THE INFLUENCE OF ATMOSPHERE AND SURFACE TOPOGRAPHY OF PVD HARD COATINS ON THEIR TRIBOLOGICAL PROPERTIES

Aljaž Drnovšek

Doctoral Dissertation
Jožef Stefan International Postgraduate School
Ljubljana, Slovenia

Supervisor: Asst. Prof. Dr. Miha Čekada, Jožef Stefan Institute, Slovenia

Evaluation Board:
Prof. Dr. Maja Remškar, Chair, Jožef Stefan Institute, Jamova 39, Ljubljana, Slovenia
Prof. Dr. Bojan Podgornik, Member, Institute of Metals and Technology, Lepi pot 11, Ljubljana, Slovenia
Prof. Dr. Franc Zupanič, Member, Faculty of Mechanical Engineering, University of Maribor, Smetanova ulica 17, Slovenia

MEDNARODNA PODIPLOMSKA ŠOLA JOŽEFA STEFANA
JOŽEF STEFAN INTERNATIONAL POSTGRADUATE SCHOOL



Aljaž Drnovšek

THE INFLUENCE OF ATMOSPHERE AND SURFACE TOPOGRAPHY OF PVD HARD COATINGS ON THEIR TRIBOLOGICAL PROPERTIES

Doctoral Dissertation

VPLIV ATMOSFERE IN TOPOGRAFIJE POVRŠINE TRDIH PVD-PREVLEK NA NJIHOVE TRIBOLOŠKE LASTNOSTI

Doktorska disertacija

Supervisor: Asst. Prof. Dr. Miha Čekada

Ljubljana, Slovenia, January 2017

To my girlfriend Lucija and to my Family

Acknowledgments

First of all, I would like to acknowledge my supervisor Asst. Prof. Miha Čekada for giving me the opportunity to work in the field of hard coatings. I am grateful for his support, guidance and encouragement, which made my scientific journey joyful.

Special thanks go to Dr. Peter Panjan for introducing me to hard coatings and tribology. Peter, thank you for our serious discussions and jokes that kept my motivation level constantly high.

To my office roommate, Matjaž, “tnx” for all your suggestions regarding work and all the “happy hours” spent on conferences.

I would also like to thank all of my coworkers from the Department of Thin Films and Surfaces: Jožko, Darja, Nastja, Srečko, Damjan, Andrej and Tomaž for making my job much easier.

All the thanks to my family, sister Petra, mother Danica and father Rado who supported me all these years.

Special thanks go to my friends for their honest laughs and for helping me maintain a healthy and social life outside the lab.

Last, but certainly not least, I would like to thank my girlfriend Lucija for her love, support and encouragement.

Abstract

Hard coatings have been in widespread use for over 40 years in the industry and the demand for new coatings is still increasing. Hence, the tribological evaluation of the coating in laboratory before the use in real application is very important. The first step to determine the adequacy of the coating for a certain application is by a simple pin-on-disc tribological test. Such a test allows us to control the parameters in a simple sliding geometry that enables the studies of friction and surface interactions such as tribochemical reactions, generation of wear debris, and galling of the counterbody material on the hard coating. These surface interactions influence the coating wear behavior.

During the tribological test the coefficient of friction undergoes several phases. The first one is the running-in period in the beginning of sliding. The topography of surfaces in contact has a major influence on this period, since the contact between the surfaces is not conformal. The topography of the sputtered coatings is mostly determined by growth defects which are common in all PVD hard coatings. Growth defects are coating irregularities like nodular defects, craters and pinholes.

In this thesis the influence of nodular defects on tribological performance of magnetron sputtered coatings is presented. The aim was to examine in detail the tribological processes that occur between the surfaces, one coated with a hard coating, and typical tribological counter-body materials. A cycle-to-cycle approach, presented in the thesis, allows us to examine the contact even when realistic counterbody material is used. TiAlN hard coating surface was examined by scanning electron microscope on regions of selected nodular defects after each cycle of sliding against alumina and softer steel (100Cr6) counterbody. In the first few cycles breaking and powdering of nodular defects was observed. This generates a large amount of hard abrasive particles. The running-in process when using alumina counterbody is relatively slow and reflects in a longer running-in period in comparison to the softer 100Cr6 counterbody. The initial interactions of nodular defects with steel counterbody have not yet been reported. The revealed mechanisms consist of micro-cutting the softer counterbody and eventually the generation and formation of tribological film patches on the sites of nodular defects. Distinct differences in wear mechanisms between the two counterbody materials in contact are presented.

As the nodular defects wear out, the running-in period ends and the transition to the second period, the steady state period, begins.

The tribochemical reaction between the surfaces is the prevailing process which determines the friction and wear behavior in the steady state period. To test this, pin-on-disc experiments with several conventional hard coatings, such as TiN, TiAlN and CrN and more advanced hard coatings, namely CrAlN and CrVN, were performed in different atmospheres with alumina counterbody. Test results performed in ambient air atmosphere, as a reference, and in inert (N_2) and oxidizing (O_2) atmosphere are reported. A detailed SEM/FIB and EDS analysis of wear tracks and wear debris is presented in the thesis. Results show that the coefficient of friction and wear behavior of the coatings sliding against alumina is severely influenced by the change of atmosphere. Tests showed different behavior such as low friction and low relative wear due to the lack of tribological oxidation in nitrogen atmosphere and changes in friction coefficient due to different surface chemistry invoked in pure oxygen atmosphere. Fish-scale-like features on novel advanced hard coatings were found in oxidizing atmosphere.

At the end, a comparison in tribological behavior is presented based on the experiments on the conventional and advanced coatings.

Povzetek

Trde zaščitne prevleke so že več kot 40 let razširjene v industriji in še vedno povpraševanje po novih prevlekah narašča. Ravno zato je tako pomembna laboratorijska karakterizacija prevlek, še preden se jih uporabi v industriji. V prvem koraku lahko tribološko ustreznost prevleke za določeno industrijsko aplikacijo preverimo z enostavnim testiranjem v konfiguraciji pin-on-disc. Takšni testi omogočajo natančen nadzor parametrov drsenja pri preprosti drsni geometriji, kar omogoča študije trenja in površinskih interakcij, kot so nastanek tribokemijskih plasti, generiranje obrabnih delcev ter sprijemanje materiala protitelesa. Površinske interakcije močno vplivajo na obrabno obstojnost prevlek.

V različnih fazah tribološkega testa se koeficient trenja spreminja. V prvi fazi, to je na začeteku drsenja, je utekanje. Na to najbolj vpliva topografija teles v stiku, saj stik med površinama ni konformen. Napake rasti prevlek in njihova gostota neposredno vplivajo na topografijo nanesene prevleke. Značilne so za vse trde PVD-prevleke. Napake rasti lahko razdelimo na napake, ki izvirajo iz globine prevleke (nodularne defekte), na površinske kraterje in luknjice kot posledica poroznosti prevleke.

V doktorskem delu sem predstavil vpliv nodularnih defektov na tribološke lastnosti magnetronsko napršenih prevlek. Cilj doktorskega dela je bil preučiti in opredeliti procese, ki se zgodijo med površinama, ki sestavljata tribološki kontakt. Z uporabo pristopa preučevanja vsakega cikla posebej nam omogoča, da lahko opazujemo stik med realnim protitelesom in prevleko. Na trdi prevleki TiAlN sem z vrstičnim elektronskim mikroskopom preučeval vnaprej izbrana območja z nodularnimi defekti po vsakem ciklu drsenja z aluminij oksidno in jekleno (100Cr6) kroglico.

V disertaciji poročam o razpadu nodularnega defekta na več delcev. Ta se razdrobi v majhne delce že v prvih ciklih drsenja, kar ustvari velike količine trdih abrazivnih delcev. Ta proces je relativno počasen, kar dokazuje tudi daljše utekanje v primerjavi z mehkejšim jeklom 100Cr6 kot protitelesom. Raziskav teh začetnih interakcij nodularnega defekta z jeklom še nismo zasledili v literaturi. Prvi opažen mehanizem je rezanje mehkejšega protitelesa z nodularnimi defekti na mikrometrski skali, kasneje pa tudi sočasno nastajanje in rast triboloških plasti na mestih z nodularnimi defekti. V disertaciji sem predstavil očitne razlike med mehanizmi obrabe v stiku z aluminij oksidno in jekleno kroglico.

Utekanje se zaključi, ko se nodularni defekti izrabijo. Za utekanjem pa nastopi faza dinamičnega ravnovesja koeficienta trenja. V disertaciji sem predpostavil, da igrajo tribokemijske reakcije med površinama odločilno vlogo za obnašanje trenja in obrabe, še posebej v dinamičnegem ravnovesju trenja. Da bi to tudi pokazali, smo izvedli poizkuse pin-on-disk z več vrstami običajnih trdih prevlek, kot so TiN, TiAlN in CrN, in naprednejšimi trdimi prevlekami CrAlN in CrVN. Poročamo o rezultatih opravljenih testov v zraku, kot referenci, ter v inertni (N_2) in oksidacijski (O_2) atmosferi. V delu je predstavljena podrobna analiza SEM / FIB in analiza EDS obrabnih kalot in obrabnih delcev. Rezultati kažejo, da sta koeficient trenja in obrabe prevlek močno odvisna od atmosfere, v kateri poteka drsenje. Poročamo o nizkem trenju in obrabi zaradi pomanjkanja tribološke oksidacije v atmosferi dušika ter drugačnem koeficientu trenja zaradi druge površinske kemije v atmosferi čistega kisika. Opazil sem tudi nastanek »luskam podobnih« obrabnih delcev, ki nastajajo le v kisikovi atmosferi na naprednih trdih prevlekah.

Na koncu je na osnovi meritev predstavljena tudi tribološka primerjava med konvencionalnimi in naprednimi prevlekami.

Contents

List of Figures xv

List of Tables xvii

Abbreviations xix

1 Introduction 1
1.1 Aims of the Thesis 2

2 Theoretical Part 5
2.1 Hard Coatings 5
2.2 Tribology of Hard Coatings 10
2.2.1 Wear 11
2.2.2 Friction 14
2.3 Parameters Influencing Tribological Performance of Hard Coatings 17
2.3.1 Topography of Coated Surfaces 17
2.3.1.1 Growth defects in magnetron sputtered hard coatings 18
2.3.1.2 Classification of growth defects 20
2.3.1.3 Growth defect sources in magnetron sputtering systems 22
2.3.1.4 Influence of surface topography on tribological behavior 22
2.3.1.5 Role of growth defects in coatings 24
2.3.2 The influence of environment on friction and wear 26

3 Experimental Methods 29
3.1 Hard Coating Preparation 29
3.1.1 Substrates 29
3.1.2 Deposition of hard coatings in industrial magnetron deposition system 29
3.1.3 Magnetron targets 30
3.2 Crystal Structure and Microstructure Characterization 31
3.2.1 X-ray diffraction 31
3.2.2 Scanning electron microscope and focused ion beam microscope 32
3.3 Topography Characterization 34
3.3.1 Stylus profilometry 34
3.4 Mechanical Characterization 35
3.4.1 Adhesion measurements 35
3.4.2 Hardness measurements 35
3.4.3 Friction and wear characterization 36

4 The Influence of Growth Defects on Tribological Properties of Hard Coatings 39
4.1 Coating characteristics 39
4.2 Results 40
4.2.1 Reciprocal tests using Al_2O_3 counterbody 40
4.2.2 Reciprocal test using 100Cr6 counterbody 42
4.2.3 Unidirectional tests with the Al_2O_3 ball counterbody 46
4.2.4 Unidirectional tests with the 100Cr6 ball counterbody 51

5 The Influence of Surrounding Atmosphere on Tribological Properties of Hard Coatings 57
5.1 Coating characterization 57
5.2 Results 59
5.2.1 Friction and wear in ambient air atmosphere 59

5.2.2 Friction and wear in nitrogen atmosphere 59
5.2.3 Friction and wear in oxygen atmosphere 60
5.2.4 TiN wear track analysis 61
5.2.5 TiAlN wear track analysis 63
5.2.6 CrN wear track analysis 65
5.2.7 CrAlN and CrVN wear track analysis 68

6 Discussion **73**

7 Conclusions **77**

References **81**

Bibliography **87**

Biography **89**

List of Figures

Figure 2.1: Different hard coatings designs 7
Figure 2.2: Hardness of TiN coatings with different composition 8
Figure 2.3: Unit cell of TiN alloyed with aluminum 9
Figure 2.4: Hardness of CrAlN coatings as a function of aluminum content 9
Figure 2.5: The tribological process in a contact between two surfaces 10
Figure 2.6: Tribologically important properties of different zones of a coated system 11
Figure 2.7: Wear interrelations based on contact type 12
Figure 2.8: Four basic wear mechanisms 12
Figure 2.9: Abrasive wear modes 13
Figure 2.10: Three components of the sliding friction 14
Figure 2.11: Development of friction coefficient with sliding distance 15
Figure 2.12: Effect of removing wear particles 16
Figure 2.13: Types of friction force curves in dependence of the number of cycles 17
Figure 2.14: Different growth defects and surface irregularities 18
Figure 2.15: Different sources of growth defects. 19
Figure 2.16: Nodular defect density as a function of deposition time 19
Figure 2.17: Peak density distributions 20
Figure 2.18: Different growth defects according to classification 21
Figure 2.19: Self-propulsion model 21
Figure 2.20: Common growth defect sources within the vacuum chamber. 22
Figure 2.21: Pressure distribution between rough surfaces 23
Figure 2.22: Changes of R_a, R_q and R_{max} parameters during sliding 23
Figure 2.23: Surface roughness 25
Figure 2.24: SEM images of GD. 26
Figure 3.1: Scheme of the CemeCon deposition system vacuum chamber. 30
Figure 3.2: (a) Triangular target and (b) scheme of deposition system 31
Figure 3.3: Image of XRD apparatus 32
Figure 3.4: SEM images of nodular defects collected with different electrons. 33
Figure 3.5: SEM image of coating cross section 33
Figure 3.6: Scheme of the profilometer working principle. 34
Figure 3.7: Stylus profile images of wear track: 34
Figure 3.8: Crack generation and coating failure during scratch test 35
Figure 3.9: The Fischerscope H100C hardness tester. 35
Figure 3.10: Scheme of a standard room temperature tribometer. 36
Figure 3.11: Sample preparation for ND identification under SEM. 38
Figure 4.1: Stylus profilometer images of wear tracks on TiAlN 40
Figure 4.2: Friction coefficient measurements in the reciprocal mode. 41
Figure 4.3: SEM images of groups of nodular defects on TiAlN before and after the test. . 41
Figure 4.4: SEM images of nodular defects before and after pin-on-disc. 42
Figure 4.5: Stylus profilometer images 43
Figure 4.6: COF measurements with 100Cr6 as counterbody. 44
Figure 4.7: SEM images of different groups of ND before and after test. 44
Figure 4.8: SEM images of nodular defects. 45
Figure 4.9: The coating surface 46
Figure 4.10: SEM images of the same group of growth defects 47
Figure 4.11: Optical micrographs of wear scar formed on the alumina balls. 48
Figure 4.12: Optical micrograph and SEM image of counterbody and wear track 49
Figure 4.13: SEM images of nodular defect in the center of the wear track. 49
Figure 4.14: FIB and EDS analysis of nodular defects after 64 and 128 cycles sliding 50
Figure 4.15: The coating surface (a) before and (b) after 128 cycles using the 100Cr6 ball. 51

Figure 4.16:SEM images of the same group of growth defects 52
Figure 4.17:SEM images of ND removal. 53
Figure 4.18:Optical micrograph images of wear scar formed on the 100Cr6 ball. 53
Figure 4.19:SEM images of nodular defect and counterbody surface 55
Figure 4.20:SEM image of a set of defects 56
Figure 5.1: Average composition obtained by EDS 58
Figure 5.2: The XRD patterns of hard coatings used in tribological experiments. 58
Figure 5.3: Ambient air measurements 59
Figure 5.4: Nitrogen atmosphere measurements. 60
Figure 5.5: Oxygen atmosphere measurements. 61
Figure 5.6: SEM analysis of a wear track made in ambient air test. 61
Figure 5.7: SEM analysis of a wear track made in nitrogen atmosphere test. 62
Figure 5.8: SEM analysis of a wear track made in the oxygen atmosphere test 63
Figure 5.9: SEM analysis of a wear track made in the ambient air test. 64
Figure 5.10:SEM analysis of a wear track made in the nitrogen atmosphere test. 64
Figure 5.11:SEM analysis of a wear track made in the oxygen atmosphere test 65
Figure 5.12:SEM analysis of a wear track made in the ambient air test. 66
Figure 5.13:SEM analysis of a wear track made in the nitrogen atmosphere test. 66
Figure 5.14:SEM analysis of a wear track made in the oxygen atmosphere test 67
Figure 5.15:FIB analysis of CrN wear track after the oxygen atmosphere test 68
Figure 5.16:SEM analysis of a wear track made in the ambient air test. 69
Figure 5.17:SEM analysis of a wear track made in the nitrogen atmosphere test 69
Figure 5.18:SEM analysis of a wear track made in the oxygen atmosphere test 70
Figure 5.19:EDS mapping of fish-scale-like structures in CrVN wear track. 71
Figure 5.20:FIB analysis of nodular defect after oxygen atmosphere test 71
Figure 5.21:SEM images of CrVN and CrAlN wear tracks in an oxygen environment 72

List of Tables

Table 5.1: Measured hard coating physical properties..... 57

Abbreviations

PVD . . . Physical vapor deposition
ND . . . Nodular defect
COF . . . Coefficient of friction
μ . . . Coefficient of friction
CVD . . . Chemical vapor deposition
TiN . . . Titanium nitride
TiAlN . . . Titanium aluminum nitride
CrN . . . Chromium nitride
CrAlN . . . Chromium aluminum nitride
CrVN . . . Chromium vanadium nitride
SEM . . . Scanning electron microscope
FIB . . . Focused ion beam microscope
OM . . . Optical microscope
SE . . . Secondary electrons
BSE . . . Backscattered electrons

Chapter 1

Introduction

Today's industry's aim is to produce high quality products at high production rate which enables a low price of an end product. For a competitive production rate and high quality of the products manufacturing work must be carried out continuously and uninterrupted as long as possible. Therefore the tools used in the product manufactory line must withstand a high amount of working hours without tool surface structural and topographical changes that would reflect in products as lower quality. A clever design of the tools, from the raw material selection to a finished tool surface treatment, must be done in order to resist the tools surface changes that would lead to the tools failure. Deposition of hard coatings with a few microns in thickness, as one of possible surface engineering techniques, has proven to be essential for the protection of tools that operate in the harshest environments. Starting with thermally activated chemical vapor deposition (CVD), first applied in 1969, different methods have been developed including plasma-assisted vapor deposition (PACVD) and physical vapor deposition (PVD). Hence industrial use of hard coatings has already been used for over 40 years and, not surprisingly, the demand for new coatings is still increasing especially with the introduction of new industrial technologies and workpiece materials. The hard coatings are commonly used on cutting and forming tools, on bearings, implants, and hard discs. Automotive, food and pharmaceutical industry are also common users of hard protective coatings.

Compared with uncoated tools, the use of hard protective coatings increases the productivity and enables some of the advanced machining operations, such as high speed cutting, hard machining and dry machining. The use of such coatings provides an inert contact between the tool and the work piece, moreover the use of different lubricants can be eliminated. This is especially of high importance in the pharmaceutical and food industry due to strict safety mandates.

The pursuit for better production rates at lower costs also promotes the use of novel industrial technologies. These present new challenges for hard coatings developers. The development of new hard coatings requires a detailed characterization of chemical, physical and mechanical adequacy before the use on a small scale (lab) and eventually in a real production line. To evaluate the hard coating mechanical performance, well-controlled tribological tests are first performed in laboratories.

The tribometer in the pin-on-disc or a similar configuration is considered to be the first step into characterization of the tribological behavior of the materials. Relatively simple contact geometry, controlled environment and basic simulation of the tool operation enables detailed studies of the material behavior under load which can then be translated to a more realistic model.

Although tribology is a study of interacting surfaces in relative motion it has to be viewed as a complex system of many different parameters that influence the tribophysical and tribochemical responses. As the name implies the hard coating main characteristic is its relatively high hardness, but there are several other important properties that trigger a tribological response. At first an appropriate substrate with suitable thermal expansion coefficient, elasticity, hardness and fracture toughness must be chosen. Second, the hard coating must possess appropriate hardness, elasticity, oxidation and corrosion resistance, and thermal stability to fit the application of the tool. The coating must also adhere well to the substrate since it has to withstand large tangential forces during the tool operation. And third, the (hard coating) surface defines the contact in the tribological system. Therefore the surface roughness, chemical reactivity and shear strength dictate the initial response on the load during the tool operation.

There are numerous reports on how the surface roughness influences the tribological behavior [1-9]. The majority of studies deal with parameters such as average surface roughness (R_a) which is more a result of substrate surface preparation and not an individual coating topographical feature. A closer look at PVD sputtered coating surface reveals that the surface is covered by growth defects in the form of nodular defects (asperities), pinholes and craters. These defects are the result of an individual deposition process and present a drawback of hard coatings.

Possible sources of growth defects and their influence on the coating corrosion and oxidation performance are described in the forthcoming chapters of this thesis. How growth defects influence the tribological properties of the PVD magnetron sputtered coating is not well known. In-situ tribometry studies (where one can observe the contact through a transparent counterbody) are not considered industrially adequate. The examination of the contact region when more realistic materials are used is extremely difficult. Furthermore, the role of growth defects is expected to be different depending on the counterbody material choice.

Hence the focus of this thesis is on understanding of behavior of nodular defects in tribological contact when steel and harder alumina is used for the counterbody. The role of growth defects is especially important in the beginning of the tribological test or tool operation in the so-called running-in period where the contact between the sliding bodies is not fully developed and defined. After the asperities wear off, and the contact zone stabilizes, the formation of a tribological film in the form of small particles from asperities and oxidized wear products can begin. At this stage, called the steady-state period, the wear and friction behavior is severely influenced by chemical reactions between the environment and the moving surfaces. The environment, such as relative humidity level, can influence the collection and removal of the wear debris from the wear track. The surrounding atmosphere also influences the tribological film formation, wear regime and surface oxidation rate of the coated surface. From a basic surface science point of view it is important to study the behavior in a well-controlled environment. The absence of water at the interface invokes different chemical reactions than that in high humid environment. The lack of oxygen reduces the oxidation rate which, with the same analogy as with relative humidity, produces different wear products which influence the tribological behavior.

The emergences of new technologies which are faster, more economical and greener invoke new challenges in the development of tool coatings. Self-lubricant coatings, such as VN-based coatings, are the examples of the latest R&D products. Such coatings enable the abandonment or reduction of cooling or low-friction additives, which present an environmental risk. There are not many reports on how the environment (oxygen, nitrogen and humidity level) influences the friction and wear behavior of conventional PVD hard coatings. The comparison to the more advanced coatings such as self-lubricant CrN/CrVN and advanced high temperature coating CrN/CrAlN against conventional PVD coatings will reduce the gap in basic tribophysic and tribochemistry knowledge of advanced coatings.

1.1 Aims of the Thesis

The aim of the thesis is to contribute to understanding of the basic tribological processes of the hard protective PVD coatings and detailed analysis of the worn surface. In the first part we addressed some basic questions regarding the role of growth defects in a tribological contact. Nodular defects form the first contact points between the sliding surfaces, hence their importance is superior in the beginning of the sliding (the running-in period). Their role in sliding against alumina and 100Cr6 steel is presented.

After the nodular defects wear off the contact area is better defined. After this the COF (coefficient of friction) behavior enters the steady state. At this stage the COF is influenced by invoked tribological chemistry and entrapped particles between the sliding surfaces. The change in atmosphere enables to suppress or enhance the chemical reactions at the surface. The response to atmospheric changes is visible in COF and different wear mechanisms. The comparison between conventional and advanced hard protective PVD coatings sliding in different atmospheres will be addressed in the second part of this thesis.

Generally, the aim of the thesis is to answer the following questions:

1. What influences the running-in period?
2. What is the most important origin of the wear particles between the sliding surfaces?
3. How do nodular defects act when sliding against 100Cr6 or Al_2O_3 counterbody?
4. Is there any difference between sliding modes in the running-in period (unidirectional and reciprocal)?
5. How do different hard coatings behave in terms of friction and wear in ambient atmosphere?
6. How do hard coatings behave in terms of friction and wear in inert or in oxidative atmosphere? What is the role of tribo oxidation?
7. Are there any differences in tribological behavior between conventional and advanced coatings?

Chapter 2

Theoretical Part

2.1 Hard Coatings

During the work process the tools are subjected to extreme tribological conditions such as high thermal and mechanical loads. To match the quality production standard the **basic tool material** must resist wear, oxidation, corrosion and galling i.e. sticking of the workpiece material to the surface of the tool. Steels offer high hardness, toughness and relatively simple production at low production costs. This makes the steel one of the most widely used materials for industrial production. Though there is still ongoing research in bulk steel improvement, the focus has shifted on the **steel surface enhancement** since all the tribological contacts are surface related [10].

A wide variety of techniques has been developed that are used to improve the wear resistance of the tool surface without affecting bulk of the material [10]. Methods that involve an additional layer with superior mechanical and tribological properties present only a part of surface engineering techniques.

A common and effective approach to improve the tool surface is by deposition of a protective tribological coating such as hard coatings. It enables improved wear and oxidation resistance which can lead to higher cutting speeds, and reduced friction in case of low friction coatings. Tribological coatings can also reduce the tendency to sticking (material pick up) and can contribute to reduced weight of the tools [11].

Materials that can be used for hard coatings are carbides, nitrides and lately oxides. Between them the transition metal nitrides have the longest history of use in surface protective applications. Mixed bond structure varying from covalent, metallic and ionic in transition metal nitrides is responsible for high hardness, superior wear resistance, chemical inertness and oxidation resistance which makes them an effective material for hard metal and tool steel surface enhancement [12].

For a successful application in the industrial use of the hard coating, positive tribological effects of the coated system must also overcome some of its limitations. The limitations of coated surfaces are the substrate ability to withstand high coating deposition temperature, and high level of hardness and stiffness of a steel substrate or the coating itself. Especially, for coatings performance (load carrying capacity) at high working temperatures. Other limitations of tribological coatings are addressed to the deposition processes ability to coat complicated tool's geometry and related problems with coating to substrate adhesion [11]. Thus the basic (**primary**) **requirements** for individual coatings are: good adhesion, high wear resistance at working temperatures and chemical stability (inertness) towards the workpiece material [13]. Achieving these and **secondary requirements** like relevant physical properties, appropriate crystalline microstructure, smooth morphology and controlled coating compressive residual stresses within the coating is not a trivial task. To match the coating requirements to specific industrial application the design of a coating is tailored to avoid the premature coating failure as much as possible.

Deposition of hard coatings

Deposition of hard coatings on tools is generally done by two different processes, either **chemical vapor deposition** (CVD) or **physical vapor deposition** (PVD). A CVD process usually involves volatile precursors and thus has a negative impact on the environment.

Additionally, the process itself takes place at high temperatures (around 1000 °C), which narrows the substrate material selection (limited to hard metals). The CVD deposition of TiN, for example

$$2TiCl_4 + N_2 + 4H_2 \rightarrow 2TiN + 8HCl$$

takes place at temperatures between 850–1100 °C [14].
In PVD processes, the coating is deposited in vacuum by condensation from a flux of neutral or ionized atoms of metals. The temperatures in PVD process are usually much lower [14]. The two main types of PVD are **evaporation** and **sputtering**. Thermal evaporation is the oldest technique used for depositing thin films. The first step is the generation of vapor by heating the source material. This vapor is then transported in vacuum from the source to the substrate, where metal vapor is condensed to a solid that forms a coating. The most basic way to heat the source material in the vacuum chamber is resistive heating, heating by the electrons or by a laser beam. The PVD evaporation methods are:

a) Resistive vacuum evaporation
b) Electron-beam evaporation
c) Molecular beam epitaxy
d) Pulsed laser deposition (PLD)
e) Cathodic arc

Deposition by sputtering offers easier control over thickness and process parameters. In this process the surface atoms of the target material are ejected by ion bombardment. Ions are created in the plasma discharge, then extracted and accelerated by electric field. If the energy of an incident ion is too low (few eV), it may just bounce from the target. If the energy is too high (>10 keV) the ion penetrates deep into the target causing ion implantation. Only if the ion energy is somewhere in between these two cases the ion collision with the target atom causes the removal of target atoms from the surface. Hence, the sputtering process is characterized by the sputtering yield, which is defined as the number of ejected atoms per incident ion [15]. It generally depends on the energy of the incident ions, the masses of the ions and target atoms, the binding energy of atoms in the solid and the incident angle of ions. In the PVD process we create plasma by applying a high voltage across a low-pressure gas. The argon ions created in this plasma field hit the target material, transferring the energy to sputtered target atoms. Common PVD sputtering techniques are:

a) Diode sputtering (now rarely in use)
b) Magnetron sputtering
c) Ion plating

The properties of hard coatings can be tailored by the **base material** selection, **alloying** with additional materials or by a **structural design** of the coating. Different transition metals have been tested to produce single layer nitride coatings. Within the same material different deposition process parameters were varied to modify the microstructural features of the coatings. For example, in the magnetron sputtering, the deposition parameters such as substrate temperature, pressure of working gas, rotation, target power, substrate bias, energy and flux of bombarding particles utilized for growing the films are known to influence grain growth and crystallographic texture. All of them affect the resulting microstructure and properties of the coating [16, 17]. By development of new deposition techniques with multiple sources the coatings that had first been used as a single material type have been combined with other coating materials. This gives rise to different coating designs. The most common coating designs are depicted in Figure 2.1.

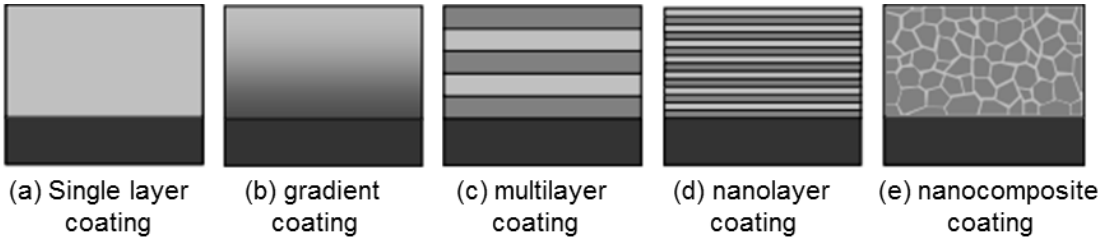


Figure 2.1: Different hard coatings designs: (a) single layer, (b) gradient, (c) multilayered, (d) nanolayered and (e) nanocomposite [18].

Single layer coatings have the simplest structure (Figure 2.1(a)). TiN and CrN hard coatings are the most known representatives of such design. Their thickness usually varies between 3 and 5 μm. If the composition changes gradually within the coating, then the term **gradient coating** is used (Figure 2.1 (b)). The **multilayer coatings** are similar, but the transition from one material to another is in this case sharp and it usually involves several sequences of individual coating layers. Their thickness can be between 0.1 and 1 μm per layer. New more advanced coatings like **nanolayered** and **nanocomposite coatings** belong to the special class of nanostructured coatings. These coatings excel in higher hardness and better mechanical properties than other types, i.e. conventional coatings.
Nevertheless, the materials such as titanium and chromium are the most widely used base materials, producing TiN and CrN single layer coatings. With an increasing need for improvement of chemical and physical properties these coatings were alloyed with different materials, most successfully with aluminum, silicon and vanadium.

For the purpose of better understanding, some conventional (TiN, TiAlN and CrN) and advanced (CrAlN and CrVN) hard coatings, used in this thesis, (properties) will be shortly presented.

Titanium nitride – TiN

PVD TiN has been used for coating tool steels since the mid-sixties [14]. It was the first commercially successful hard coating. Its attributes are relatively high hardness (2200 HV), chemical stability, low friction and wear. Due to its golden color it also became practical for decoration purposes [19, 20].

Titanium nitride crystallizes in the cubic (NaCl) structure and exists as a solid solution containing nitrogen in the range 37.5 to 50 at.% The hardness of single phase TiN can differ depending on the composition and the PVD process. This is shown in Figure 2.2 where Sundgren [20] collected measurements from literature. In coatings which contain Ti_2N phase the hardness increases with nitrogen concentration.

The crucial disadvantage of TiN coating is the relatively low oxidation resistance which makes the coating useless in high speed cutting applications [14, 20]. This increased the research to improve the oxidation resistance with alloying the TiN coatings with other transition metals, most successfully with aluminum producing TiAlN hard coating.

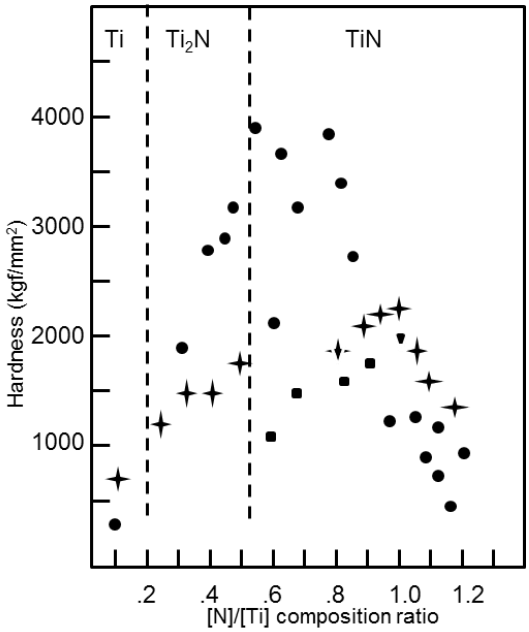


Figure 2.2: Hardness of TiN coatings with different composition [20].

Chromium nitride – CrN

CrN hard coatings became successful in tool protection due to anti-oxidative and anti-corrosion properties [21]. It was proven to be also one of the most uncomplicated systems among the common types of coatings, e.g. TiCN, TiN, TiAlN and CrN, thus making it frequently used in the industry [22]. An advantage over TiN coating is its higher chemical inertness. Because of the latter and higher toughness, the CrN coating is superior in respect to TiN [23]. In addition, the CrN coatings can be successfully deposited at much lower temperatures (below 250°C). This is especially important for the protection of materials that cannot withstand higher temperatures [24].

CrN hard coating is generally characterized by a fine grained and low stress structure which also enables the deposition of thicker coatings [22]. The coating belongs to the single metal nitride coating similar to TiN, therefore it is a suitable candidate for alloying with other elements to tune the coating properties to the specific application. The hardness of CrN coating is expected to be around 2200 HV.

Titanium aluminum nitride - TiAlN

By addition of aluminum in the TiN, the wear and oxidation resistance are enhanced [25]. Aluminum was chosen as an alloying element because it forms a stable aluminum oxide layer when it is exposed to high temperatures. This layer acts as a protective layer preventing any further oxidation. In alloying, the titanium atoms are partially substituted by smaller aluminum atoms (Figure 2.3). This increases the hardness of the coating to 3200HV and decreases the lattice parameter, hence TiAlN has a more dense structure [25]. Maximum microhardness measurements were obtained for 60 at. % of aluminum in TiAlN. As we increase the Al alloying above 70 at. % the microhardness decreases [12]. Excessive amount of aluminum changes the cubic (NaCl) structure of the TiAlN coating to the hexagonal (ZnS) structure which is typical for AlN. Scanning electron microscope (SEM) pictures revealed that the columnar microstructure is dominant at low aluminum content. At high aluminum content (above 60 at. %) the grain size decreases and the structure becomes less dense columnar [12, 26].

Tribological behavior of TiAlN was extensively studied [27-29]. The friction coefficient measurements in dry environment showed that compared to TiN coating the TiAlN coatings are more appropriate for high speed machining due to lower friction coefficient and low wear at higher sliding speeds and temperatures [27].

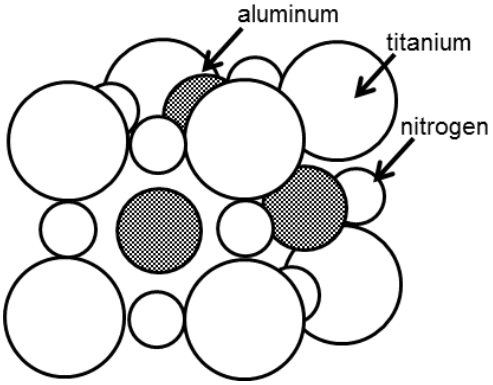


Figure 2.3: Unit cell of TiN alloyed with aluminum [25].

Chromium aluminum nitride – CrAlN

The CrAlN underwent a similar development process as TiAlN coating. Chromium nitride (CrN) has been successfully applied to the molding dies and cutting tools. But its relatively low hardness and low abrasive wear resistance left some possibilities for improvements, especially for the steel cutting applications [30]. Now its performance is expected to be improved with the addition of aluminum due to the formation of complex oxides at high temperatures [31]. Aluminum in CrN has a significant effect on hardness and thermal stability when compared to pure CrN coatings as long as the structure is cubic (NaCl) type [32]. As the aluminum content increases the transformation to hexagonal (ZnS) structure can occur. This happens when the aluminum content is beyond the solubility limit of aluminum or aluminum nitride in the hexagonal structure, between 51 and 69 at. % [33]. The hexagonal structure has a lower hardness and poor ductility but is still useful in some applications because it shows high oxidation resistivity at elevated temperatures [34].

As in other coatings the deposition process and its parameters influence the coating morphology, grain size and hardness. The review of the topic reveals that different results were obtained in the process of tuning [35]. This indicates the complexity of tuning the coating properties for an individual coating system. Hardness as a function of aluminum content is shown in Figure 2.4, summarizing data from several authors [35].

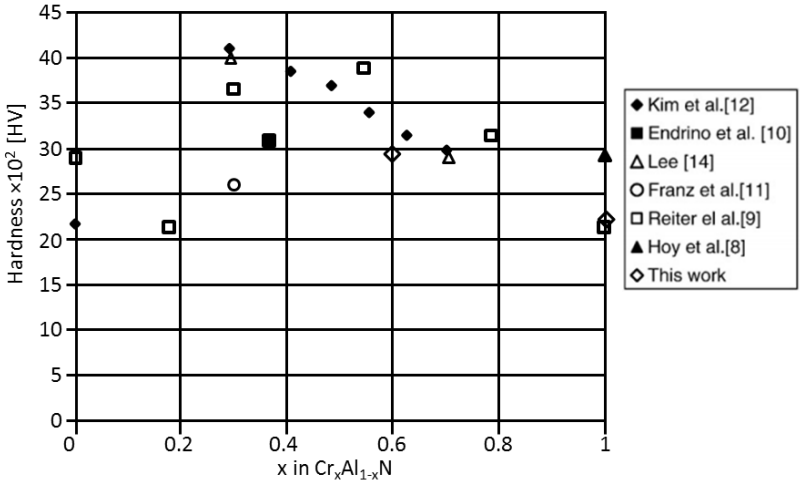


Figure 2.4: Hardness of CrAlN coatings as a function of aluminum content [35].

Chromium vanadium nitride – CrVN

Recently, much attention has been attributed to develop new solid lubrication protective coatings, since the harsh environment, such as elevated temperature with high humidity, can lead to failure of conventional solid lubricants (DLC, MoS_2 and h-BN) [36]. Low friction can be achieved by formation of lubricous oxides. Sub-stoichiometric compounds, known as Magnéli phases, are known to form oxides with low shear strength.

Elements such as molybdenum, tungsten, titanium and vanadium are known to form Magnéli phases. Vanadium forms oxides with formula:

$$V_nO_{2n-1} \quad \text{for } 4 \leq n \leq 8$$

which are known as Magnéli phase oxides [37] and also higher oxidized vanadium oxides that can be abbreviated as:

$$V_nO_{2n+1}$$

The objective of VN coatings is to reduce friction at high temperatures by self-lubrication [38]. At elevated temperatures different vanadium oxides start to form from VN. Some of these oxides have weakly bound lattice planes and a low melting temperature. These properties can lead to low friction behavior since little force is needed to shear these planes. V_2O_5 was found to be mainly responsible for the reduction of the friction. This oxide has a low melting temperature between 670 and 685°C. When the contact temperature exceeds this temperature, the V_2O_5 can also act as a liquid lubricant [38].
With the addition of vanadium to the CrN matrix, an attempt is to reduce friction but keep the mechanical integrity of the CrN coating intact. The addition of vanadium also increases the hardness due to the solid-solution hardening effect [39].Typical hardness values of vanadium doped CrN coatings are from 1800–2400 HV, depending on the amount of vanadium.

Before using the hard coating in an industrial application all the coatings undergo laboratory testing where response of the coating under mechanical load is measured in terms of friction and wear. The scientific field that covers studies of friction and wear of surfaces in relative motion is known as tribology.

2.2 Tribology of Hard Coatings

Tribology is a field of science and technology where contacting bodies in relative motion to each other are studied. Tribology couples many disciplines from physics, chemistry to mechanical engineering and material science. It is important that tribology is considered as a system of different parameters which all influence the tribophysical and tribochemical response (Figure 2.5). The tribological process can be described as a process where materials in relative motion with properties such as chemical composition, microstructure, hardness and the material topographical properties react in a certain environment with some energy input to form a contact. This invokes mechanical and tribochemical changes of materials in the contact. They are expressed as material changes in chemical and geometrical sense as well as the changes in released energy [1, 40, 41].

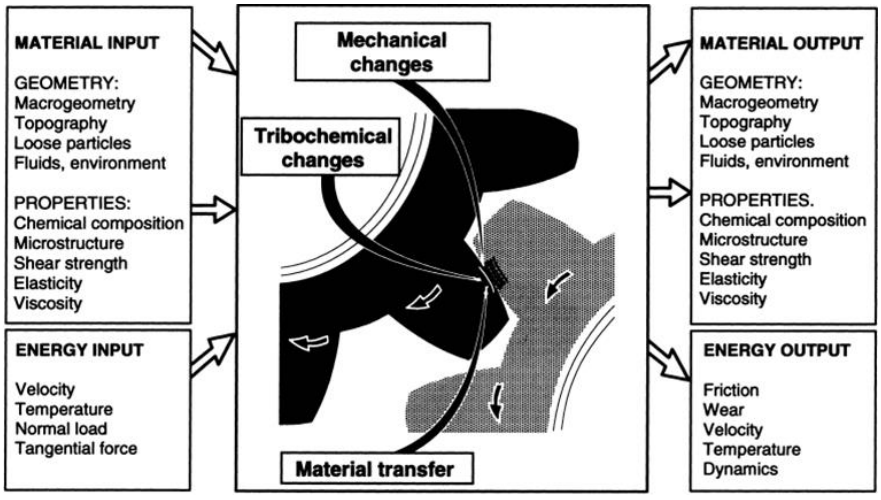


Figure 2.5: The tribological process in a contact between two surfaces [41].

Knowing the input properties of contacting surfaces and laws which mandate the tribological changes helps us to control the output energy and the output material changes, namely friction and wear. For that the tribology plays an important role in human society from the ancient times and its role is continuously amplified with growing development and technology. Nowadays the need to reduce friction and wear is dictated by economic and environmental mandates. The competitive market forces the scientists and engineers to develop materials and procedures to enhance the productivity, to extend the lifetime of machinery, to save energy and to improve the safety [40]. One way to fit these requirements is by using protective (tribological) coatings at tribological contacts, but this must be done with deep consideration and care. A coated system can be divided in four different zones namely substrate, substrate-coating interface, coating and (contacting) surface. Each zone must possess properties that fit the best to the desired application which unfortunately means that most of the requirements are not achievable simultaneously. Some of these requirements are presented in Figure 2.6. The final coating success depends on the successive interplay between these properties [40, 42].

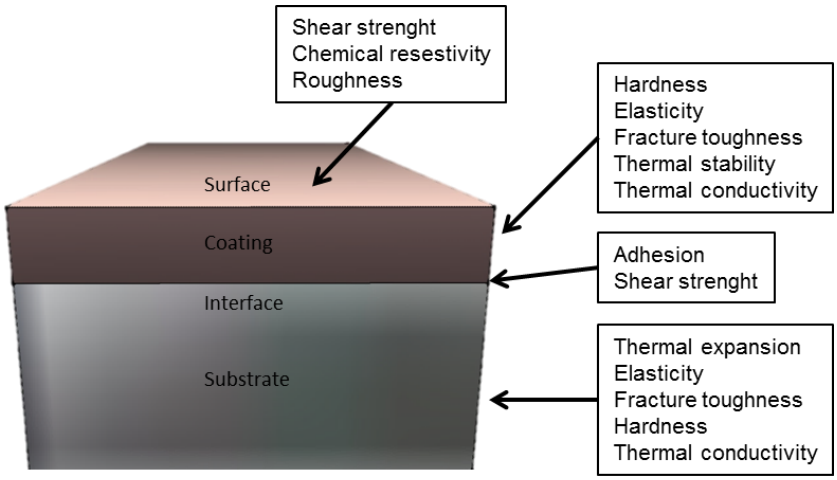


Figure 2.6: Tribologically important properties of different zones of a coated system [40, 42].

2.2.1 Wear

To explain the complexity of the processes involved in tribological contact, mechanisms such as macromechanical, micromechanical, nanomechanical and tribochemical contact, as well as the material transfer were derived [41]. In all of them wear and friction mechanisms at different scales happen simultaneously.
Surfaces in relative motion experience the removal of material at the side of the contact. This is generally addressed as *wear*. Both, friction and wear, are the response/result of the same contact system between the moving surfaces, but their relationship is still not well understood [43]. Although, generally, we observe low wear rate at low friction coefficient and vice-versa, but this is not always the case.
The material can be removed from the contact via different mechanisms (Figure 2.7) [1, 40, 44]. Different contact regimes produce wear described as sliding, rolling, impact, fretting and slurry wear type. They all cause deformations in material which lead to basic wear mechanism.

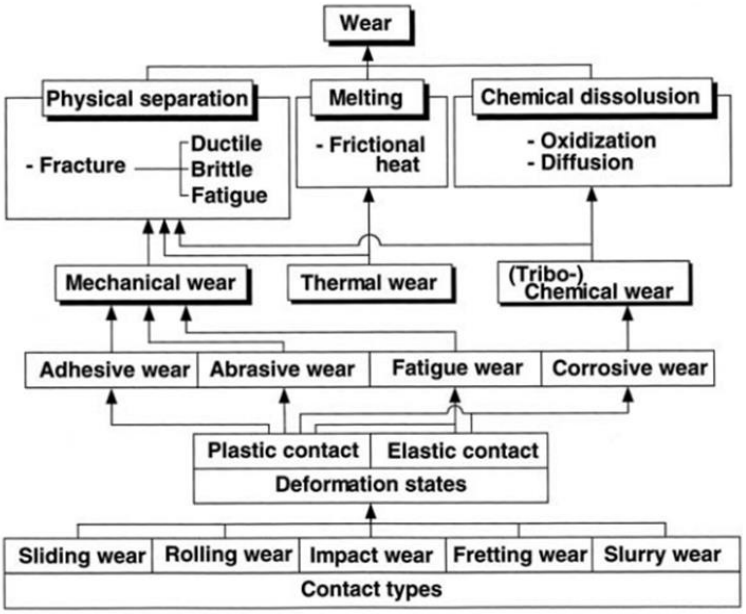


Figure 2.7: Wear interrelations based on contact type [44].

The basic wear mechanisms/modes encountered in coatings tribology are (Figure 2.8):

a) Adhesive wear
b) Abrasive wear
c) Fatigue wear
d) Chemical (corrosive) wear

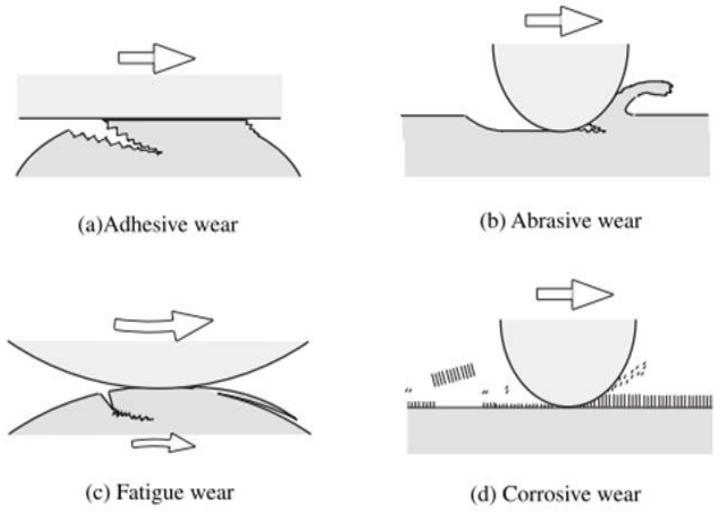


Figure 2.8: Four basic wear mechanisms [44].

Regardless the type, the wear is evaluated by the volume of the lost material or quantity of adhered material on the surface. This can be described by wear rate, specific wear rate or **wear coefficient**. Often the worn volume is directly proportional to the normal load and the sliding distance, and inversely proportional to the hardness of the material. This can be formulated as [40]

$$V = K' \frac{F_n s}{H} \tag{2.1}$$

where V is the wear volume, F_n is the normal load, s is the sliding distance, H the hardness of the material and K' is the wear coefficient. Because the volume of the removed material

is not illustrative enough in all applications the use of **wear rate** or **specific wear rate** is more commonly acknowledged [40].

$$K = \frac{V}{F_n s} \tag{2.2}$$

In this equation K is the **wear rate** and it is usually expressed with dimensions (10^{-6} mm^3/Nm) [40].

Adhesive wear

Adhesive wear occurs when asperities come into contact forming adhesive asperity junctions. When the junction is broken due to tangential forces, some material in the bulk from the softer asperity is removed (Figure 2.8 (a)). While the adhesion mechanism does not play a dominant role in the real contact, there are situations like forming tools operation, sliding in vacuum/inert atmosphere, or when flash temperatures in the contact are extremely high, where the adhesive wear could be the dominant wear mechanism [40].

Abrasive wear

Abrasive wear is common at interfaces where one of the surfaces is considerably harder than the other, when roughness of the surfaces is high or when a hard particle is entrapped between the sliding surfaces. Abrasive wear is classified by the nature of the contact and the environment. The type of the contact determines the mode of the abrasive wear. The two possible modes are known as two-body and three-body abrasive wear. A two-body wear occurs when a hard asperity removes the material from the opposite surface, while in a three-body wear the particle between the surfaces is not constrained and can move freely.

The contact environment also defines if the contact is open or closed. Open contacts are those where the surfaces are sufficiently displaced to be independent from each other. Hokkirigawa and Kato [45] divided the abrasive wear into three wear types. These are (Figure 2.9):

a) Cutting
b) Wedge forming
c) Ploughing

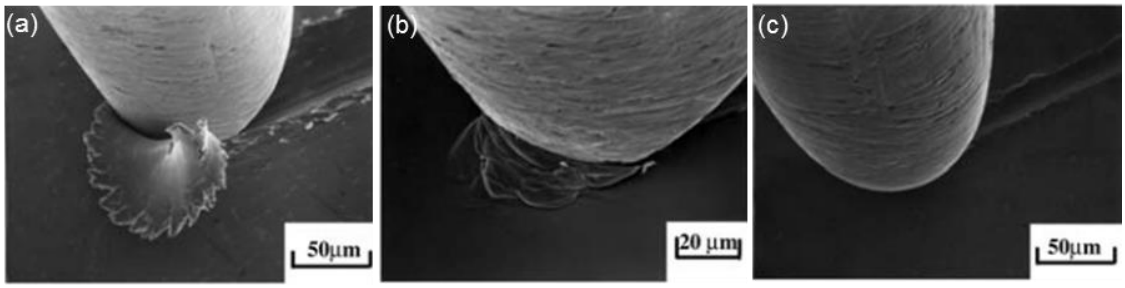


Figure 2.9: Abrasive wear modes: (a) cutting, (b) wedge forming and (c) ploughing [45].

In all three different abrasive types the formation of grooves is evident, due to wear particle generation and plastic flow of the material to form ridges on both sides of the groove.

Fatigue wear

Fatigue is a progressive and localized damage i.e. weakening of the material, which is caused by repeatedly applied loads. Wear generated in such cycling systems is called fatigue wear. Depending whether the number of cycles is low or high the fatigue mechanism can be low-cycle or high-cycle, respectively. Beside the wear associated with repeated loading and unloading a common phenomenon is the **fatigue crack growth**. This occurs when the load is higher than a certain threshold. The growth of cracks will begin from stress concentrators such as dislocations and defects. With time, the crack will reach the critical size and propagate rapidly through the material (Figure 2.8 (c)). This may result in material detachment.

Chemical wear

When the surfaces are sliding their asperities collide which causes plastic deformation of the asperities and subsequently a localized temperature rise. These localized, short term heat peak bursts are called **flash temperature** and can reach several hundred degrees above ambient temperature [46-48]. Flash temperatures influence both, the friction and the rate of the wear by inducing chemical changes i.e. **tribochemical reactions** at the sliding interface. The reaction layer continuously produced by tribochemical reactions on the surfaces is then removed by friction, therefore the relative growth rate of tribo chemical layer determines the wear rate [40].

2.2.2 Friction

Another response of a tribological system is in the form of friction. It is a force that resists the motion of sliding bodies. Friction is not an intrinsic material property but it is a system response in the form of a force. It is the energy loss mechanism of sliding [44]. The coefficient of friction, μ, is defined as the tangential force (F_t) divided by a normal load F_n on the contact(2.3).

$$\mu = \frac{F_t}{F_n} \tag{2.3}$$

Although there is still no complete physical explanation for friction, there are several general rules regarding the friction force [44]:

1. The friction force does not depend on the apparent area of contact
2. The friction force is proportional to the normal load
3. The kinetic friction force does not depend on the velocity and it is smaller than a static friction force.

Over the years of research a concept of friction has been developed, called *the genesis of friction* [49]. It postulates that the friction coefficient is affected by the sliding distance and the environment, both changing the contributions of the three major components of friction (Figure 2.10):

- **Friction due to adhesion**: Asperities that are in contact are welded together creating an adhesive junction. The continuous creating and breaking of these welded asperities cause the resistance in sliding [50]. Typical values of friction coefficient for this mechanism, μ_a*=0—0.43*, where the low value is obtained for well-lubricated surfaces and high value for identical metals sliding against each other.
- **Friction due to ploughing**: μ_p*=0—0.4*. The ploughing is an effect of a hard particle or broken asperity captured between the surfaces. The low value is obtained when no or a very small amount of particles is present in the junction. The high value is obtained in case of identical metals sliding against each other with wear particles penetrating deeply.
- **Friction due to asperity deformation**: *0—0.4*. The asperity deformation is the source of the static coefficient of friction. When the original asperities are deformed, asperity interlocking cannot take place. This component contributes to steady-state friction when new asperities are continuously generated in the sliding junction.

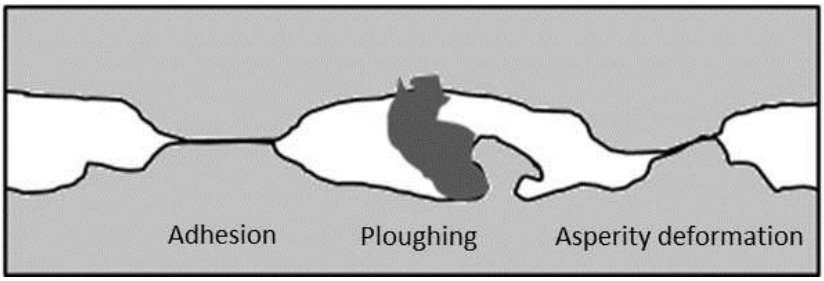


Figure 2.10: Three components of the sliding friction [40].

The friction coefficient changes with the sliding distance i.e. time. Generally, every contact starts with the running-in period, followed by the steady-state period and ends with the breakdown or destruction period. In *genesis of friction* Suh and Sin [49] identified five different friction regimes in the running-in period (Figure 2.11):

I. **Ploughing** of the surface by asperities. Due to surface contamination the adhesion is negligible. The friction in this stage is largely independent of material combinations, surface and environmental conditions.

II. The slow increase of the coefficient of friction is a result of contamination removal and adhesion to uncovered surface.

III. The increase of the coefficient of friction is due to high wear of asperities and consequently a rapid increase of wear particles between the sliding surfaces. The deformation of asperities continues as well as the contribution of adhesion due to larger clean interfacial surfaces. In this stage, the wear particles can be entrapped between the surfaces causing local ploughing.

IV. A **steady-state friction** for identical materials sliding against each other. The number of particles between the surfaces is constant. The adhesion contribution is constant too. With delamination, wear creates new asperities which contribute to asperities deformation.

V. In the case when hard stationary slider is rubbed against soft specimen. The asperities on the harder slider are removed and the surface is mirror polished. The friction coefficient decreases due to decrease in asperity deformation, ploughing and decrease of contact pressure. With mirror-like surface the number of anchorage sides for wear debris is reduced.

VI. The steady-state period of coefficient of friction is reached. Both surfaces are mirror-like polished.

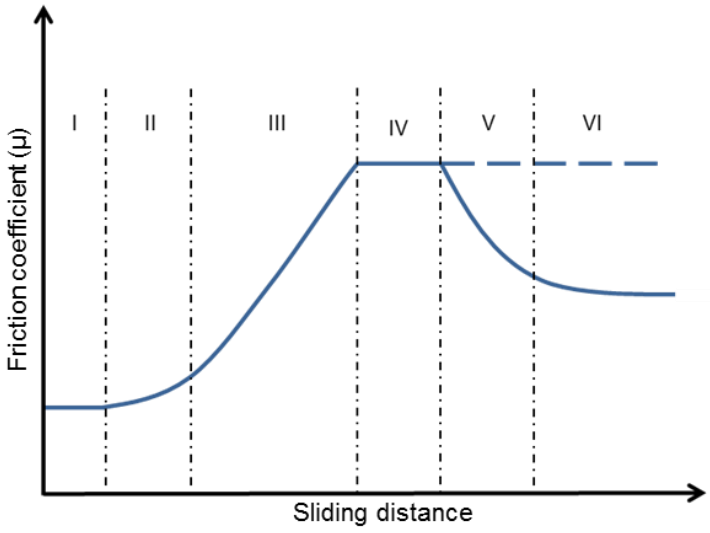


Figure 2.11: Development of friction coefficient with sliding distance [49].

At the start of sliding, when two newly machined surfaces are placed together, they only touch at the highest asperities. At this point the actual contact area is small [51]. The contact area is increased when the surfaces are fitted together, meaning that the asperities are gradually removed. This process is characterized with generation of a large amount of wear particles. The influence of wear debris on the friction and wear of the coating was also studied by Suh and Sin [49]. They showed that in steel contact in crossed-cylinder experiments, the removal of wear debris in the wear track results in a decrease of the friction coefficient. The initial value of the coefficient of friction is reached after a certain sliding time in which new debris are created (Figure 2.12).

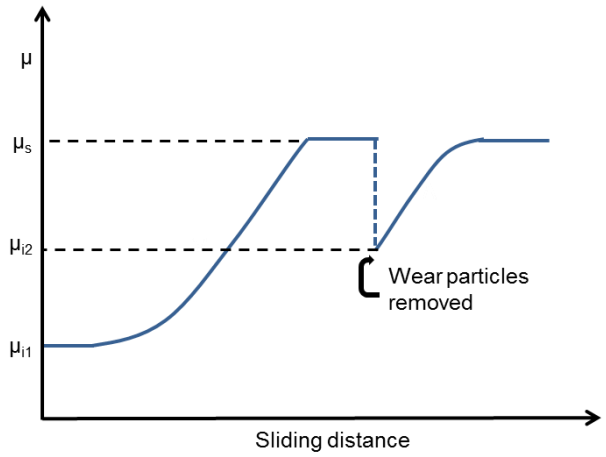


Figure 2.12: Effect of removing wear particles [49].

More recently, Singer et al. [52] focused on wear debris influence on friction in sliding contact for low-friction protective coatings. By in-situ observations he confirmed that the formation of third bodies between the sliding surfaces controls the friction and wear processes providing long lifetime for the low-friction coatings. The **running-in period** is an initial stage of friction, some kind of frictional transition which depends not only on the material and changes of its surface roughness, but on the whole tribosystem i.e. physical and mechanical properties. Frictional transitions can occur naturally but are more often imposed by the operating conditions. For that in real operation machines (tools) a large amount of care must be invested in an optimized running-in procedure for each individual tribological system. An increase of lifetime up to 40 % for the machines can be achieved by carefully performed running-in [53].
Running-in period includes changes of the surface composition, microstructure, and distribution and size of the third body (debris, tribofilm). It is characterized by an overall time-dependent friction trend i.e. shape of the friction force curve, duration of an individual friction curve feature and the fluctuations of friction. Peter Blau [51] described eight types of running-in friction curve types, presented in Figure 2.13(a-h):

a) **Contaminated surfaces**; a thin film of low friction contaminant is worn off.
b) **Boundary-lubricated metals**; surface wear, with initial high wear rate until the surfaces become smooth.
c) **Unlubricated metals**; similar as in (b), but with subsequent development of debris layer i.e. tribofilm.
d) **Unlubricated oxidized metals**; similar as in (b), but with a more tenacious and protective oxide film.
e) **Coated systems**; systems where fatigue wear process is dominant; wear through the coating.
f) **Clean, pure metals**; change of the crystallographic orientation in some regions. Their reduced shear strength lowers the friction.
g) **Graphite on graphite or metal**; creation of a thin film during running-in period.
h) **Hard coating on ceramics**; change of the roughness and generation of fine grained debris.

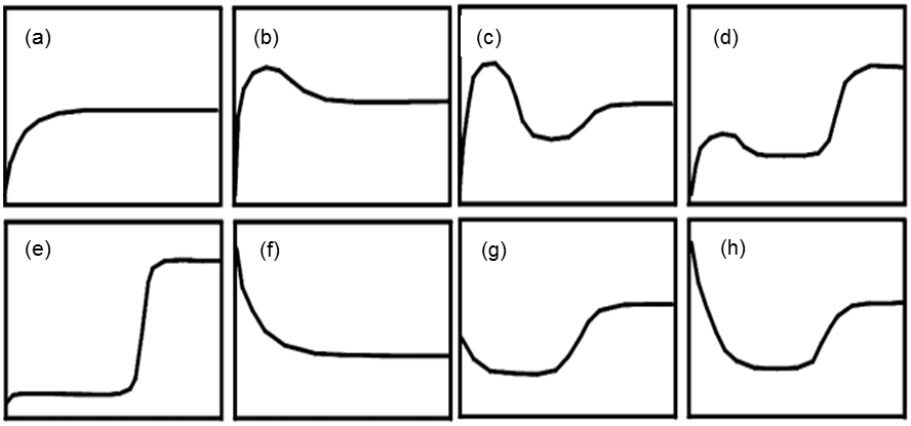


Figure 2.13: Types of friction force curves in dependence of the number of cycles [51].

These curve types were identified by Blau based on tribology literature in the 1980's. It must be emphasized that the curves are not strongly connected to the described system, but can be achieved by different sets of interfacial processes [54]. Several other authors have focused their investigations on the running-in period of different sliding pairs [53, 55-59]. The studies were conducted on metal-metal pairs [60, 61], lubricated systems [58, 62, 63] and coatings [9, 55, 62].

Nevertheless, most of the friction and wear studies have been performed to study the friction force in the steady state period [32, 64, 65]. Usually a comparison between different materials or behavior at different input parameters is presented. Friction with all the parameters that influence the contact between the surfaces forms a particularly complex interaction system.

2.3 Parameters Influencing Tribological Performance of Hard Coatings

Although hard coatings provide an additional protection of the surface of the tools, eventually in tribological applications the protective layer is removed by **gradual wear out** or by the coating **premature failure**. Usually premature failure occurs because of [11]:

- **Coating detachment**
- Large plastic **deformation**
- **Cracking** and **spalling**
- **Pickup** of the counterbody material

To avoid unwanted failure of the protective coatings, the aim of the researchers is to understand the basic mechanisms involved in various tribological processes to help select the appropriate coating and design of the coated surface [66].
Most of the success from researchers has come from the trial and error approach since many material and tribological parameters influence the outcome. Some elements with a major impact on the friction and wear behavior are:

- (coating) materials properties (hardness, coating thickness)
- geometry of contacting bodies
- contact parameters like load, velocity and pressure (distribution)
- surface topography
- environment (humidity, vacuum, lubrication etc.)

The influence of **topography** and **environment** on the tribological properties of hard coatings is in the focus of this thesis.

2.3.1 Topography of Coated Surfaces

Surface characteristics strongly influence the friction and wear behavior especially in the running-in period [55]. The topography of (PVD) coated surface mainly depends on the **substrate material topography** and topography that is induced by the coating deposition processes. The topography of the substrate material can be controlled by surface preparation before deposition such as grinding and polishing. Parts of the (PVD)

deposition process induced topography can be mildly controlled by the rate of etching. This process prior to deposition increases coating adhesion to the substrate but it also creates small irregularities on the substrate – shallow craters and shallow protrusions [6]. These are formed at the sites of metal carbides and non-metallic inclusions. They originate in the steel substrate preparation i.e. ion etch cleaning. Different etching rate of carbides and non-metallic inclusions compared to substrate matrix produce these irregularities (Figure 2.14) [67, 68]. Interestingly, these protrusions have an effect on the final coating topography even in the case of thicker (few microns) coatings.
Very poor control in the deposition process over particles entrapped in the coating can be obtained. These particles produce **growth defects** (GD).

Panjan et al. [69] classified the growth defects and morphology found in hard coatings according to their size as:

- **Nanoscale**: where morphology is determined by the structural growth defects
- **Sub-micron scale**: where morphology is determined by nucleation
- **Microscale**: where morphology is determined by growth defects
- **Macroscale**: where morphology is determined by topography of bare substrate

The morphology features on macroscale were already described in the beginning of this chapter, and nanoscale and sub-micron scale can be efficiently eliminated by energetic deposition techniques or processes where adatom mobility at the substrate is sufficiently high. Microscale growth defects produced in PVD deposition systems, especially those created in magnetron sputtering will be described in more detail.

2.3.1.1 Growth defects in magnetron sputtered hard coatings

The (PVD) coated surfaces are never perfect. In magnetron sputtered hard coatings different growth defects which influence the coating topography can be found (Figure 2.14).

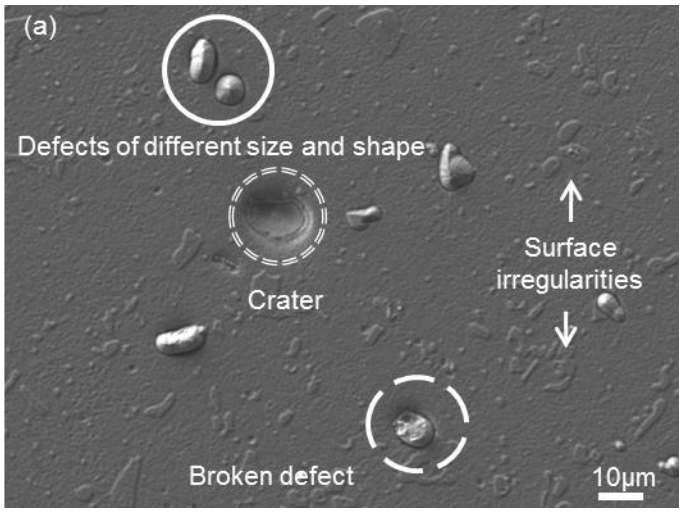


Figure 2.14: Different growth defects and surface irregularities on the hard coatings surface [68].

The growth defects are non-uniformly distributed over the coating surface and depth, while their form, size and density depend on deposition conditions [69]. Growth defects originate from surface irregularities or the particles that are caught on substrate during coatings growth [69-72]. These particles are often called **seeds** and are essential for growth defect growth. The **geometrical shadowing** effect of the seed causes the GD to grow [73]. The coating covers the seed and because it grows faster at seed side relative to bulk deposit, it forms a **nodular defect**. As shown in Figure 2.15 the seed can be of a different shape and origin (a, d) and can start the growth of the defect at different stages of coating growth.

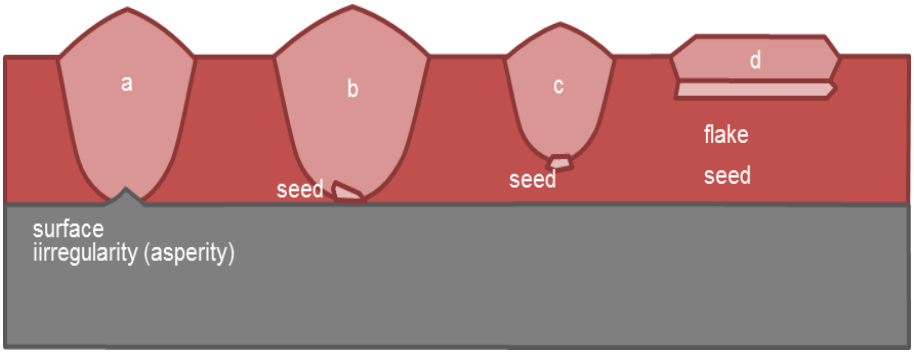


Figure 2.15: Different sources of growth defects. In (a) the substrate surface irregularity or in (b-d) foreign particles in the form of seed at different growth stages can cause the defect growth.

The consequence of such defect generation mechanism is that the defect density depends on the deposition process parameters. Longer deposition times yield higher defect density, since more seeds can be incorporated into the coating [74]. This is seen in Figure 2.16 where a large amount of samples prepared at different coating times were analyzed using stylus profilometry.

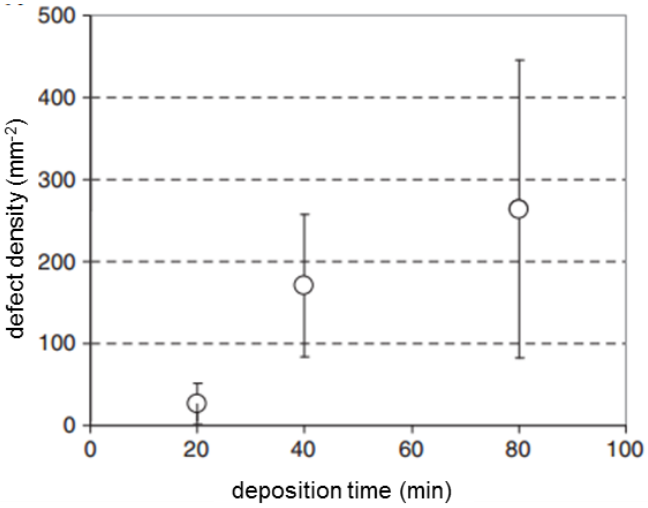


Figure 2.16: Nodular defect density as a function of deposition time [74].

Interestingly, the analysis of 50 different batches each with three samples at the same position but different rotation and thus different thickness revealed that there is no significant difference in nodular defect density.

Panjan et al. [74] compared the defect density among different coatings (target materials) produced with different deposition systems. The results are presented in Figure 2.17. Coatings in Figure 2.17 (a) were produced using thermionic arc evaporation while coatings in (b) were produced in two different unbalanced magnetron systems. The results show that the CrN coating prepared by thermionic arc process exhibits the smallest GD density in comparison with TiN coating. The authors suggest that the reason for that is in material since the chromium sublimates from crucible, while the titanium evaporates [74].

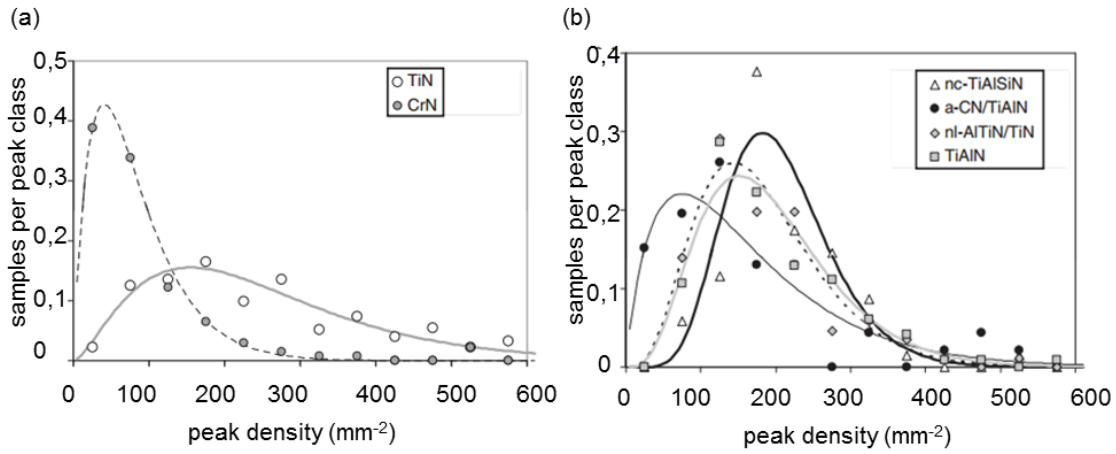


Figure 2.17: Peak density distributions for: (a) TiN and CrN hard coatings prepared by thermionic arc evaporation and (b) sputter deposited double layer a-CN/TiAlN, TiAlN, nl-AlTiN/TiN and nc-TiAlSiN. All coatings were deposited on hard metal substrates [74].

In Figure 2.17 (b) the coatings were produced using two unbalanced magnetron systems (UMS), UBM1 and UMB2. The main difference between both systems is that the UMB2 uses the hollow anode unit which produces more intensive plasma during the etching and the deposition steps. The deposition system UBM2 is also equipped with larger sputter sources than the UBM1 system, therefore a higher total power is used. Even though there are differences in deposition systems, no significant difference in distribution of GD prepared by sputtering in deposition systems UBM1 and UBM2 was noticed. The lowest peak count was detected in a-CN/TiAlN coating. This was assigned by the authors to the lower total power that is used in deposition of the carbon coatings.

Comparing deposition systems, the coatings deposited by thermionic arc evaporation exhibit less defects than the sputter deposited coatings [74].

2.3.1.2 Classification of growth defects

General classification of growth defects can be made by dividing them into two large groups. The first are the **nodular growth defects**, these are defects which are higher than the mean level of coating surface and the second are **cavities**. The peak density is in the range of 100–500 per mm^2 while the number of cavities is lower by an order of magnitude [74]. Panjan et al. [69] made the classification of the growth defects according to their geometrical shape or seed source.

a) **Defects in the form of flakes**: These are loosely-bound defects that form at the asperities or other particles. They can be easily removed due to thermal and internal stresses. A gap can appear between the coating and the defect due to the deformation of the seed. Typical size is 5–40 μm (Figure 2.18(a)).
b) **Open void defects:** A loosely bound particle flakes off during the coating growth or cooling stage due to compressive stress or thermal stresses. This causes the formation of through-voids on the coating surface (Figure 2.18(b)).
c) **Cone-like defects:** These are small defects with a round, cone-like shaped tip. Their origins are small particles, 100-400nm in size, which flake from the chamber components. Usually these particles have the same composition as the coating as they originate from chamber components (Figure 2.18(c)).
d) **Pin-hole defects:** These are narrow holes that extend through the whole coating. They are generated at the substrate cavities which are formed during the polishing process [75]. The narrow cavities cannot be closed-covered completely by the thin coating due to shadowing effect. The deposition rate on the sides of the cavity is much smaller than on the flat front side of the substrate. This creates the pin-holes. They can be open if the hole is large or closed after some certain deposition time if the holes are small enough (Figure 2.18(d)).
e) **Defects in the form of microdroplets**: Microdroplets are generated by arcing. The probability for arcing is increased with the contamination of targets and

substrates [75]. Arcs generate droplets of molten material which are incorporated into the coating during growth. Micro-droplet defects are characteristic for cathodic arc evaporation systems (CAE), but can also be found in other deposition systems.

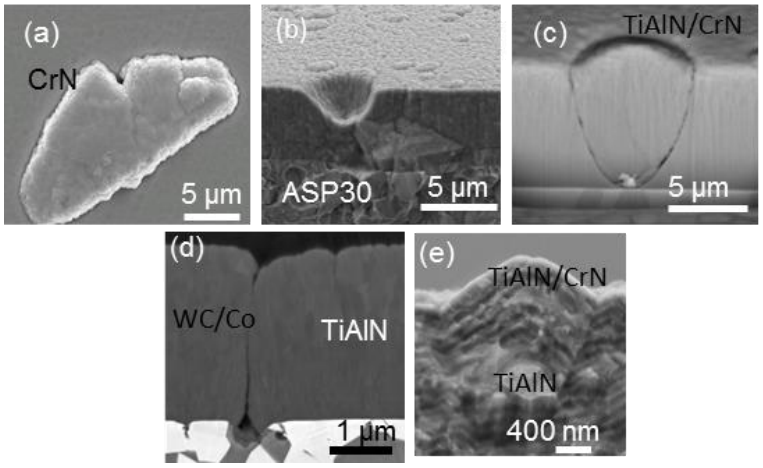


Figure 2.18: Different growth defects according to classification (a-e)[74].

Cavities or open void defects are by origin related to nodular defects. Münz et al. [76] described a possible mechanism for the creation of cavities in coatings (Figure 2.19). This model postulates that the arc generated droplets have a low adhesion to the substrate. As droplets are caught on the substrate they generate nodular defects in the coating growth process. During coating growth the compressive forces build up in the coating. Due to the created stress and poor adhesion of the droplet to the substrate the defects self-propel. This creates an open void all the way to the bare substrate. Depending at which stage of the deposition process this happens this void can be totally closed, if it happened at the start of the coating growth process, or can be partially covered, with a thin porous layer covering the substrate at the crater bottom.

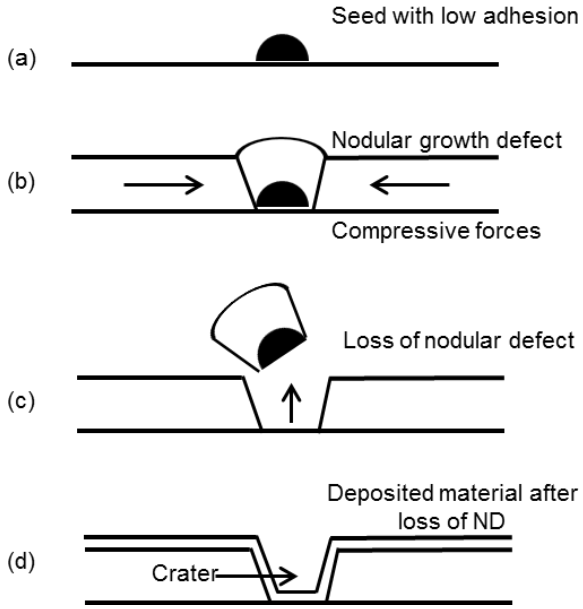


Figure 2.19: Self-propulsion model. (a) Landing of a droplet on the substrate, (b) growth of the nodular defect, (c) loss of the nodular defect due to compressive forces and (d) crater creation [76].

This principle was applied by Münz for cathodic arc deposition droplets, but can also be applied to magnetron sputtered growth defects with low adhesive contamination seeds.

2.3.1.3 Growth defect sources in magnetron sputtering systems

Although it is impossible to deposit a coating without any growth defects, it is possible to reduce the GD density by high-quality substrate cleaning procedure, periodical cleaning of all components within the vacuum chamber and with the use of shields in front of magnetron targets. The deposition system is a large source of particles (seeds), especially the substrate holders and heaters which are covered by coatings from previous batches [74, 77]. The coatings on these inner vacuum chamber parts are subjected to extensive heating and thus the thermal stress which causes the coating cracking and delamination in the form of chips. The chips are then transferred to the substrate surface and incorporated into the coating growth [70]. In Figure 2.20 common sources of growth defect seeds are presented. Particles can be generated from the target due to contamination with nonconductive inclusions or target poisoning effect (undesired oxidation or nitration of the target) which causes the arcing. This generates large droplets of molten material that start the growth of the defects. Another problem are the moving parts in the deposition system where wear particles are generated, or the pressure variations caused by high pumping speed that picks up the fine dust particles [75, 78].

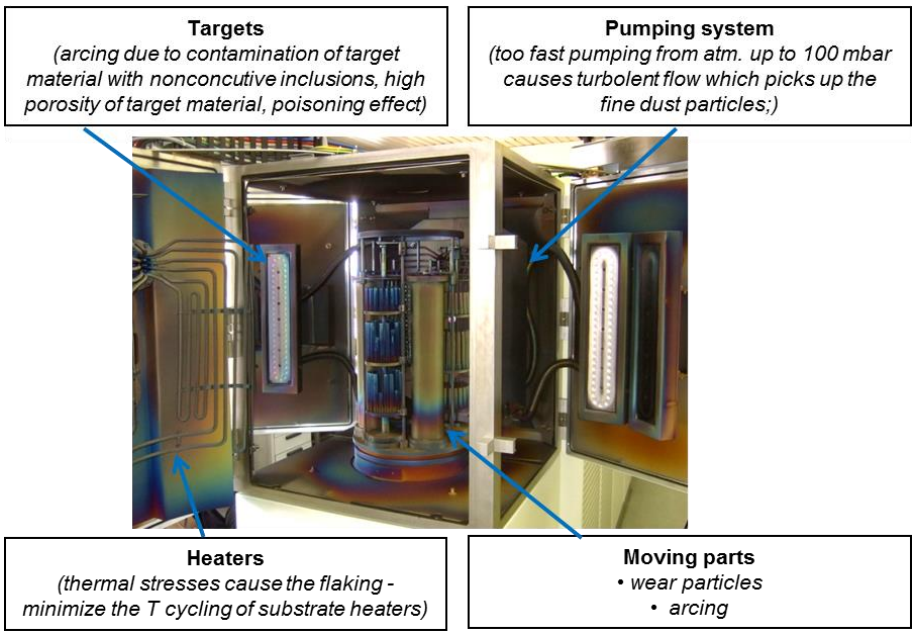


Figure 2.20: Common growth defect sources within the vacuum chamber.

2.3.1.4 Influence of surface topography on tribological behavior

The topography of the surface influences the stress distribution in a coating at different levels below the contact surface [11, 79] (Figure 2.21). The highest contact stress is located at the asperities, hence to minimize the stress, the coating surface should be as smooth as possible. Even at low average stress the stress peaks may cause the plastic deformation of the asperities i.e. generation of wear debris at the contact.

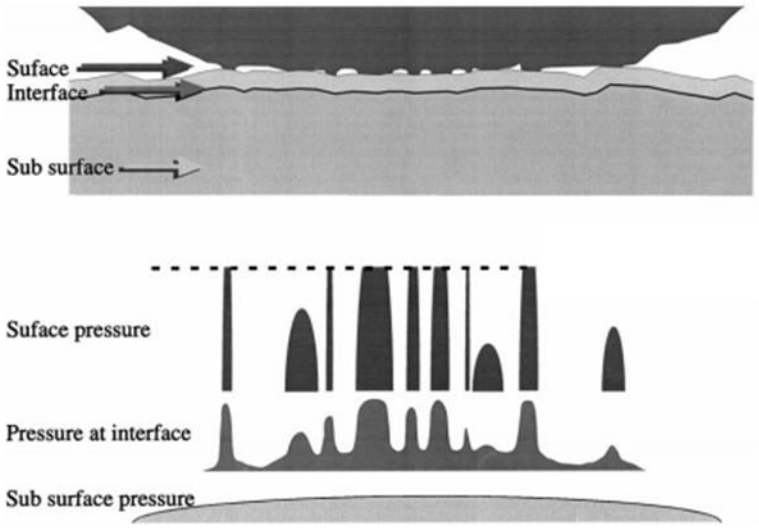


Figure 2.21: Pressure distribution between rough surfaces [11].

Generally, a tribological system invokes both plastic and elastic deformation of asperities with the latter component being significantly higher [80]. Nevertheless, this means that during sliding, especially during running-in, the surface undergoes dramatic changes in topography, i.e. amplitude distribution of the profile (Figure 2.22). This was shown by several authors [80, 81].

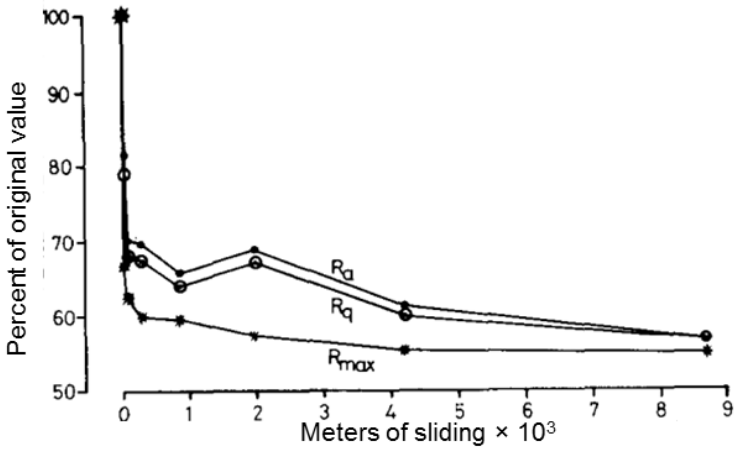


Figure 2.22: Changes of R_a, R_q and R_{max} parameters during sliding [81].

In Figure 2.22 R_a denotes center line average roughness, R_q the root mean of R_a and R_{max} the difference between highest peak and the lowest valley of the line profile. We can notice that the major topographical changes happen in the first meters of sliding. The changes occur in both dry and lubricated conditions. Changes in surface topography and high wear rate during operation in dry conditions make the studies of how the topography parameters influence friction behavior extremely difficult [82]. During tribology tests or a tool real operation, the coating topography changes include smoothening or roughing of the interface, formation of micro-cracks, phase transformations, deformation hardening, formation of oxides, formation of solid films by reactions with lubricant additives, transfer of material from the counter surface and tribofilm formation [83]. Experiments nevertheless show that surfaces with lower roughness exhibit a lower COF [82]. To observe the changes of the interface in real time, the in situ tribometry was developed. This method has been extensively used to study the formation of a tribological film in DLC coatings and subsequent low friction [57, 84]. Though this method can provide useful information about the tribological film growth and chemical changes if in-situ Raman spectroscopy is also used [85], it cannot provide this information in a system with realistic counterbody materials.

Extensive studies have also been done to study how the topography (coated or uncoated) influences the tendency of material transfer or galling [5-7, 11, 67]. Carlsson and Olsson [86] showed how droplets and dimples strongly influence the tribological performance of DLC coating. It was shown that polishing decreases the amount of pick-up material. The friction coefficient is also smaller with the use of polished DLC coatings. Harlin [67] stated that the material pick-up is mainly controlled by abrasion action of the hard coating asperities thus polishing of the coating reduces the abrasion factor hence smaller material transfer. Podgornik at al. [7] studied how cold work tool steel surfaces prepared in different ways influence the material galling. Additionally they investigated the effect of surface roughness and post-polishing on galling resistance of TiN and DLC coated surfaces. Interestingly, they found that the galling resistance and influence of surface roughness and topography depend on the type of coating too. In TiN hard coating the combined effect of high shear strength and very hard surface any increase in surface roughness leads to a major decrease in galling resistance as shown by Podgornik [7]. He also mentioned that any droplet formed during coating deposition will have an additional detrimental effect. In contrast, at low friction coatings anti-galling properties against stainless steel start to prevail over the negative effect of surface roughness. In general, studies show how the topography of different coatings or bare materials influences the tribological behavior [87]. When softer against harder materials are used the surface topography influences the tendency for material transfer. Surfaces with lower protrusions also exhibited a faster friction decrease, i.e. a faster running-in.

In the literature, studies focusing on the PVD growth defect role in the tribological contact are rare [55, 88]. Therefore, in one part, the aim of this work is to enlighten the view on tribological properties of hard coatings through topographical features whose detailed studies are lacking – (PVD) nodular defects.

2.3.1.5 Role of growth defects in coatings

The growth defects in hard coatings can cause problems in industrial applications. Therefore the formation of defects is undesirable. The deposition system influence on defect density was already mentioned. In cathodic arc evaporation (CAE) there is the largest defect density. The arcing process produces a large amount of droplets - molten target material which solidifies during the flight to the substrate. The detrimental effects of macro particles include the local loss of coating adhesion, surface roughening and grain coarsening, non-uniform nitrogen and phase distribution within the particle, and the formation of shrinkage porosity due to droplet self-repulsion mechanism [89]. Defects either from CAE or magnetron sputtering definitely affect the overall coating performance. How to reduce the growth defect density in the case of magnetron sputtering was already described in Chapter 2.3.1.3.

The most detailed studies of the growth defects have probably been done in optical coatings [90-92] and corrosion studies [93, 94]. Damage in **optical coatings** caused by laser was first associated with the presence of the nodular defects. Their lens-like shape caused the light to focus within the defect and caused reflective index variations. In thin protective optical coatings used in computer hard discs the defects cause uncontrolled changes in surface roughness. As presented in Figure 2.23 the growth defect density increases the roughness of the coatings. In microelectronics, defects are the cause of electrical short circuits [95]. Another problem is the **permeation** through defects in barrier coatings. Transport barrier coatings are of increasing interest in food packaging and other industries. The use of such coatings decreases the permeation of gases by several orders of magnitude.

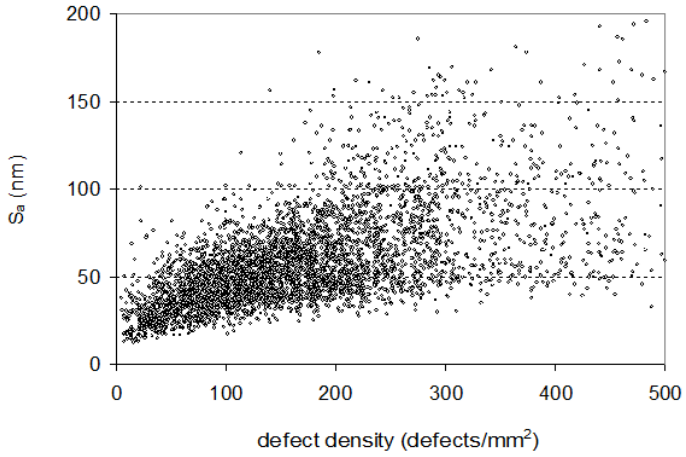


Figure 2.23: Surface roughness: correlation between the growth defect density and the coating surface roughness [74].

The growth defect role in hard protective coatings may not be as crucial as in optics but it is also an important factor determining the coating quality. Growth defects act like stress raisers, they can increase the friction coefficient, increase the permeability for gases and decrease the wear and corrosion resistance of the coating. The latter is one of the major applications of the hard coatings since hard coatings possess high chemical inertness. Growth defects open possible channels or pathways for the corrosion media to reach the substrate. Thus the growth defects decrease the corrosion resistance of the coatings [39, 93, 96]. To do so the nodular defects have to originate from the substrate interface in order to allow the corrosion media to reach the substrate. The defects that start to grow in the middle of the coating do not have detrimental effects. In addition, nodular defects must form channels around them that are wide enough for corrosive media to reach the substrate. In this sense, the craters or open void defects present larger problems for corrosion resistance due to direct and usually wide pathways to the substrate. Fenker at al. [93] described in detail the defects effect on corrosion resistance. If corrosion is characterized by the anodic dissolution of the substrate material with a high anodic current density at localized defect site the corrosion is **galvanic**. At sites of pores and pinholes it is called **pitting corrosion**. An example of pitting corrosion is shown in Figure 2.24a. The corrosive media entered the substrate-coating interface through a pinhole causing the corrosion of the steel. The coating itself was not damaged by the corrosive media.

Through pinholes or channels between the nodular defect and the coating, the **oxygen** can also enter the substrate-coating interface similar as the corrosive media. Therefore defects lower the oxidation resistance of the hard coatings. In Figure 2.24(b) the nodular defect after oxidation of CrN/CrVN multilayered coating at high temperature and oxygen environment is shown. Vanadium diffused to the surface through the channel surrounding the nodular defect and oxidized. Apart from lowering the coatings oxidation resistance, the out diffusion of the vanadium through defects can contribute to reducing friction, but such diffusion must be controlled in order not to affect coatings mechanical adequacy.

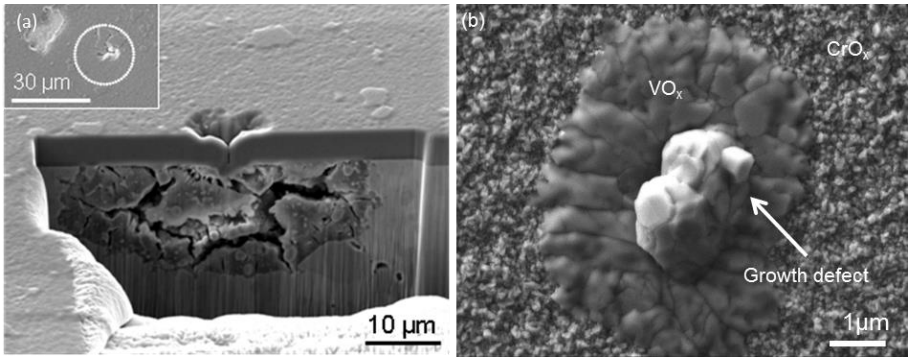


Figure 2.24: SEM images of GD. (a) Corrosion through pinhole and (b) outward diffusion of vanadium oxide at the side of the nodular defect [39].

While most top oxide layer-CrO_x acts as a diffusion barrier, the vanadium from inner layers of the coating can diffuse to the surface through channels surrounding nodular defects or pinholes. In the case of self-lubricating coatings this kind of diffusion ensures a low friction coefficient at high temperatures, but can also lead to premature failures of the coating since high diffusion flow of the material alters the mechanical properties of the coating. In our previous study [39] we suggested that the oxidation process starts at the sides of GD. Therefore some control over defect density must be achieved so that the controlled out-diffusion processes happen, as required in the case of solid lubrication coatings that limit the structural changes of the coating itself.

The influence of the growth defects, particularly of the nodular defects in tribological applications, is not well reported. A recent major study was conducted by Luo [55]. He studied the running-in period in TiAlN/VN multilayered coatings against an alumina counter body and identified three stages of friction. In the first stage the friction is low – the initial sliding contact involves a limited number of asperities (nodular defects). In the second stage (10–20 cycles) the friction coefficient increases due to the fracture and spalling of the nodular defects. During this stage, the wear particles are formed from nodular defects that become entrapped in the sliding contact. The particles are then exposed to a sliding/rolling motion under the applied loads. This motion causes abrasive wear of the counterface, scratching of the worn coating, breaking of the particles into smaller fragments, and the adhesive attachment of fine fragments onto the parent surface of the coating. This stage in the wear process was observed to continue until the nodular defects were leveled with the coating surface. In the third stage (>50 cycles), a steady-state friction is maintained. In this sliding period the conformal "three-body" sliding contact is formed. The steady-state wear is found to be significantly influenced by the initial coating roughness [63]. Tkadletz et al. [88] studied the effect of CAE droplet growth defect on the wear behavior in dry sliding. His conclusions were that wear was not severely affected by growth defects. But under load the defects break and release the droplet fragments that can act as abrasive media. Although the studies reveal some principles of defect induced friction and wear behavior, no systematic study has been conducted on magnetron sputtered defects. In addition, no study has been done about the role of defects in sliding against industrially adequate materials.

2.3.2 The influence of environment on friction and wear

While the topographical features have an effect on tribological performance especially at the beginning of the sliding, when the contact between surfaces is not conformal, the tribological behavior can also be severely influenced by the environment. Not only as the use of different cooling and low friction oils and additives but also as the humidity, temperature and oxygen-to-nitrogen ratio at the tribological contact.
Generally the environment influences the performance of the tribological system by [97]:

1. A **formation of an adsorption layer** between the sliding surfaces leads to a lower coefficient of friction. Such an effect can be best observed when sliding in vacuum where the adsorption process is disabled. In such conditions the bonding between the two surfaces is strong due to fresh surfaces with dangling bonds exposed by sliding.

2. **Change of mechanical properties** caused by adsorption. Especially the adsorbed water molecules, or corrosive media, on the surfaces can cause changes at the surface that influence the mechanical performance of the surface.
3. **Tribochemical reactions** cause the formation of different chemical products. These products on the surface or in the form of debris influence the surface performance.

As noticed, the main mechanism that causes the changes in tribological behavior at laboratory conditions is the adsorption of water or gas molecules on the surface. Absorbents on the surface can participate in surface chemical reactions, or can act as a binding media for wear debris collection, material transfer and tribological film formation. It is not necessary for relative hardness of the coatings to play a major role in the prediction of friction and wear properties, the main role in determine the wear/friction may be the tribological oxidation and subsequent wear of the thin tribo-oxide layers. The major impact in tribological surface oxidation is from the composition of the coating, test conditions such as temperature, sliding velocity and normal load, and surrounding environment in the form of oxygen amount at the contact and humidity.

For the oxidation to occur, a sufficient amount of oxygen and energy in the form of heat must be available. Temperature at the contact region is higher than the test ambient temperature. This is due to dissipation of friction energy at the contacting asperities. The temperature rise can be several hundred degrees higher than the ambient temperature, but just for a short time and at a limited small area i.e. **flash temperature** [48]. The temperature at the contact increases monotonically with the surface roughness hence the surface parameters such as height and spacial distribution of asperities influence the contact temperature. The exact temperature at the contact is hard to measure [48], but there are several models developed that relatively successfully predict the temperature [98, 99].

In addition to temperature, the composition of hard coating (type) and relative humidity at room temperature test play crucial roles in oxidation kinetics and thus friction and wear behavior of the hard coatings. Köcker et al. [100] studied the influence of different test parameters on the tribological behavior of TiN, TiAlN and CrN PVD coatings. Depending on the ambient medium, relative humidity, sliding distance or velocity, very different friction and wear coefficients can be observed. He noticed that low sliding velocity exhibits low wear of CrN and TiAlN coating. With increasing velocity the wear is increased in case of CrN coating but not in case of TiAlN. Wear decreases with velocity in case of TiN coating. Upon changing the relative humidity Köcker reported that TiAlN coating best performance was obtained at dry conditions (2 % RH) while CrN coating wear resistance increases with relative humidity. TiN exhibits a high wear rate at low RH which increases with increasing RH. The friction coefficient is low and remains low with higher RH for CrN, the TiAlN COF is low at low humidity and it increases with humidity, while TiN COF does not change with relative humidity [100]. The same experiments were also conducted in a dry nitrogen atmosphere. The friction and wear behavior for CrN and TiAlN coatings are similar to dry air experiments. The experiments with TiN coating show constant COF values with up to 10 times smaller wear than in dry air experiments.

TiN and TiAlN coating tribological oxidation was studied the most intensely. Their tribological performance is attributed to the formation of thin tribo-oxide layers that consist of TiO_2 and TiO_xN. Depending on the environment (RH) the formation of rutile or anatase form of TiO_x oxide can occur [101]. The rutile is formed at high humidity. The hydrated layers of TiO_x in combination with debris act as a lubrication layer which leads to a lower friction observed in the experiments [43, 100, 101]. For TiAlN it is known that hydrated oxides can form on the surface during longer storage in ambient air conditions [101, 102]. Wilson [47, 103] conducted experiments for TiN sliding against high speed steel (HSS). He produced wear map regimes and studied the effects of humidity. He found out that the humidity assists oxidation and wear which is also common for many ceramics in similar conditions.

Similarly, the alumina can react with water at the interface to form aluminum hydro-oxide [43]. At low humidity the anatase form of oxide is formed. In combination with loose abrasive debris in the contact region this produces higher COF [104]. Wit et al. [105] performed TEM studies of wear debris which showed that crystalline or amorphous debris can be formed when sliding with Al_2O_3 counterbody depending on the test conditions and relative humidity.

For low friction at pure nitrogen atmosphere, when testing TiN/TiN pair there is no available chemical explanation because of absence of (hydro-)oxide layers that could enable easy shareable plains between oxide and coating/counterbody material [100]. This triggers the urge for further studies. Moreover, the more advanced nanolayered hard coatings based on aluminum or vanadium have not been extensively studied at different atmospheres. Therefore the literature in this field is scarce. These coatings, due to their excellent anti wear and low friction properties, show great possibilities for their use in different industrial environments; therefore the studies of friction and wear behavior induced in different environments are mandatory.

Chapter 3

Experimental Methods

In this part experimental methods for coating deposition and characterization will be described. Some results, which are not crucial for the workflow of this dissertation, will be also presented in this chapter.

3.1 Hard Coating Preparation

All our hard coatings were prepared on D2 tool steel substrates, coated in an industrial scale unbalanced magnetron deposition system.

3.1.1 Substrates

D2 tool steel was used as a substrate material for the investigation of the influence on tribological properties of nodular defects in magnetron sputtered hard coatings, and the influence of atmosphere on tribological behavior of coatings. D2 tool steel is a high carbon, high chromium type tool steel that is quenched at 1040 °C followed by oil, warm bath (500-550 °C) cooling. Hardness achieved after quenching is 62-64 HRC. Steel was then tempered at 500 °C in oil. After this the steel has 58 HRC or 700 HV.
For residual stress measurements in the deposited hard coatings we also used silicon wafers.

D2 tool steel samples were cut in a shape of a circle plate with a radius of 15 mm and thickness of about 3 mm. To ensure good adhesion of a hard coating all the steel samples were mirror-polished (10–20 nm), and cleaned in ultrasound bath using different chemical detergents. After soaking in detergents the samples were rinsed with deionized water and dried with hot and clean air. Final cleaning was done in the deposition chamber by ion etching with argon and krypton ions.

3.1.2 Deposition of hard coatings in industrial magnetron deposition system

Hard coatings used for the purpose of tribological tests described in this thesis were deposited using the CemeCon CC800/9 industrial deposition system. Schematically the vacuum chamber of the system is presented in Figure 3.1. This system uses four unbalanced magnetron sources positioned at each corner of the chamber. Each magnetron source has a (segmental) planar target which is used for sputtering. By using different target materials the deposition of multilayer coatings is possible.

In the middle of the chamber there is the turntable with substrate towers. Each of these towers has smaller substrate holders vertically arranged which are designed for different tools such as drills.

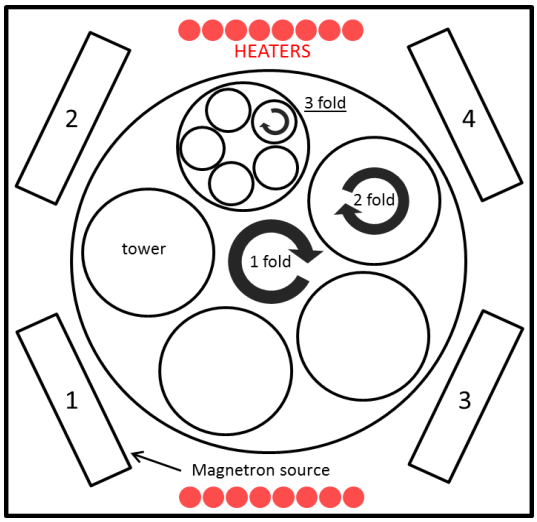


Figure 3.1: Scheme of the CemeCon deposition system vacuum chamber.

Turntable with towers and substrate holders enables the three different rotations as depictured in Figure 3.1.
The deposition process is composed out of different stages.

Pumping and heating
In the first stage the vacuum chamber is pumped down to the pressure of 4 mbar. The CC800/9 uses a rotary pump to reach rough vacuum and the turbo-molecular pump for high vacuum. At set pressure the infrared heaters heat the chamber to a set temperature of 450 °C.

Ion etch cleaning
In the next stage the samples are cleaned by ions i.e. **ion etching**. The deposition system CC800/9 enables two types of plasma cleaning. The first is middle frequency cleaning (MF) which is used to clean non-conductive impurities on the substrates. The second is the so-called booster etching which is more intense. On average about 200 nm of material is removed in 40 minutes of ion etch cleaning process.

Sputtering
The last stage is the coating deposition by magnetron sputtering. On all four targets a negative voltage is applied, and a positive voltage is applied on booster. In this case the targets act as cathodes and the booster is an anode. The turntable is on negative potential (–100 V). The gases (mixture of argon and nitrogen gas: 150 mln: 70 mln, respectively) are fed into the chamber through the booster where the gas atoms get **ionized**. In such a way a relatively high ionization is achieved. The plasma is confined in the area between the targets and the booster and also spreads to the area of the substrates.

Magnetrons have permanent magnets behind each target. The magnetic field forms a closed loop which traps the electrons close to the target. These electrons are then further used for ionization of the gas atoms close to the target. Ions are then accelerated towards the negatively charged target. They cause sputtering upon hitting the target material. The deposition of the coating is achieved when sputtered target atoms condense on the substrate.

3.1.3 Magnetron targets

Depending on the PVD process different targets can be used. In general, a high purity target that is at least the same size as the substrate is needed to enable a uniform coating. The development of targets has gone parallel to the development of coatings. For deposition of metals elementary targets are used. By using reactive gas (e.g. nitrogen) during deposition we can obtain compound coatings such as TiN. The other way to obtain this coating would be to use a TiN target, which is technically more difficult while deposition rate is much lower.

Coatings such as TiAlN or CrAlN can be obtained either by using several high-purity **elemental targets** or **segmental targets** can be used. Such targets are made of one material and then subsequently one or more different sputtering materials are added (incorporated). The composition of the obtained coating is not identical to that of the segmental target, since there is a difference of sputtering yield for materials used in the target. For the purpose of this thesis the targets for deposition of TiN and CrN coating were pure metal targets, and for deposition of TiAlN the titanium metal targets with plugs made from aluminum were used.

For the deposition of CrN/CrVN and CrN/CrAlN we used specially designed targets **(i.e. gradient targets).** These are formed from two triangular-shaped individual targets; hence the name "triangular" target is also used. One part of the target was made of chromium and the other part was made of either vanadium or aluminum. By using two sets of these targets plus two conventional segmental targets we were able to produce CrN/$Cr_xV_{1-x}N$ or CrN/$Cr_xAl_{1-x}N$ multilayered coatings. The thickness of individual layers and overall composition of the hard coating produced in this way differed, depending on the vertical position of the samples (see Figure 3.2). Ten samples were arranged in a vertical line covering the whole composition range. How the composition changes due to sample position and hardness measurements are presented in the following sections of the thesis.

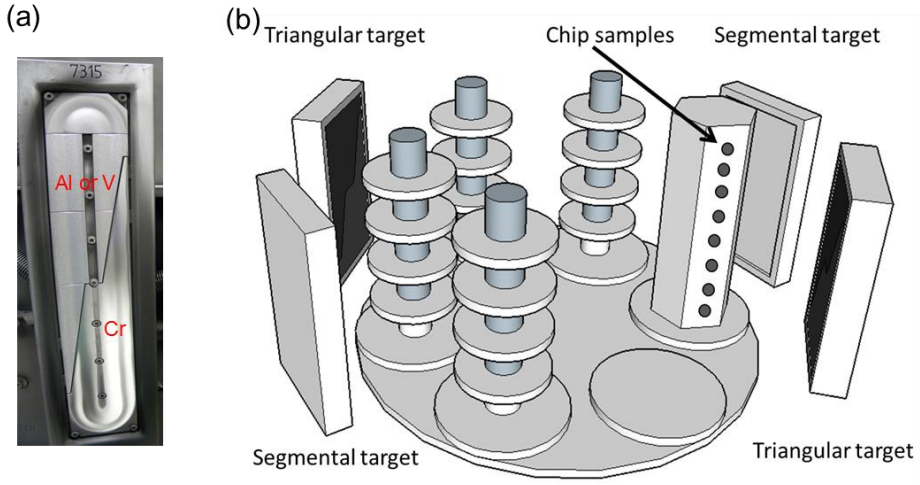


Figure 3.2: (a) Triangular target and (b) scheme of deposition system. Sample positions and target arrangement for deposition of CrN/CrVN and CrN/CrAlN advanced multilayer coatings.

3.2 Crystal Structure and Microstructure Characterization

3.2.1 X-ray diffraction

A common technique for analyzing the crystal structure of hard coatings is the X-ray diffraction (XRD). It is a non-destructive and rapid method in which the samples are mounted on a goniometer and gradually rotated while being illuminated by X-rays. The commonly used geometry to obtain X-ray patterns is Bragg-Brentano. By this method the incident angle changes and it is equal to the detector angle. The output data consists of reflections from the crystal plains which are parallel to the substrate.

We used X-ray diffraction to confirm the structure of the hard coatings and to observe lattice parameter changes as the content of aluminum and vanadium changed in CrN/CrAlN and CrN/CrVN hard coatings, respectively. The spectra were measured by Bruker AXS D4 Endeavor presented in Figure 3.3 (a).

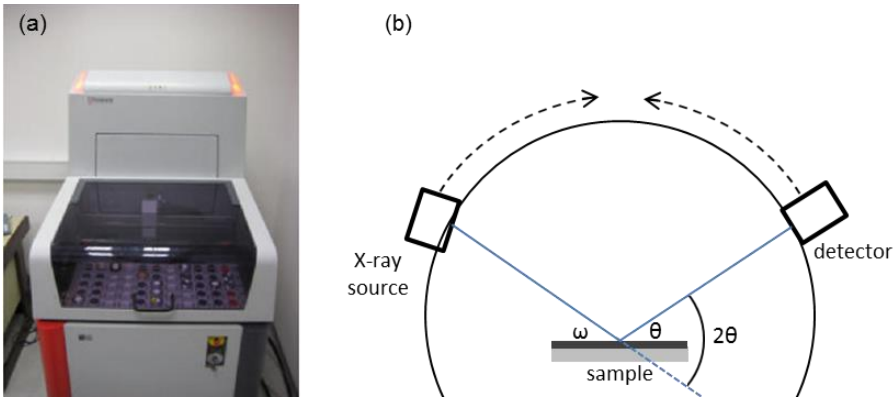


Figure 3.3: Image of XRD apparatus: (a) Bruker AXS D4 Endeavor and (b) schematic presentation.

X-rays are generated by deceleration of electrons in the anode; the generated X-rays are directed to the sample. To obtain the diffraction spectra the Bragg condition for constructive interference must occur:

$$n\lambda = 2d\sin\theta \,, \tag{3.1}$$

where λ is the X-ray wavelength and d is the distance between crystal lattice planes.

3.2.2 Scanning electron microscope and focused ion beam microscope

For surface morphology, and characterization of wear tracks and different growth defects the scanning electron microscope (SEM) and focused ion beam (FIB) microscope were used. We used either Jeol JSM-7600F scanning electron microscope or Helios NanoLab 650 dual beam focused ion beam microscope.
In SEM, the electrons are generated in an electron gun. As the electrons pass across the condenser lens, they are focused in a thin beam which is deflected by coils to scan the surface of a sample. The interaction of the electrons with the sample causes the emission of secondary electrons (SE), back-scattered electrons (BSE) and characteristic X-rays which are then collected by different detectors to form an image. Analyzing volume depends on the type of the detected particles, energy of the incident beam (acceleration voltage) and atomic number of the material of interest. Secondary electrons are the most commonly collected to form an image. The reason for that is that the SE are weakly bound electrons from the outer atomic shell therefore the energy for their emission is low. Consequently their energy is low, meaning that they are collected within a few nanometers of the sample surface. The slight disadvantage of the SE is that their number is independent of the sample material therefore the image does not give any compositional contrast.

Compositional contrast can be obtained by the collection of BSE. The number of BSE in contrast to SE strongly depends on the atomic number of the material. BSE are elastically and inelastically scattered electrons, which leave the sample surface. Heavier elements scatter more strongly than the lighter elements; hence the compositional contrast image can be obtained. The difference between the SE and BSE electron image is presented in Figure 3.4 where the same nodular defect was imaged by SE and BSE, respectively. On the BSE image we notice a bright ring in the middle of the broken off defect. This indicates that the material of the ring is different than the surrounding material. On the SE image the ring is poorly visible because SE are not sensitive to the atomic number of the material.

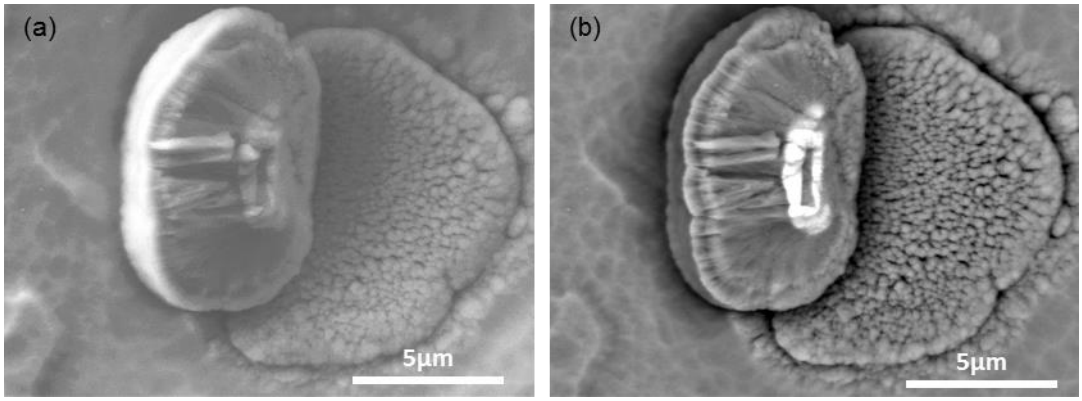


Figure 3.4: SEM images of nodular defects collected with different electrons. (a) Secondary electron image and (b) back-scattered electron image of the same nodular defect on TiAlN hard coating.

More advanced scanning electron microscopes are equipped with a focused ion beam source. In Helios NanoLab 650, the FIB column is incorporated into the SEM microscope at 52° angle with respect to the SEM column. The advantage of such dual system is that FIB can be used on samples inspected by SEM without changing the microscope system. A FIB is used for in-situ milling on the specific area.

The milling is done by gallium ions which are created from the evaporated gallium solid source. Precise etching can be used to produce cross section views of the material which is especially useful in coatings for investigation of the sub-surface characteristics such as crack propagation, growth defect cross sections and transmission electron microscope lamella production. Ions can also be used for the deposition of different materials on the sample surface. This is done by precursor gases which disintegrate upon interaction with heavy ions and condense at selected areas. The small coated areas protect the surface of interest and improve the quality of the cross sections. At small ion currents it is also possible to do ion imaging. The ions produce electrons when they interact with the surface, which can then be collected by different detectors. Images obtained by ions usually have a better compositional contrast than those obtained by the electrons. However, the image must be obtained quickly due to constant etching of the material. The difference between these two imaging modes is shown in Figure 3.5. In ion image (b) the contrast between different compositions and orientations is clearly visible in the D2 substrate. The topmost layer consists of platinum deposited by ion beam. This protects the surface layer and reduces the so-called curtain effect, producing a smooth cross section interface.

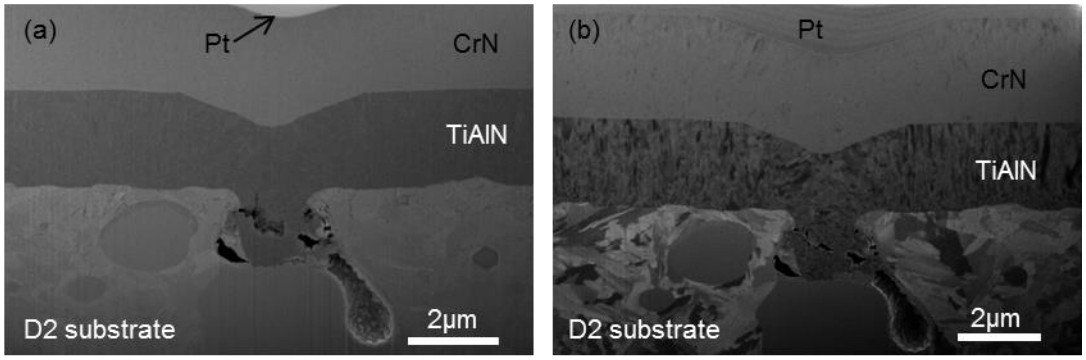


Figure 3.5: SEM image of coating cross section. (a) Obtained by secondary electrons in standard SEM and (b) secondary electrons induced by ions using FIB.

The SEM and FIB microscopes also have an energy dispersive X-ray detector or EDS. This detector uses characteristic X-rays for element detection. It was used for overall coating composition determination and for characterization of the wear products and defect seeds.

3.3 Topography Characterization

3.3.1 Stylus profilometry

For topography measurements of the surfaces and compressive stress measurements the stylus profilometry was used. It is a similar technique as the atomic force microscopy (AFM), a type of scanning probe microscopies. In profilometer, the sensing is done by a diamond stylus which is in constant contact with the surface. As the stylus is moved over the surface, vertical displacements are recorded as a function of the position (Figure 3.6). Tayler Hobson Talysurf Series 2 profilometer is also equipped with a stage that can move the sample perpendicular to the scanning direction. Therefore a 3D topographical image can be reconstructed from a series of line profiles (Figure 3.7 (a, b)).

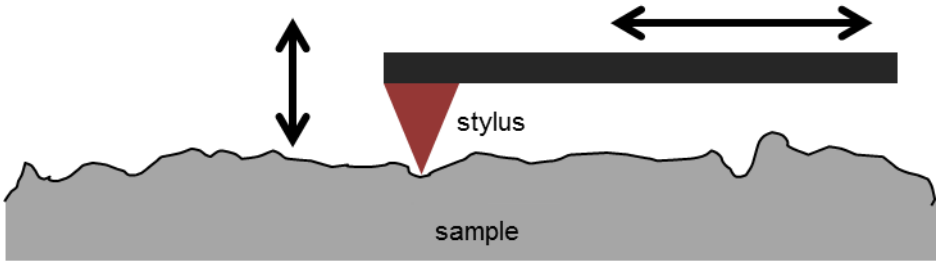


Figure 3.6: Scheme of the profilometer working principle.

All coated samples undergo 3D stylus investigation for determination of defect density. The area of 1 × 2 mm was scanned with a lateral resolution smaller than 0.2 µm. The area was then divided in two 1×1 mm areas from which the average number of peaks above 0.5 µm is calculated. The same condition is taken for the calculation of holes in the sample (–0.5 µm). Some of these results were already presented in Figure 2.17. The stylus profilometry was also used for the determination of wear volume and examination of wear tracks after tribological tests. An example of such a measurement is presented in Figure 3.7 where in (a) the top 2D line profile image is shown which can be transformed into a 3D image. For the determination of mean wear track depth or wear volume, the average of a few profile lines was taken for calculation (c).
The wear volume was calculated by multiplying the wear track length with the average surface of the wear track on the cross section.

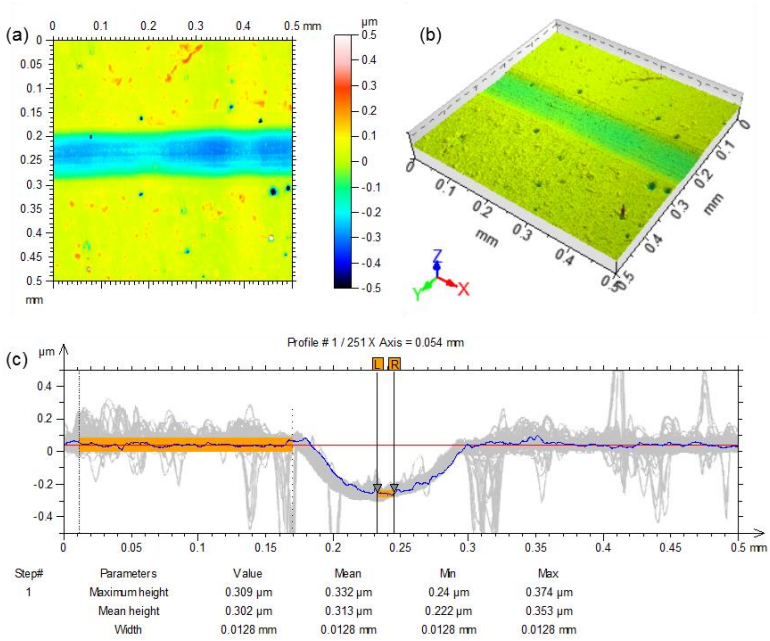


Figure 3.7: Stylus profile images of wear track: (a) 2D profile image that is converted in (b) 3D profile image or in (c) set of individual line profiles.

3.4 Mechanical Characterization

3.4.1 Adhesion measurements

Adhesion of a coating to the substrate surface is one of major parameters for successful application. Hard coating adhesion was tested with CSM Revetest scratch tester where increasing force is applied to the coating surface by a diamond tip. This is a destructive method, which makes a scratch in the coating until the coating failure-detachment from the substrate. Criteria for the coating failure may be the occurrence of the first crack or the first induced cohesive or interfacial fracture (delamination) [11]. Critical loads of 80–100 N are frequently recorded for PVD coatings on high speed steel. It should be pointed out that the critical load usually increases with substrate hardness and coating thickness, and decreases with higher surface roughness [11].

Some general stages are summarized in Figure 3.8. As the load increases, the angular cracks first appear at the edge of the scratch (a), with further increase of the load parallel (b) and transverse semicircular cracks (c) appear. Coating chipping (d) and spalling (e) occur at the final stage before exposing the bare substrate (f). The force at which the coating failure occurs is recorded as the delamination force. Several measurements have to be done in order to determine the average force of the coating adhesion (f).

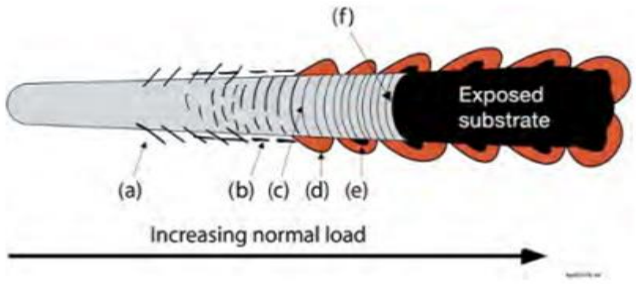


Figure 3.8: Crack generation and coating failure during scratch test [40].

The forces of total delamination of hard coatings used in this thesis are collected in Table 5.1.

3.4.2 Hardness measurements

(Nano)hardness was measured by indentation using Fischerscope H100C. With it the hardness according to Vickers can be measured. The maximum load that can be applied is 1 N, and the lower load limit is 0.4 mN.

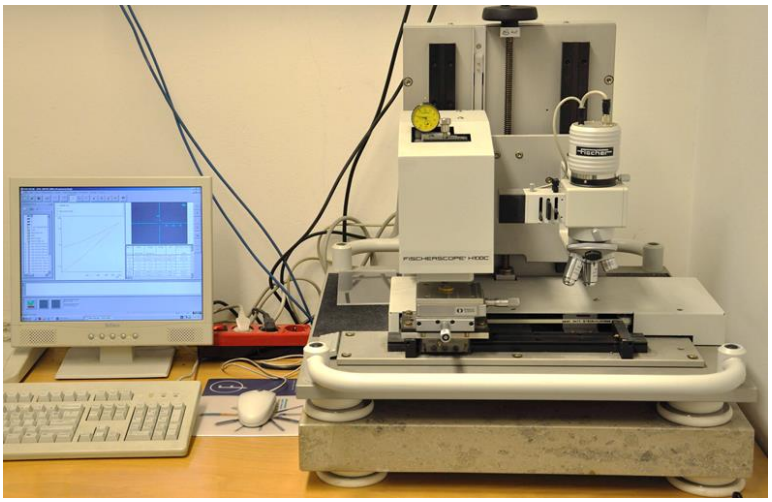


Figure 3.9: The Fischerscope H100C hardness tester.

Hardness is a measure of how resistant solid matter is to various kinds of permanent shape change when a compressive force is applied. It is defined as the ratio between the indenter normal force (F) and the projected area (d is the diagonal of indentation) of the indent at the surface of the measured material.

$$H = \text{const}\frac{F}{d^2} \tag{3.2}$$

The typical principle involves a diamond pyramid which is pressed into the material by a specific force. Hardness is then evaluated from the size of the indentation. Harder materials leave small indentations on the surface. Alternatively, the depth of the indenter can be measured instead. In this method the depth is measured as a function of force (loading and unloading). The hardness is calculated from the depth-force diagram using the Oliver and Pharr procedure [106]. The hardness is measured in different units due to high dependence of hardness on the measuring method. Physically the most correct would be in MPa which is more and more used though still the most common is the Vickers hardness (HV) expressed in kg/mm^2. The approximate relationship between those two is H≈10 HV [40].

Because the hardness is measured by pressing indenter into the sample, care must be taken when measuring thin films. For correct value of the hardness the influence of the substrate must be avoided. According to the standard [40] the indentation depth must not exceed 1/10 of the film thickness. The depth of the indent is monitored during measurement. The influence of surface roughness has to be considered too. For properly measured hardness, statistical approach, by measuring at least three times, must be performed.

3.4.3 Friction and wear characterization

To test friction and wear of the coatings, we used a standard room temperature tribometer CSM Tribometer (now part of Anton Paar). The operating principle of tribometer is shown in Figure 3.10. It uses a 6 mm diameter ball (alumina or 100Cr6 steel) for counterbody. Alumina and 100Cr6 are both softer than the hard coatings, but alumina has a bit smaller hardness than hard coating, while 100Cr6 ball is much softer. The counterbody is held by the ball holder on a lever which is connected to the tangential force sensor and balancing weights. The latter is used to counterbalance the weights of the lever and the ball holder. Normal load is applied by death weights on the ball holder.

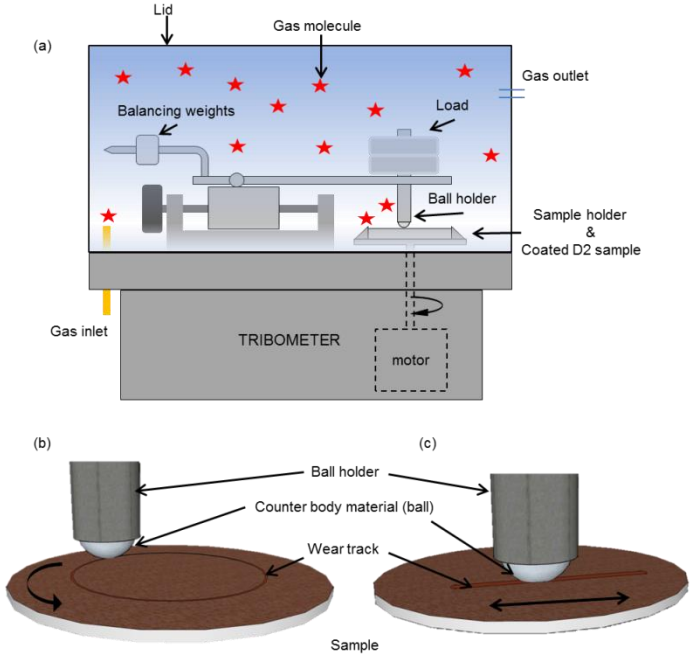


Figure 3.10: Scheme of a standard room temperature tribometer. The tribometer can operate in two modes(b) unidirectional and (c) reciprocal.

The tribometer has a motor connected to the sample holder. It enables two modes of testing: single way or unidirectional mode (b) and two way or reciprocal mode (c). The tribometer is covered with a transparent lid which enables atmosphere changes by applying different gases through gas inlet.

For the study of the **influence of nodular defects on tribological properties** of hard coatings two kinds of tests were performed:

- In reciprocal mode
- In unidirectional mode

All tribological tests were conducted at room temperature. For reciprocal mode tests the wear track length was set to 5 mm. The beginning of the wear track was set one millimeter from the Rockwell test indentation. All the tests were done with 1 N load (Al_2O_3 p_{max}= 810 MPa, 100Cr6 p_{max}=610 MPa) and 1 cm/s sliding velocity. At each test different number of ball sliding cycles (4–256) was conducted. These tests were especially appropriate for the 3D profilometry examinations which were performed perpendicular to the wear tracks. With SEM, the examination of GD in as deposited and after sliding condition was done. In the cyclic mode tests the progression of wear from as deposited to end of the test on the same defect was observed.

To locate the same defects after the tribological test, all samples were marked with Rockwell indentations for local coordinate system determination. The coordinates of these markers were used to translate from the OM stage coordinate system to the SEM or FIB coordinate system. The translation equation between two different coordinate systems can be written as [107]:

$$r'=Mr+r_0 \tag{3.3}$$

In the Equation 3.3 the *r* presents a vector of a point (Rockwell indentation) in the first coordinate system, *r'* the same point vector in the second coordinate system, *M* presents the rotation matrix and r_0 the spacing of the reference point. The above equation can be also written as

$$\begin{pmatrix} x' \\ y' \end{pmatrix} = \begin{pmatrix} \cos\varphi & -\sin\varphi \\ \sin\varphi & \cos\varphi \end{pmatrix} \begin{pmatrix} x \\ y \end{pmatrix} + \begin{pmatrix} x_0 \\ y_0 \end{pmatrix} \tag{3.4}$$

and can be further itemized to

$$\begin{aligned} x' &= \frac{y_2'-y_1'}{d}x + \frac{x_2'-x_1'}{d}y + x_1' \\ y' &= \frac{x_2'-x_1'}{d}x + \frac{y_2'-y_1'}{d}y + y_1' \end{aligned} \tag{3.5}$$

In the latter (Equation 3.5) (x'_1,y'_1) and (x'_2,y'_2) present the coordinates of reference points in second coordinate system, while $(0,0)$ and $(0,d)$ present the coordinates in the first coordinate system. *d* is the distance between both reference points and can be formulated as:

$$d=\sqrt{(x_1'-x_2')^2+(y_1'-y_2')^2} \tag{3.6}$$

The use of such translation system enabled us to find the same growth defects under different microscopes before and after the tribological testing.

For tests in **reciprocal mode** additional Rockwell indentations were done. They mark the approximate tribological test starting position (Figure 3.11). The position coordinates of all Rockwell indentations were taken using an optical microscope (OM) (Zeiss Axio CSM 700). The samples were than examined with SEM (Jeol JSM-7600F). Besides the imaging, the position coordinates of several defects were saved. Using this approach the same growth defect was easily found after the tribological test.

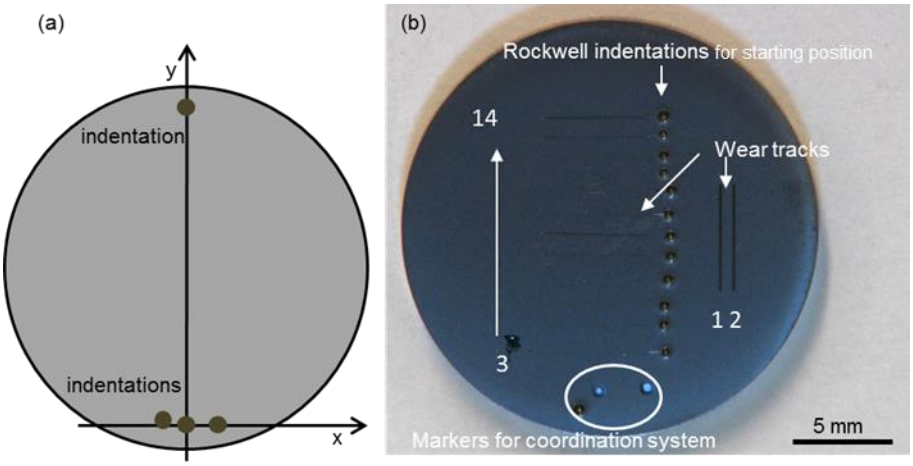


Figure 3.11: Sample preparation for ND identification under SEM. (a)Sample coordinate system orientation[107] and (b) TiAlN sample used for linear tests

For **unidirectional mode** experiments the samples were prepared similar as for the reciprocal test, just without markings at the start position. The starting position of the test was defined as one mm beneath the lowest coordinate system marker. A relatively large area was examined to ensure that some defects were in the wear track.

A unidirectional mode was employed with a wear-track radius of 5 mm for the 100Cr6 and 4 mm for the alumina, both performed on the same sample. In all the tribological tests the parameters were kept constant (1 N load and 3 cm/s velocity of sliding). The tests were designed to track the progression of the contact area in the initial sliding cycles. A set of 1, 4, 8, 16, 32, 64 and 128 cycles was made for each counter-body material. All individual tests started in the same position. After each set of cycles an SEM analysis of nodular defects was performed. The FIB analysis was done only on selected growth defects after a certain number of sliding cycles.

We did not track individual growth defects when testing the **effect of atmosphere** on the tribological properties of hard coatings. In these tests only reciprocal sliding mode was used. For a counterbody a 6 mm Al_2O_3 (HV≈2000) ball was used due to its inertness to high oxidizing atmosphere. All experiments were conducted with the normal load of 5 N (p_{max} = 1.3–1.6 GPa) and the movement velocity of 2 cm/s over a 5 mm long track. The number of cycles was set constant at 5000 for all the hard coatings with an exception of TiAlN which was set to 3000 due to premature wear off.

Prior to the test the samples were cleaned with ethanol in the ultrasonic bath for 10 min, dried, wiped with 2-propanol and purged with nitrogen. Every sample was also purged after each individual test by blowing with the dry nitrogen to remove the loosely attached wear particles which could interfere with incoming tests.

To achieve a change in atmosphere a constant flow of pure gas was blown through the tribometer chamber. Nitrogen or oxygen gas of high purity was let to flow constantly through the tribometer chamber for at least 10 minutes prior the test. For ambient air atmosphere experiments, no gas was used and the tribometer chamber was ventilated for approximately 10 min prior to the test. The humidity was monitored with Voltcraft HT-200 humidity meter which was placed in the vicinity of the test sample. The laboratory conditions were constant (laboratory room temperature and approximately 40% relative humidity (RH)). In the case of the nitrogen or oxygen atmosphere the humidity level was 0% RH. For wear tracks and wear particles analysis the optical and scanning electron microscopy with EDS were used. Wear of the coating was measured by 3D stylus profilometry.

Chapter 4

The Influence of Growth Defects on Tribological Properties of Hard Coatings

4.1 Coating characteristics

Since the aim was to track the changes in growth defect morphology all the tribological tests were done only on the standard TiAlN coating prepared by unbalanced magnetron sputtering. D2 tool steel discs were used as substrates in all tests.
The TiAlN coating composition was Ti 23 at. %, Al 27 at. % and N 50 at. % a face-centered cubic crystal structure as measured by XRD (Figure 5.2). A hardness of 3350 $\pm$ 150 HV was measured by nanoindentation (Fischerscope H100C). The residual stress in the coatings was measured from the curvature of a sample deposited on a silicon wafer. By using the Stoney formula we obtained the compressive stress of 2.5 $\pm$ 0.3 GPa. All the samples had a high density on nodular defects.

4.2 Results

4.2.1 Reciprocal tests using Al_2O_3 counterbody

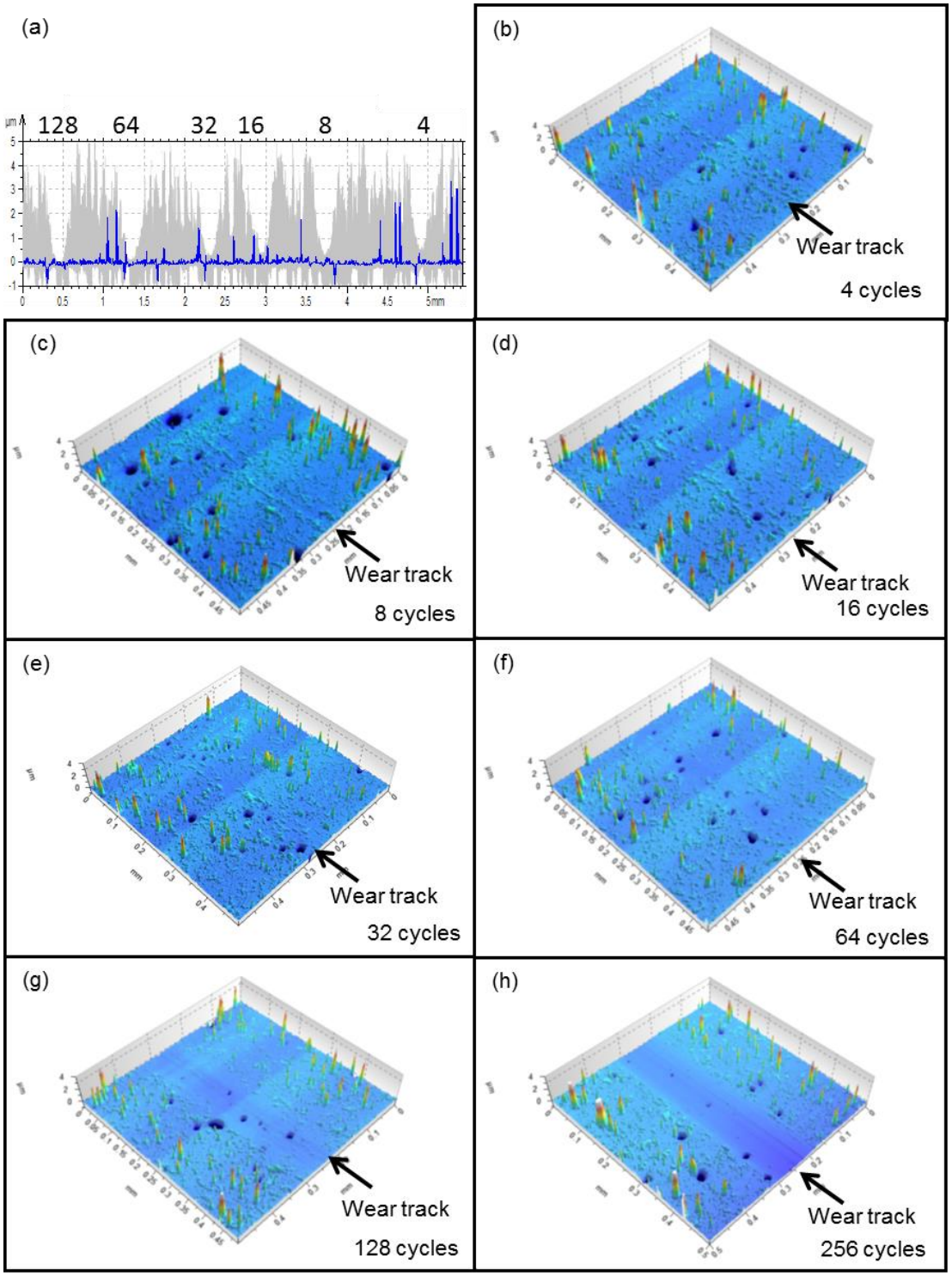


Figure 4.1: Stylus profilometer images of wear tracks on TiAlN: (a) Average line profile across the wear tracks. (b-h) individual 3D profilometry images of the middle of the wear track. The scanning size was 0.5 × 1 mm.

These tests were designed to track the changes by profilometry as shown in Figure 4.1. During the first four cycles only the tops of the nodular defects are removed (Figure

4.1(b)), as the friction coefficient steeply rises from 0.2 to 0.6 (Figure 4.2(a)). After additional cycles the nodular defects appear geometrically smaller until after 64 cycles, when they are completely worn out. The COF measurements in this period are consistent with profile images, meaning that the COF is generally rising to approximately 0.7 together with an increasing contact area due to breaking of nodular defects. Some discrepancy can be noticed in COF behavior presumably due to local differences in GD density and distribution.

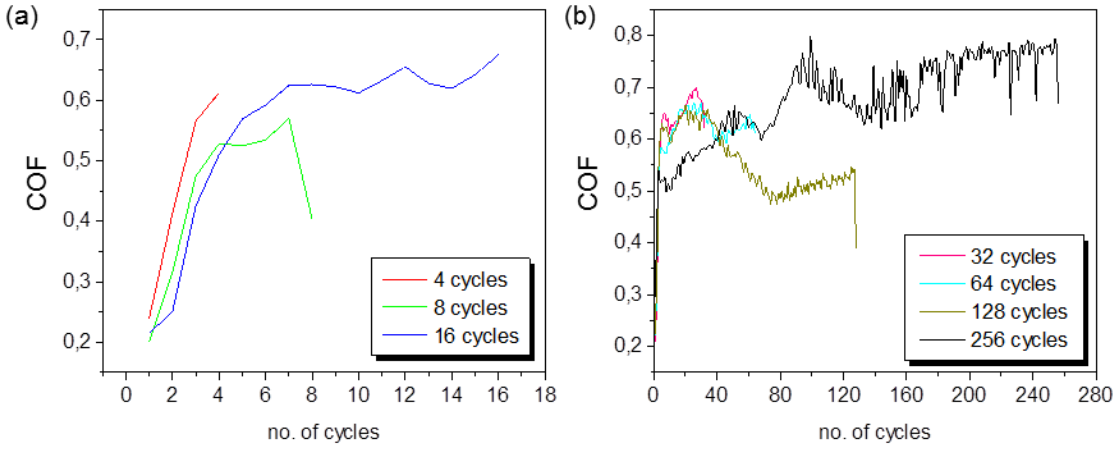


Figure 4.2: Friction coefficient measurements in the reciprocal mode. (a) for 4, 8 and 16 cycles and (b) for 32, 64, 128 and 256 cycles.

After 64 cycles the nodular defects in the wear track disappear but there is no visible damage on the hard coating surface. As the number of cycles increases to 128 or even 256, the grooves in the hard coating surface appear. There is no trace of nodular defects and the wear track appears to be smooth. The COF rises to 0.8 in this period where it stabilizes. SEM analysis of the defects before and after tribological test gives us a more detailed description on the wear progress. In Figure 4.3 a particular defect before and after 4, 16 and 64 cycles is presented. The defects that are presented originate from the middle of the wear track and were all subjected to progressive wear from the beginning of the test.

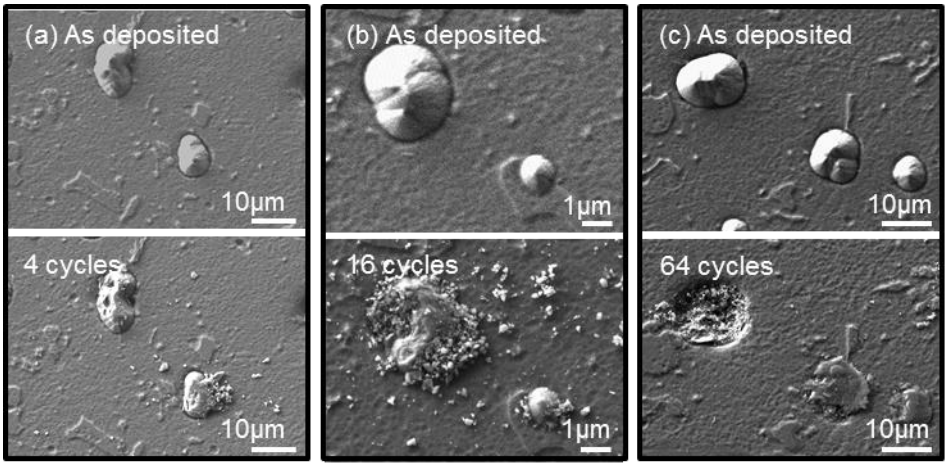


Figure 4.3: SEM images of groups of nodular defects on TiAlN before and after the test. (a) As-deposited and after 4 cycles, (b) as-deposited and after 16 cycles and (c) as-deposited and after 64 cycles.

After four cycles the defect tops are removed. Depending on the position in the wear track and the height of the neighboring defects, some defects suffer more damage than others presented in Figure 4.3 (a). After additional 12 cycles larger nodular defects are crushed,

but the majority of the nodular defects still peaks over the coating surface (Figure 4.3 (b)). This is not the case after 64 cycles, where the majority of the defects are leveled with the hard coating surface. Some, usually larger defects wrench out of the coating and form craters. Presumably this happens due to larger stress as Münz described in his model [76]. Selected defects were analyzed using FIB cross sections. These are presented in Figure 4.4.

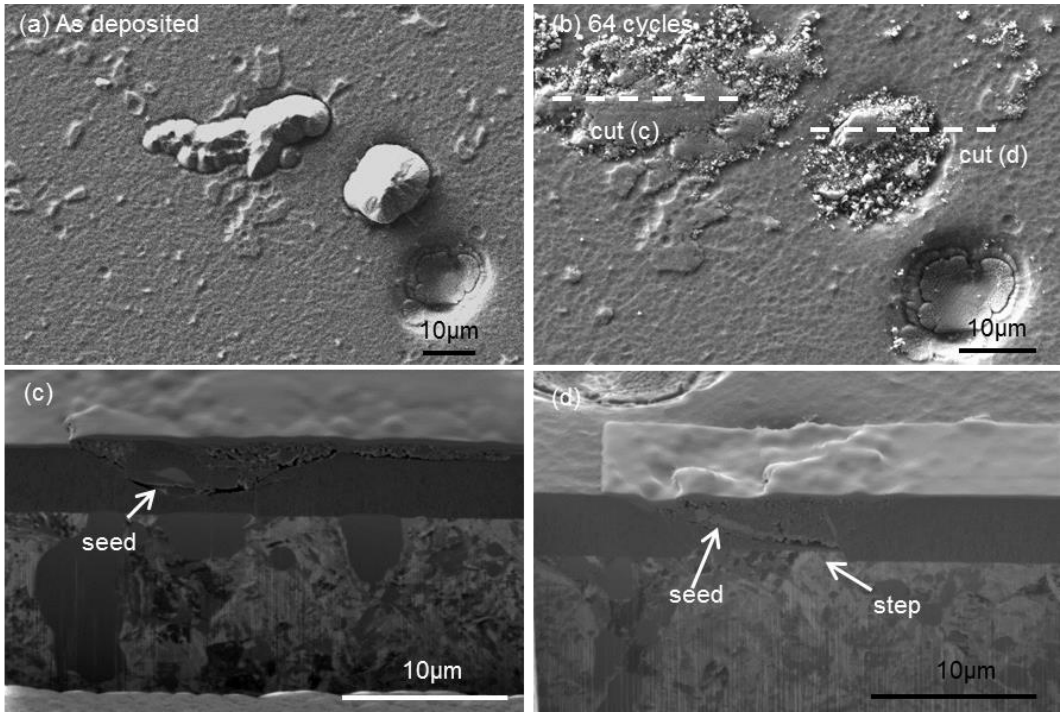


Figure 4.4: SEM images of nodular defects before and after pin-on-disc. (a) As-deposited defects and (b) the same defects after 64 cycles sliding with alumina ball. The lines indicate the FIB cross section cuts, which are presented in (c) and (d).

As indicated in Figure 4.4 (b), after 64 cycles there is no major damage on the coating surface. The presented nodular defects experienced two distinct mechanisms of wear, namely the first mechanism is the powdering of the defect leaving the debris on the spot. The second mechanism was leveling the defect with the surface by breaking to smaller pieces that were then removed from the wear track. The defect presented in (c) was elongated and its seed landed on the hard coating during material deposition, while the defect presented in (d) was a typical cone like defect whose iron seed landed on the substrate during the etching process. This is indicated by the step beneath the seed. In both cases the remaining defect is composed of defect particles reaching all the way to the seed. A more detailed look in the defect (d) reveals that the seed was also damaged and crushed in smaller particles by the sliding load.

4.2.2 Reciprocal test using 100Cr6 counterbody

Figure 4.5a presents profiles made across the wear tracks after the tribological test using 100Cr6 ball, and 3D profiles of the wear track after a series of cycles. After one cycle the COF almost instantly reaches 0.6 (Figure 4.6a). In this cycle the tops of the highest nodular defects are broken. In Figure 4.5 the defects in the wear track appear to be more elongated in the direction of sliding. This indicates the galling or sticking of some material on the defects. SEM images in Figure 4.7 (a) show the material being collected by the nodular defects as confirmed by EDS analysis on (c). The wear track becomes more visible after additional sliding. The defects appear thicker compared to the defects outside the wear track due to galling of the counterbody material. After 32 cycles the wear track is about 200 µm in width. Beside the material being collected by nodular defects, the material from 100Cr6 ball also adheres on the hard coating surface.

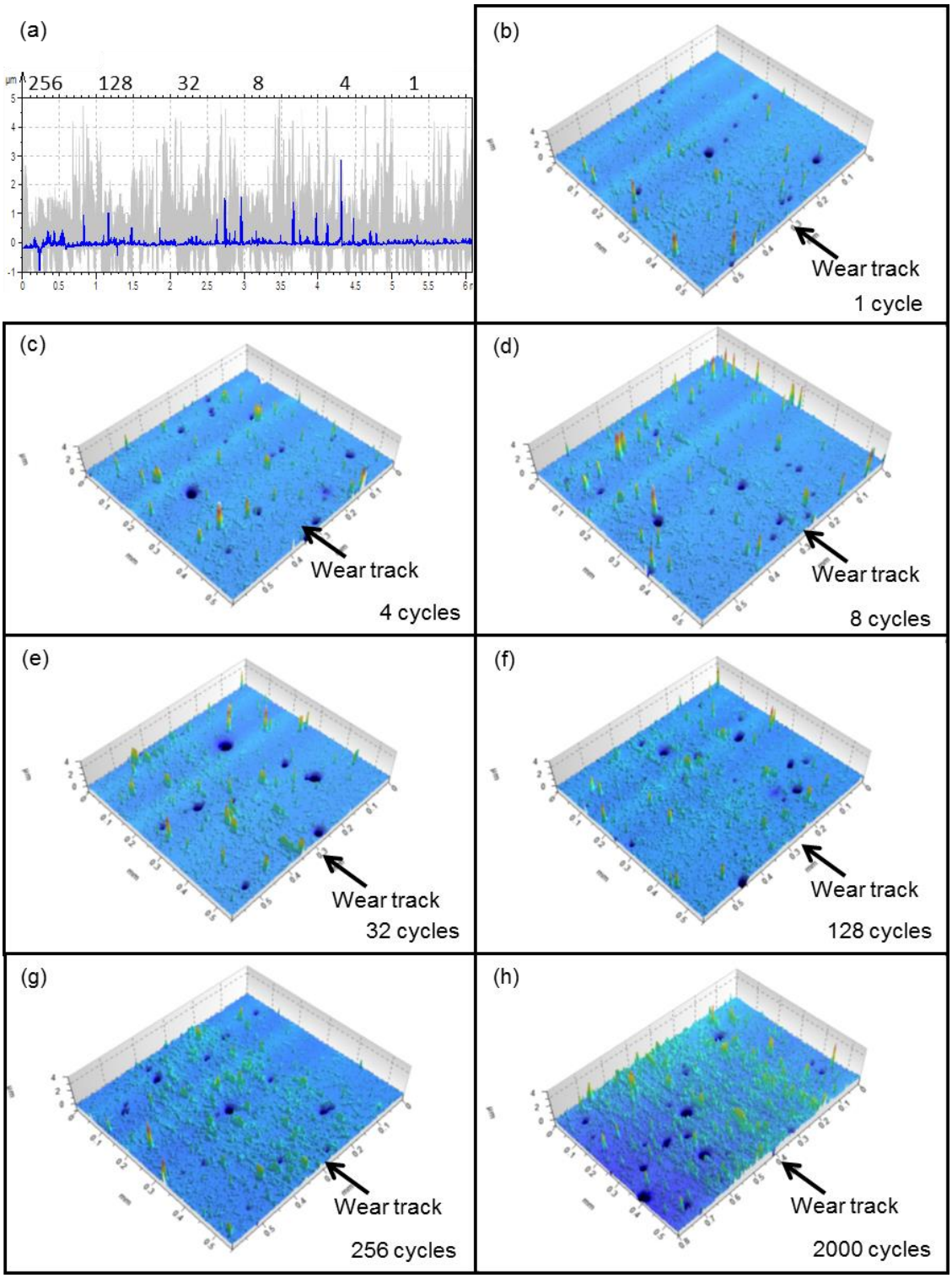


Figure 4.5: Stylus profilometer images: (a) Average line profile across the wear tracks. (b-h) individual 3D profilometry images of the middle of the wear track. The scanning size was 0.5 × 1 mm.

Figure 4.6 (a) presents the COF behavior up to 32 cycles. It rises from 0.1 to a stable value of 0.7. The COF measurements in this period show good repeatability between them. The exception is the 2000 cycle's measurement which show different slope. From 3D profilometry measurements the progression in wear of the defects is not apparent. As the tests continue the wear track widens to about 250 μm in 256 cycles. More and more defects are covered by the ball material.

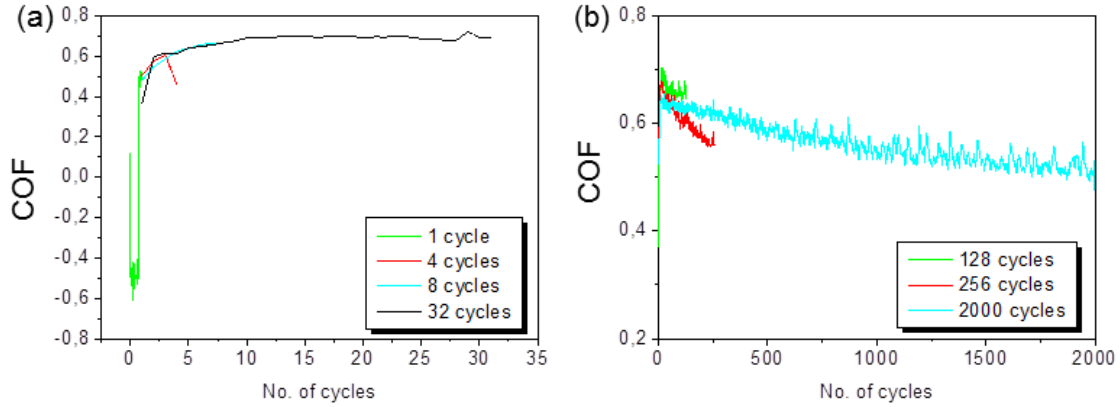


Figure 4.6: COF measurements with 100Cr6 as counterbody. (a) 1, 4, 8 and 32 cycles and (b) for 128, 256 and 2000 cycles.

An additional test up to 2000 cycles was made to find out if some damage on the coating could be detectable after longer sliding time. From profilometry images, we can conclude that the hard coating did not wear off. The wear track width on the hard coating reached 0.5 mm at the end of the longest test. COF measurements (Figure 4.6 (b)) do not match as well as in shorter tests. The measurements for 128 and 256 cycles have a similar trend but the longer test shows different value of COF. This could be related to different local surface topography and even more because of the influence of environment over longer testing time.

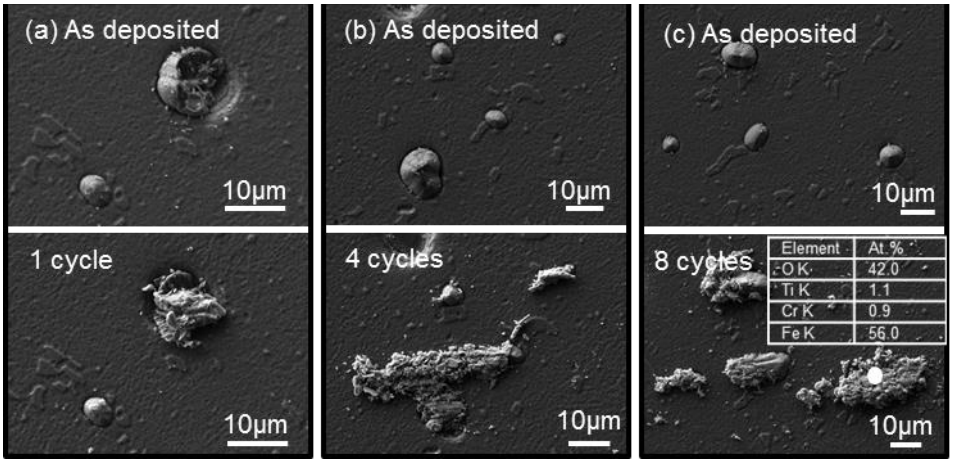


Figure 4.7: SEM images of different groups of ND before and after test. (a) As-deposited and after 1 cycle, (b) as-deposited and after 4 cycles and (c) as-deposited and after 8 cycles.

SEM analyses of the defects before and after the tribological tests reveal similar results as the 3D-profilometry. The nodular defects are the first contact between the sliding surfaces. Because the defects exhibit higher hardness than the counterbody, they suffer less damage. From Figure 4.7 we can track the progression of material being collected. As the number of cycles increases, the amount of counterbody material surrounding the nodular defects grows and appears denser. In some cases, larger nodular defects are broken and leveled with the surface.

In SEM Figure 4.8 (a) and (b) a surface comparison between the as-deposited and after 128 cycles is presented. Nodular defects are covered by the counterbody material forming tribological film patches. Grooves on the patch indicate that the structure is dense. A more detailed observation reveals that as the counterbody reaches the surface of the nodular defects, the ball material is collected by the surface irregularities. Since the density of these irregularities is relatively large, a large part of the surface is covered by the ball material.

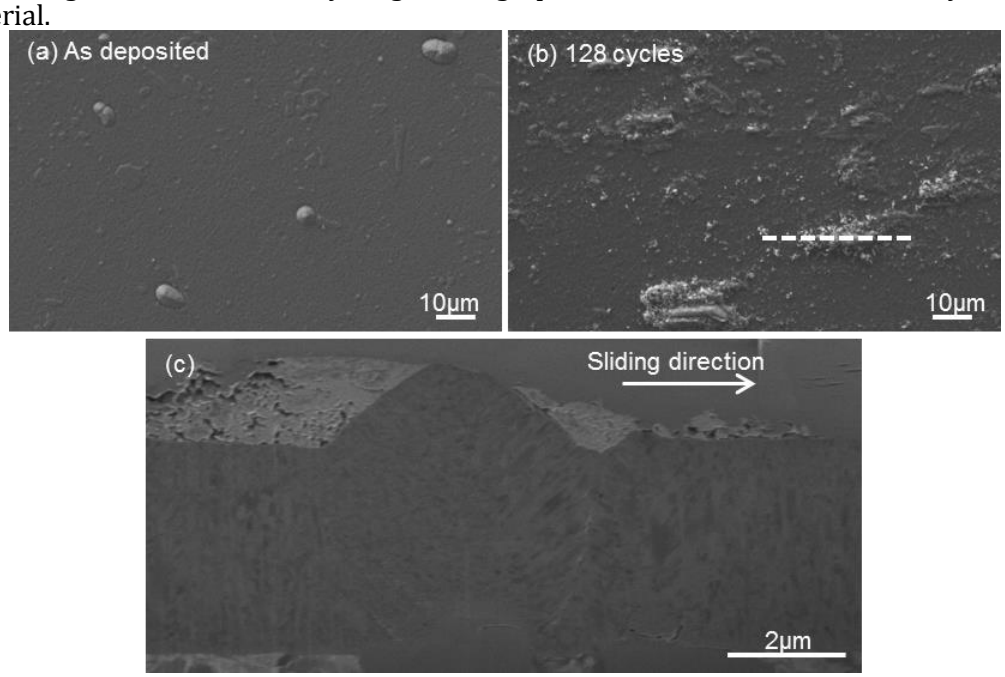


Figure 4.8: SEM images of nodular defects. (a) As-deposited, and (b) defects after 128 cycles sliding with 100Cr6 ball. The line indicates the FIB cross section cut presented in (c).

The nodular defect in Figure 4.8 positioned in the middle of the wear track was cut using FIB. From the image (c) we notice that the tribological film forms on both sides of the nodular defect due to a nature of reciprocal sliding. The thickness of this tribofilm close to the defect is up to two micrometers. The tribo film thickness is larger on a site of final sliding direction and compressed into the depression around the defect. EDS analysis showed that it is composed mainly from the counterbody material mixed with defect particles in smaller concentration.

4.2.3 Unidirectional tests with the Al_2O_3 ball counterbody

Using alumina ball as a counterbody (alumina has a more comparable hardness to that of TiAlN coating) the wear is also expected on the hard coating surface. In Figure 4.9 the same surface area of the as-deposited TiAlN coating sample and after 128 cycles sliding with alumina is presented.

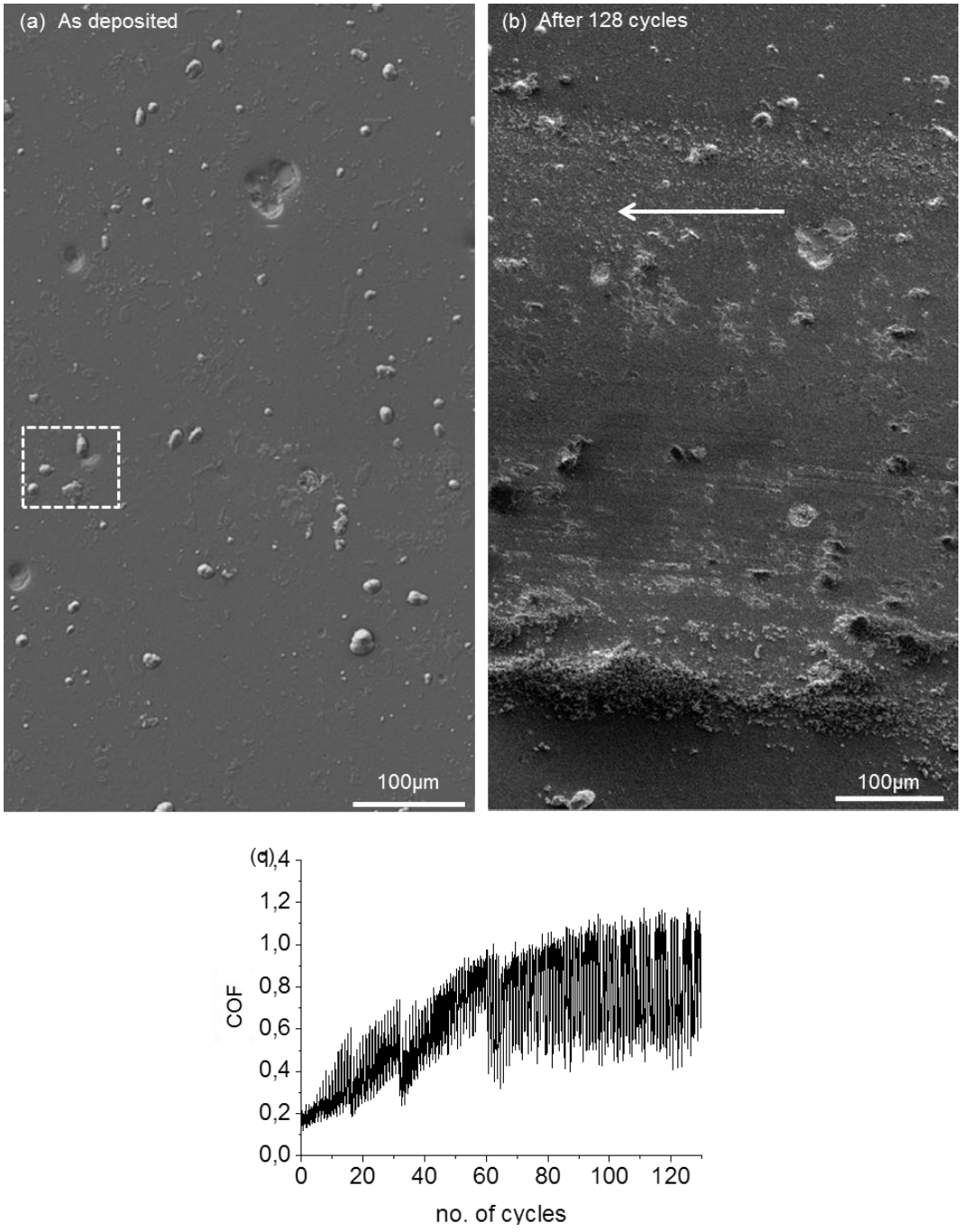


Figure 4.9: The coating surface (a) before and (b) after 128 cycles using the Al_2O_3 ball; (c) the coefficient of friction (COF) versus the number of cycles.

The arrow indicates the direction of sliding. The set of growth defects labeled with a square was studied in more detail by following the progression of their wear (Figure 4.10). Comparing the images in Figure 4.9 (a) and (b) we can see that all the asperities appear to be leveled with the coating surface in the wear track. At some positions (around ND) the material is also adhered to the surface. This leveling rate is slower when using

Al_2O_3 than the micro-cutting of the softer 100Cr6 material. Hence, a large difference is evident as we compare the COF measurements on the TiAlN coating obtained with a softer counterbody and that with the harder one (alumina).

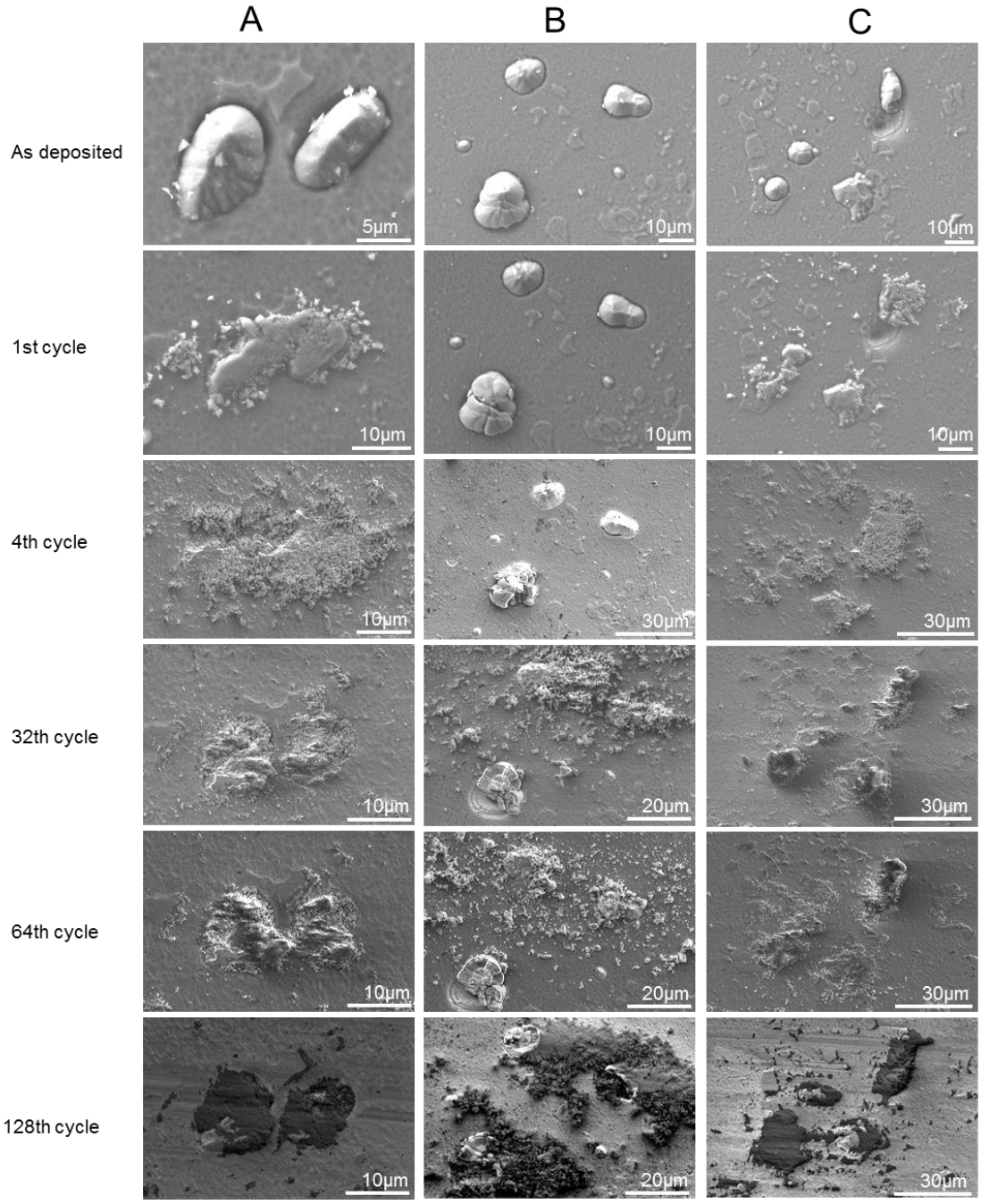


Figure 4.10: SEM images of the same group of growth defects before and after the pin-on-disc test ranging from cycle 1 to cycle 128.

In Figure 4.9(c) the COF measurements for all the 128 cycles are collected. COF value starts close to 0.2 and steadily reaches 1 in about 100 cycles. Slow increase of COF can be explained by the progression of the breaking and the spallation of the nodular defects (Figure 4.10) and the collection of wear debris. The wear of the alumina ball is presented in Figure 4.11. On the latter set of images the adhered material on the ball can also be noticed.

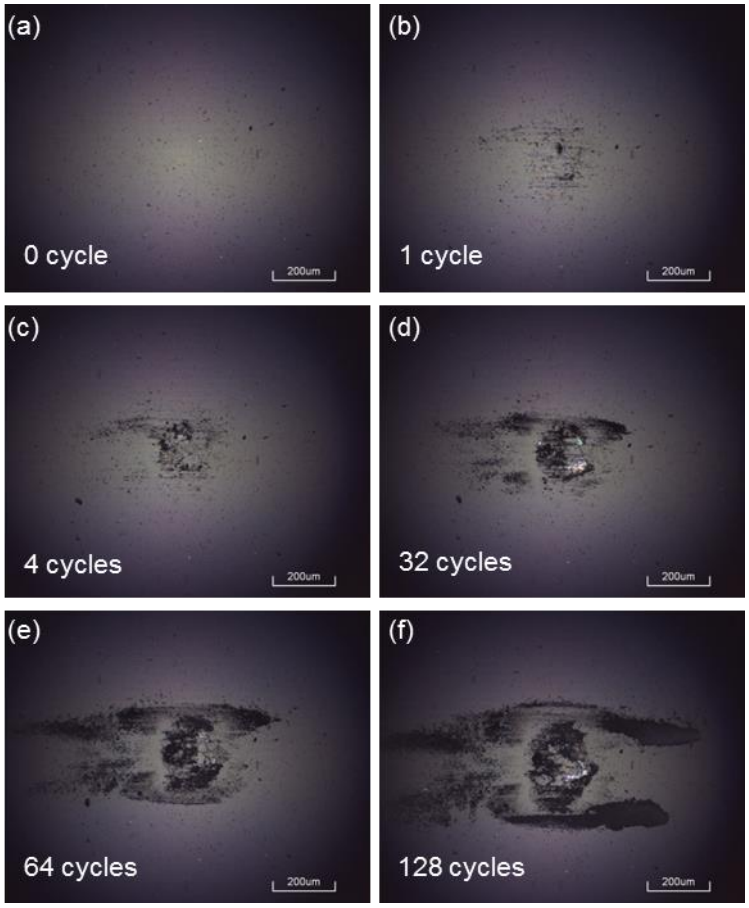


Figure 4.11: Optical micrographs of wear scar formed on the alumina balls.In (a) the image of an unused ball is presented. The wear of the ball progresses (b-f) with the number of cycles.

By breaking of nodular defects a large amount of particles is introduced in the sliding contact. The entrapped particles in the contact are subjected to a sliding/rolling motion under the applied compressive and tangential loads. As a result of these forces, a fine fragmentation of defects occurs, this causes at a later stage the abrasive wear of counterface and coating surface. Particles that are pushed from the contact region accumulate at the edge of the wear track. The wear particles, in contact region or at the edge of the wear track, are poorly adhered and can be easily removed. In Figure 4.9(c), drops or steps in COF after each individual test are observed. COF mismatch could be caused by the wear particle removal during SEM and FIB analysis.

The analysis of typical nodular defects in the middle of the wear track shows the formation of fine abrasive particles and oxidation at their positions (Figure 4.10). The oxide products appear darker on BSE image at 128 cycles. After just four cycles these fine abrasive particles filled up the depressions (craters) in the contact zone.

The residual debris was pushed outwards, resulting in a cleaner and smoother center of the wear track. This is noticed after just 32 cycles, while the debris which is not in the center of the wear track, stayed stationary. Some debris is also anchored around the nodular defects. Until the nodular defect was completely worn off, this debris was compressed in front of the defect. As the steady-state approaches (after approximately 128 cycles) the grooves are visible on the defect-free coating surface. The formation of such grooves is caused by the TiAlN and alumina abrasive particles and also by the asperities on the counter body. The asperities were noticed after we cleaned the surface of the ball by ultrasound bath in ethanol and dried with nitrogen (Figure 4.12(a)).

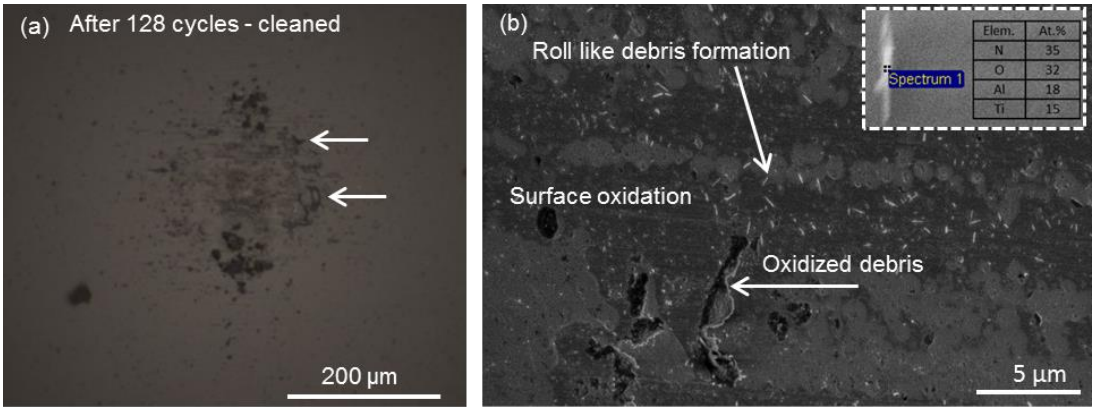


Figure 4.12: Optical micrograph and SEM image of counterbody and wear track (a) OM image of cleaned alumina ball after 128 cycles. The asperities of adhered material are marked with arrows. (b) SEM image of the oxidized coating surface with debris in the form of compressed oxide powder and roll-like debris. EDS analysis of roll-like debris is also presented.

The dark regions on the backscattered-electron (BSE) image correspond to an adherent thin oxide layer or oxidized debris in depressions of the coating (Figure 4.12(b)). We found that such oxide patches occurred preferentially at the sites of the nodular defects, surface irregularities and in the vicinity of the grooves which were noticed after the final test. The final contact area is formed when nodular defects are leveled with the hard coating surface. At this stage we observed the formation of nanoscale, roll-like fragments. These are typical for a TiAlN/Al_2O_3 sliding pair [108-110]. The mechanism of the roll-like debris formation is not understood in detail [110], but this cycle-to-cycle research approach indicates that it might form from the coating surface material due to plowing of the counterbody surface irregularities (Figure 4.12). Observing the counterbody we see that the wear is minimal and not uniform.

From Figure 4.12 (a) we can see an oval wear scar with some adherent material on the periphery of the wear scar marked with arrows. The adherent material on the ball increases the contact with the coating surface, causing damage and tribo-oxidation of the surface and the formation of the first roll-like debris. The origin of the roll-like debris is not known, but they appear to be a product of abrasive wear of the hard coating surface. In order to understand what is happening with the nodular defects we performed several FIB cross sections similar as in the case of the 100Cr6 ball (Figure 4.8).

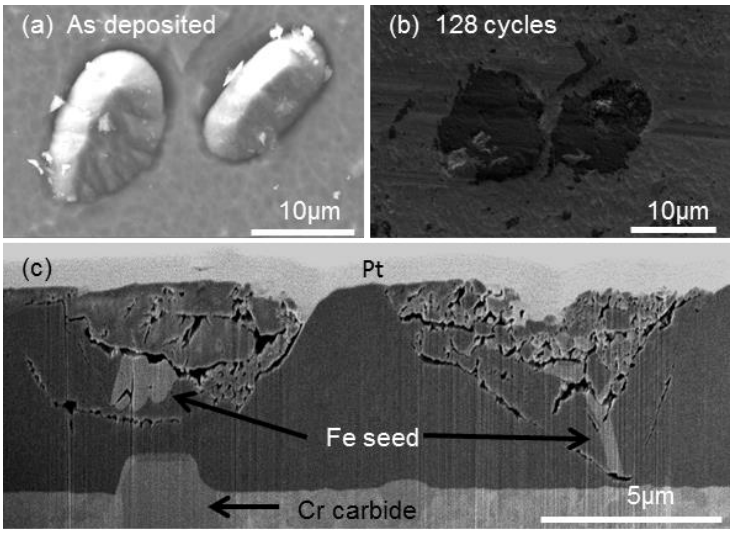


Figure 4.13: SEM images of nodular defect in the center of the wear track. (a) As-deposited defects and (b) after 128 cycles sliding with Al_2O_3 ball. (c) Cross section across the middle of the nodular defects.

In Figure 4.13 two nodular defects from the middle of the wear track were studied. We notice that after 128 cycles the nodular defects were leveled with the coating surface. The depressions at the defect sides were filled with wear products. As the nodular defects were cut we analyzed the seeds. Both consist of iron. We notice in (c) that the left defect grew on chromium carbide. During the ion etching step the iron particle shielded the substrate surface underneath which resulted in a large step. After tribological tests were performed, a large portion of the defect crumbled in small particles. The defect on the right side was also formed on an iron particle. This particle landed on the surface after the ion etching, thus no step is visible beneath the seed. Even though the seeds are geometrically different, they both underwent the same process of powdering. EDS measurements showed that particles consist of partly oxidized hard coating material. In the measurements we could not detect any pure alumina particles from the counterbody.
In Figure 4.14 two neighboring defects were cut at different stages of tribological tests. Figure 4.14 (a) shows the FIB cut through a nodular defect after 64 cycles, while the neighboring defect (c) was cut after additional 64 cycles (all together 128 cycles). In both cases the seeds are iron-based particles (3) which landed on the surface prior or during the etching process. The most noticeable differences are the seed size and the fact that after 128 cycles the defect is crushed in small particles (4) while on defect (a) after 64 cycles only the defect top was removed, leaving the interior of the defect intact. We performed EDS mapping which is presented in (b). The result shows that a fraction of particles is composed of aluminum oxide. The origin cannot be confirmed, but due to the absence of titanium in the oxide layer it is presumably from the counter body.

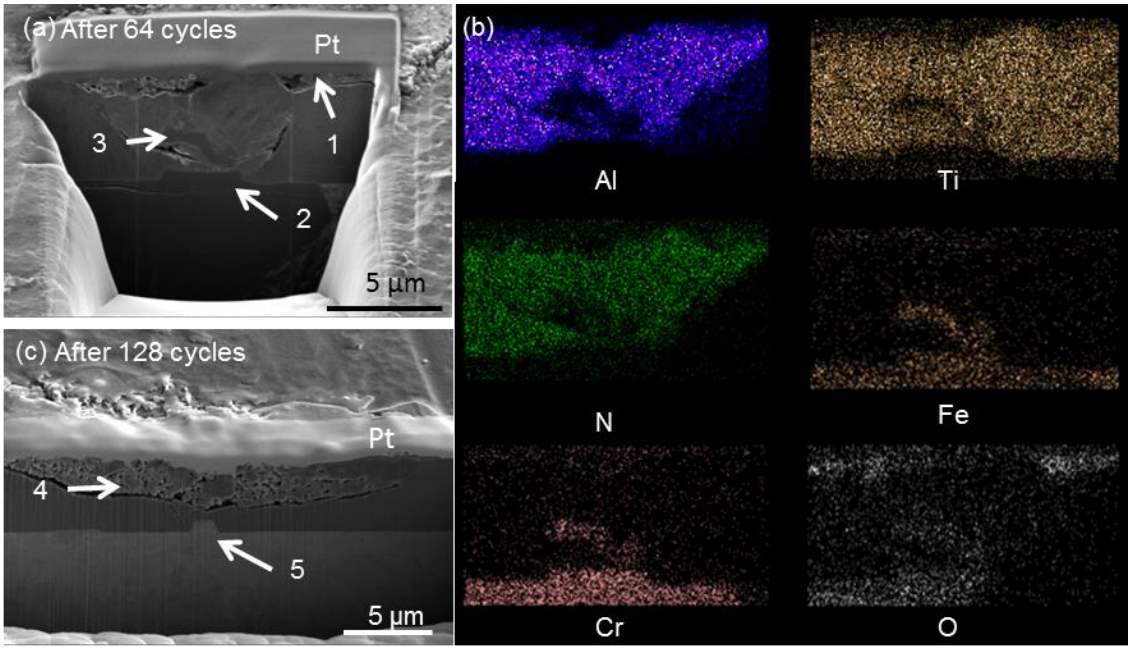


Figure 4.14: FIB and EDS analysis of nodular defects after 64 and 128 cycles sliding. (a) Cross section of a defect after 64 cycles and (b) EDS mapping analysis of the same defect. The neighboring defect (c) was cut after 128 cycles.

Studies of the role of the growth defects in tribological contact show how the defects influence the tribological properties of the hard coatings. With continuous sliding, after the running-in period, the surface is leveled and new tribo-oxidation based wear processes over the whole wear track surface begin. The study of atmosphere influence, such as high and without oxygen presence at the tribological contact, is presented in the chapter 5.

4.2.4 Unidirectional tests with the 100Cr6 ball counterbody

Similar to the linear tests when using a softer counter body the wear of the coating after 128 sliding cycles is minimal. Figure 4.15 shows a large area of the coating surface before and after 128 sliding cycles. The arrow indicates the direction of sliding. The sets of growth defects labeled with a circle in Figure 4.15 were studied in more detail (see Figure 4.16).

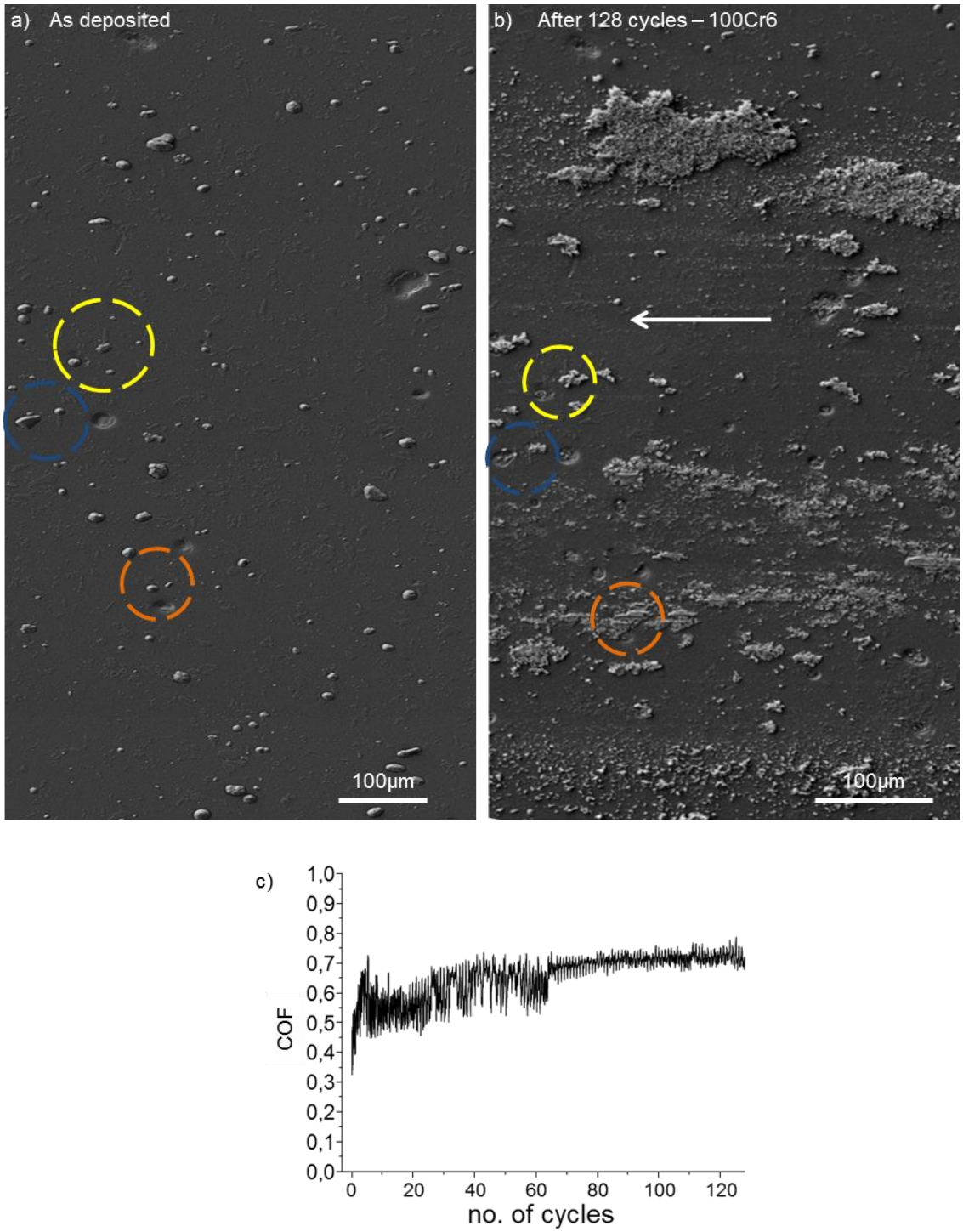


Figure 4.15: The coating surface (a) before and (b) after 128 cycles using the 100Cr6 ball. (c) The coefficient of friction versus the number of cycles.

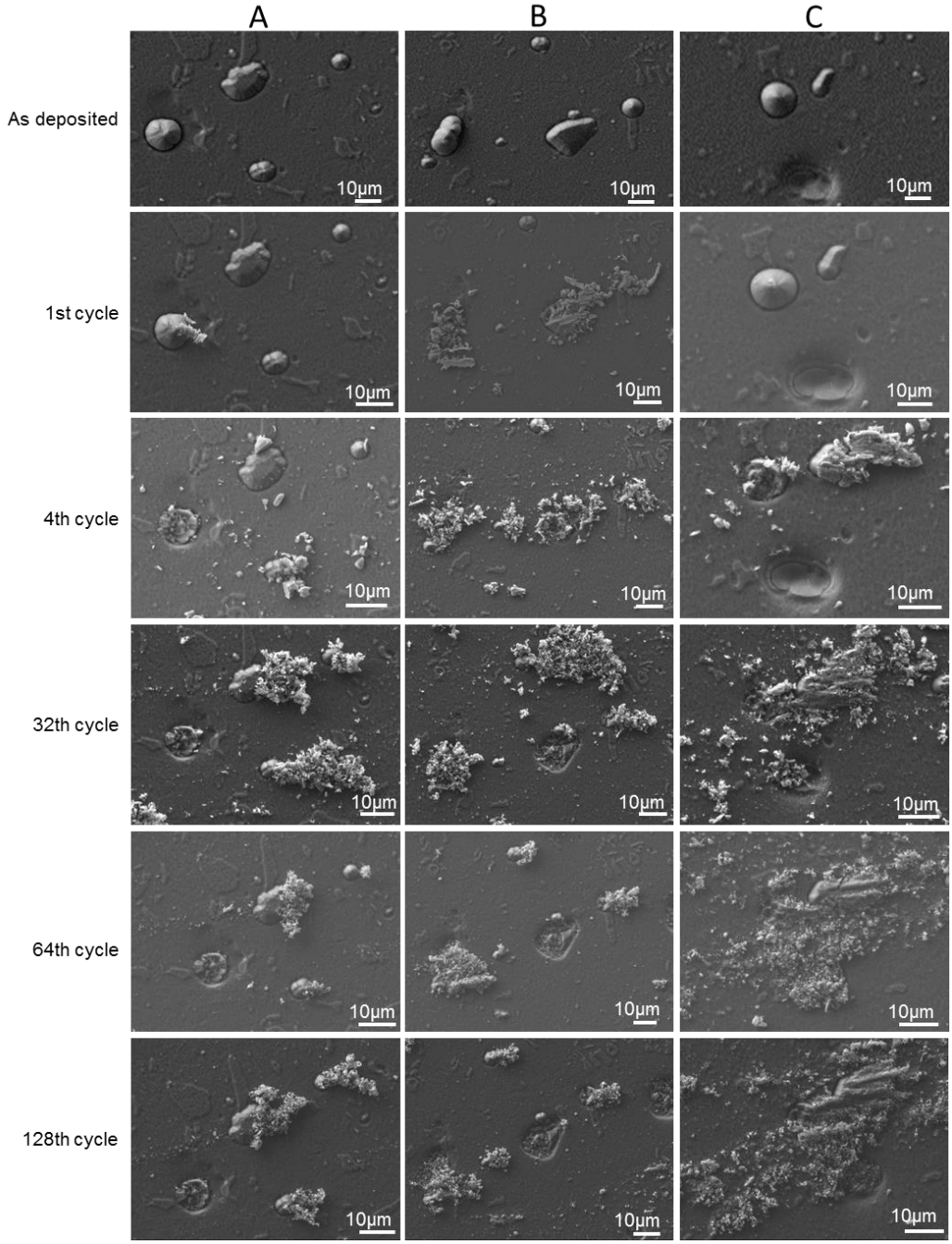


Figure 4.16: SEM images of the same group of growth defects before and after the pin-on-disc tests ranging from the 1st to the 128th cycle.

Comparing the images from Figure 4.15 (a) and (b) we noticed that the damage is visible only on the nodular defects, where craters were formed from the nodules. Similar observations were found in linear tests. As shown in Figure 4.16 this process consists of breaking the nodular defect into small particles. These particles are then removed and craters filled with debris from the counter body. In some cases, usually larger and poorly adhered nodular defects are more susceptible, the nodular defect can be wrenched out in one piece. This is presented in Figure 4.17.

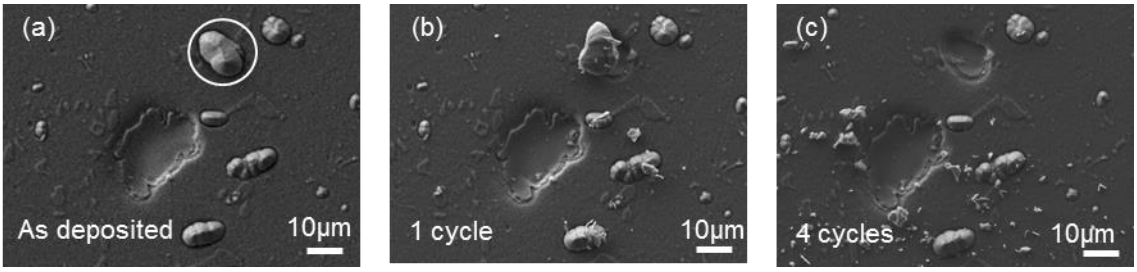


Figure 4.17: SEM images of ND removal. (a) As-deposited and (b, c) after 1 and 4 cycles sliding, showing the removal of the nodular defect in one piece.

Debris composed of defect particles and 100Cr6 ball material fills the craters producing a relatively smooth surface. The remaining debris is either removed from the wear track to the edge or is collected at the sides of the nodular defects. The latter causes the formation of tribological film patches i.e. galling of the counterbody material.

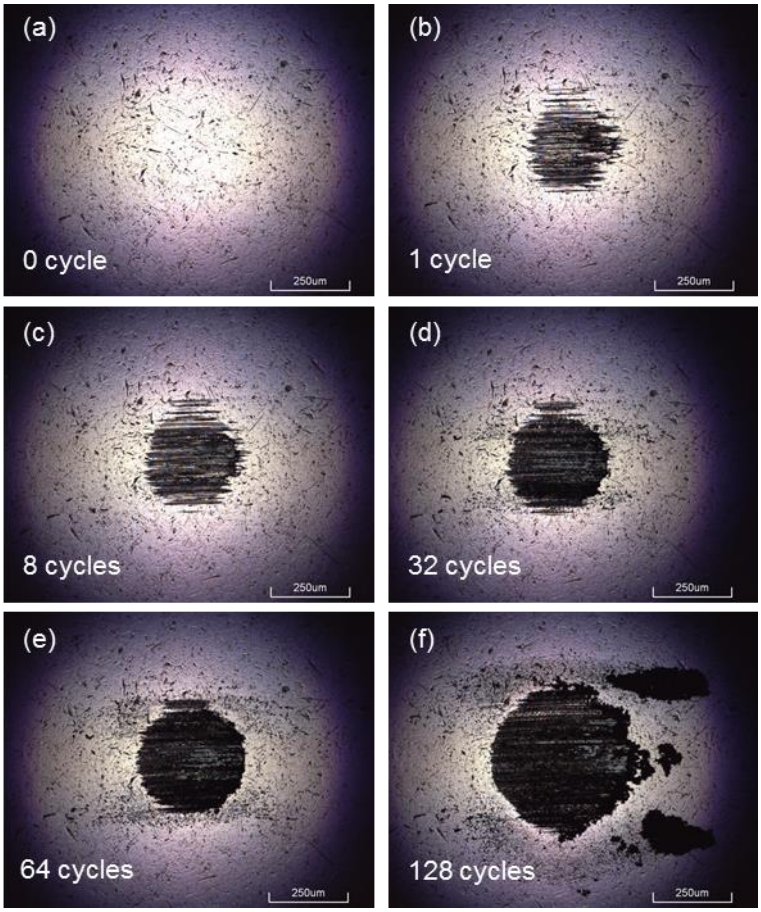


Figure 4.18: Optical micrograph images of wear scar formed on the 100Cr6 ball. In (a) the image of an unused ball is presented. After one cycle (b) the wear in the form of horizontal scratches is clearly visible. The wear of the ball progresses (c-f) with the number of cycles.

The breaking of the nodular defects and the formation of the tribological film have an influence on the COF measurements. In the beginning the coefficient of friction is around 0.35, then it rises to approximately 0.7 during the first 10 cycles (Figure 4.15 c). From the SEM analysis we can conclude that this initial value is related to the small contact area that is formed only by the nodular defects. The contact area can also be roughly estimated by measuring the circumference of the wear scar of the counterbody. The wear scar on the ball is visible after just one cycle, and its diameter increases with each cycle (Figure 4.18 a-f). After a series of 128 cycles the wear-scar radius increases from an initial 120 µm after

one cycle to approximately 240 μm at the end of the test. Due to the wear of the ball, the contact area increases and with every additional cycle more defects are found in the wear track. We found that the initial wear mechanism is cutting of the softer counterbody by nodular defects and the fracturing of the top of the nodular defects. We observed that already after the first cycle some nodular defects have a ball material on their top. These chips are formed due to the cutting effect (micro abrasion) of nodular defects (Figure 4.16). This is also supported with wear scars visible at the counterbody surface. The Figure 4.18 (b) presents the counterbody after the first cycle. On the scar surface the horizontal scratches are already visible; they were caused by nodular defect abrasion of the softer material. These scratches later form a uniform circular wear area, due to a relatively large number of defects in contact over the whole wear track and multiple passes.

As the COF approaches the steady state value we can observe the formation of tribological film patches around clusters of nodular defects. These act as anchoring or collection sites for wear debris. Their position in the wear track and geometry has an influence on the formation of tribofilm and relative size of the patches. Our observations show that elongated defects or groups of smaller defects oriented perpendicular to the sliding direction collect debris more quickly and efficiently (Figure 4.16(c)). With built up material that surrounds the defects, the contact pressure decreases due to the larger surface. The debris accumulates in front of the nodular defects, if viewed from the sliding direction. Immediately after the formation (in the initial cycles) the debris are poorly adhered and can be easily removed with a simple blast of air. After the debris generate from the nodular defects in the later cycles, these fragments mix with the counterbody matrix material that accumulates in larger more compressed patches. This can be clearly seen at designated nodular defects in Figure 4.16 that show a sequence of the same growth defects before and after the tests ranging from 1 cycle to 128 cycles. A clear and progressive wear of the nodular defect and the formation of a large amount of particles can be observed especially on defects (C) where aggregation of particles results in a dense tribological film patch. On the compressed debris patches we observed grooves, which can be chronologically linked with more stable COF values. The counterbody ball slides on the coating surface, contacting only the film patches and defects, in this way creating grooves. It is important to point out that the shape and the position of the film patches are not stable during the wear test. The removals of patches during the tribological test probably cause the fluctuations in the COF measurement.

It must also be emphasized that even though the nodular defects were in the wear track, all of them were not subjected to a full contact load due to the different height of the defects, especially during the first cycles. Only the highest nodular defects were in contact with the ball, scratching its surface. During sliding, the nodular defects in the contact are exposed to high shear stresses, which cause their fracture and spalling. This wear process continued until the nodular defects were leveled with the surface or a protective tribological film was built around them.

At several stages, we preformed FIB and EDS analyses of some surface features. Figure 4.19 (a) presents a chip formed by a nodular defect during the first cycle and FIB cut through (Figure 4.19(b)), respectively, while Figure 4.19 (c and d) presents a ball's wear damage after one cycle of sliding. In Figure 4.19 (a) the ball material in the form of a chip around the nodular defect shows the starting mechanism, which can be labeled as a cutting mechanism, during the first contact with the softer counterpart. The grooves on the edge of the ball wear zone (Figure 4.19c, indicated by arrows) could be caused by individual nodular defects, while the ball wear in the middle of the contact zone was caused by the scratching of a large number of nodular defects across the whole cycle length. The SEM analysis revealed that several nodular defects in the wear track were already broken during the first cycle. The small pieces of these broken defects can be found in the wear track or can be noticed in the middle of the counter body wear scar. An EDS analysis of this region showed that the defects did not suffer any oxidation before they were broken (Figure 4.19 (d)). On the defect-free TiAlN coating surface we did not observe any scratches that could be caused by abrasive particles from the crushed nodular defects.

An example of a broken defect after one cycle is shown in the FIB cross section in Figure 4.19 (b). The nodular defect was almost leveled with the coating surface. The ball material cut off by some other nodular defect was pushed into the depression in front of

the defect (marked with A). This cross section reveals a large number of cracks in the defect and also the seed that caused the growth of the defect (B).

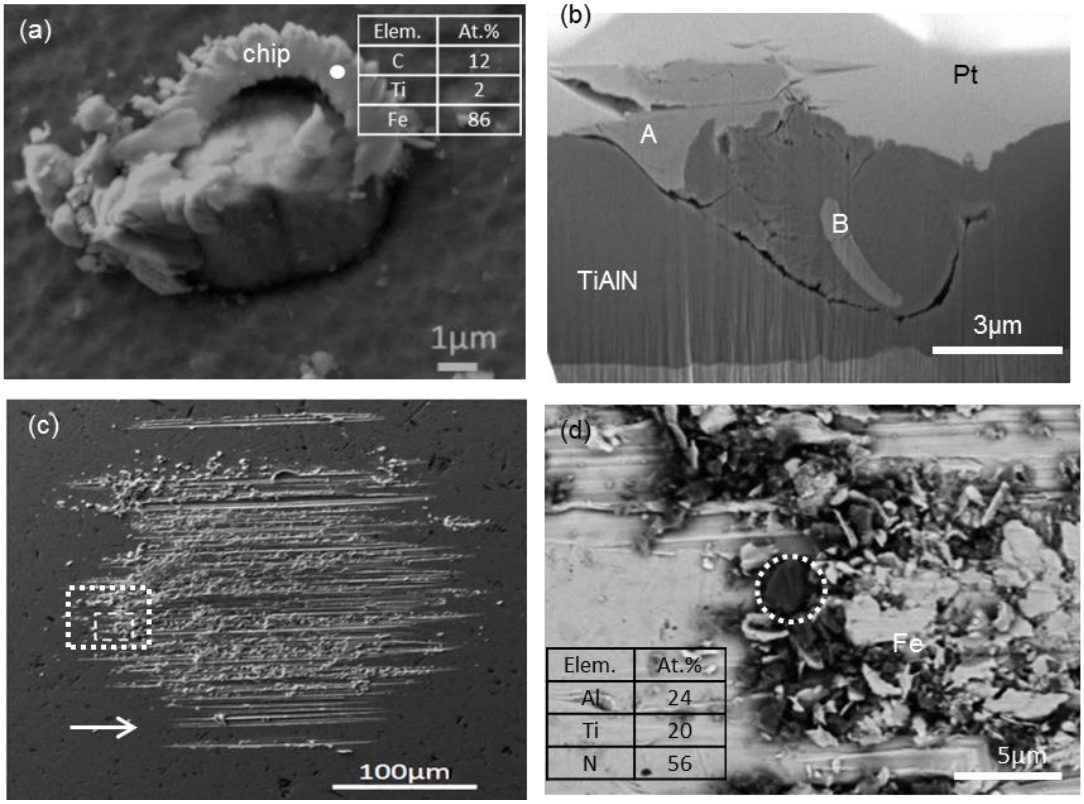


Figure 4.19: SEM images of nodular defect and counterbody surface (a) after one cycle and (b) a FIB cut through of the same defect. In (c) the ball wear scar with horizontal scratches caused by nodular defect is clearly visible, marked area with EDS is presented in (d).

At the end of the 128 cycles the defects from Figure 4.16 (c) were examined by FIB (Figure 4.20). Although the two nodular defects were located close to each other, the defect 1 broke after 4 cycles (Figure 4.20(d)) while the defect 2 (Figure 4.20 (c)) did not break after all the tests.

The first FIB cut was made at the defect 2. This defect is elongated and oriented perpendicular to the sliding direction. Hence a large tribological film formed in front of the nodular defect. It is composed of the counterbody material and the TiAlN wear particles that originate from the crushed nodular defects. These wear particles are visible in the tribological film as the darker spots. The formation of such film protects the defect from high pressure enabling more cycles before it collapses. On this image the formation of a crack across the defect is seen. Its formation could be caused by the high shear stresses generated during the tribological test. Such a crack causes the complete breaking or leveling of the nodular defect with the hard coating surface. In both cases the release of the accumulated debris in the contact may cause the fluctuations in COF. The formation of the nodular defect was caused by an elongated iron particle. For comparison, Figure 4.20 (d) shows the nodular defect 1 that was broken into small pieces after just 4 cycles. The FIB cross-sections were made after 128 cycles. Beneath the deposited protection layer of platinum there is a thin film of counterbody material that filled the depression formed at the sites of the broken nodular defect. Deeper, towards the substrate, there is the iron seed. The seed is large and has an irregular shape making it completely different compared with the defect 2 seed. Underneath the seed a relatively large step in the substrate surface can be noticed. Such step formed during the ion etching of the substrates prior to the deposition of the coating. Namely, if a particle was present on the surface prior to the ion etching, it would have shaded the ion etching and consequently resulted in an “etching step” as visible in Figure 4.20 (d).

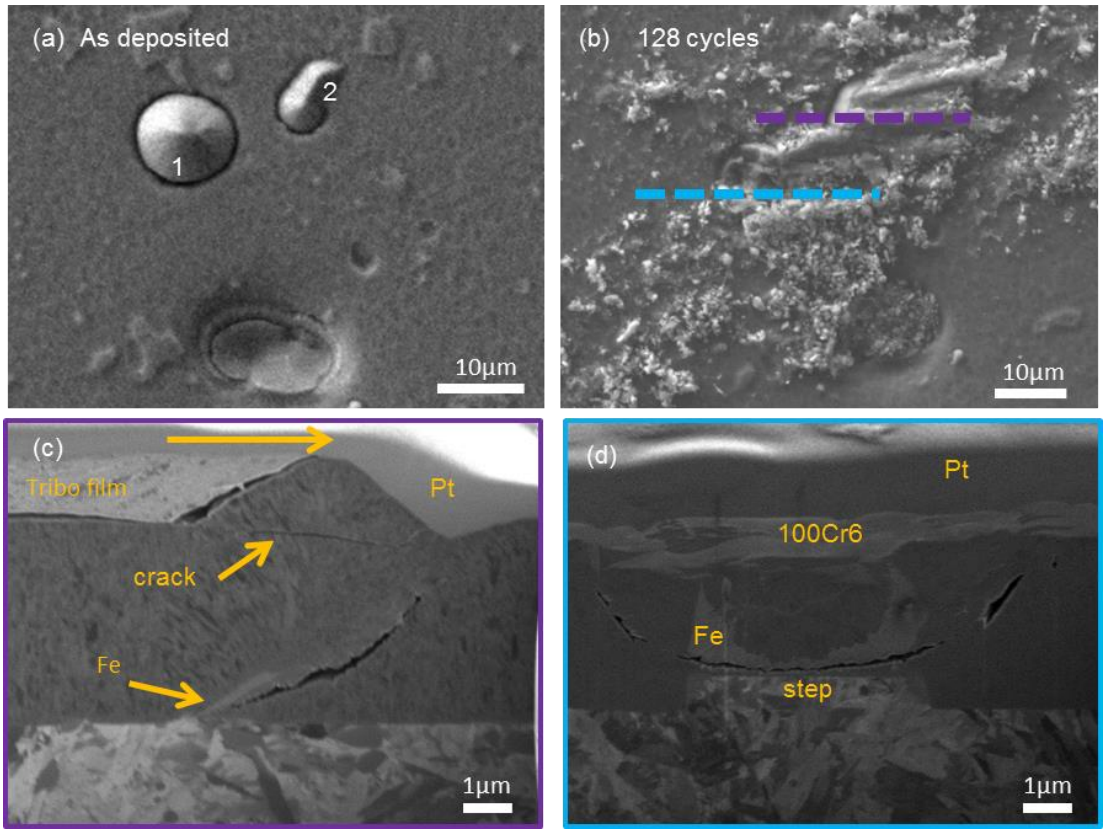


Figure 4.20: SEM image of a set of defects. (a) Prior to the tribological test, and (b) after the tests were done. (c) FIB cross section of the defect 1 and (d) defect 2.

Chapter 5

The Influence of Surrounding Atmosphere on Tribological Properties of Hard Coatings

5.1 Coating characterization

To observe the influence of tribological oxidation at room temperature during pin-on-disc experiments, we performed tests with several conventional (TiN, TiAlN and CrN) and advanced (CrAlN, CrVN) hard coatings under different atmospheres.

All the hard coatings used were deposited in the industrial unbalanced magnetron sputtering system CameCon CC800/7 or CC800/9. TiAlN (Ti:Al=55%:45%) and CrN were deposited using CC800/7 while $Cr_xV_{1-x}N$ and $Cr_xAl_{1-x}N$ coatings were deposited using triangular targets in the CC800/9 deposition system, both using DC power sources. All samples were deposited on mirror-like polished D2 steel discs. The thickness of the coatings was measured by the ball crater method of on FIB cross section. The film thickness of CrVN and CrAlN with different Cr/V and Cr/Al rations varied from 3.7 to 8.5 μm and from 4.5 to 7 μm, respectively. Their thicknesses differ due to different sputtering yields of the target material. TiAlN and CrN coatings thickness was constant at 4 μm. The measured coating properties are presented in a table 5.1

Table 5.1: Measured hard coating physical properties.

Coating	Substrate	Thickness [μm]	Total delamination force [N]	Hardness [HV]
TiN	D2	3.8	90	2900
TiAlN	D2	4.5	95	3400
CrN	D2	8.5	75	2400
CrAlN (6 at. % Al)	D2	6.5	95	2100
CrVN (6 at. % V)	D2	6.6	95	2200

The EDS compositions of advanced coatings deposited by using triangular targets are presented in Figure 5.1. Depending on the vertical position the amount of aluminum or vanadium changes from 1 at. % to approximately 12 at. %. For the experiments only three from each group were tested, namely the samples with 1 and 12 at.% of alloying element and the sample in the middle (6 at.%).

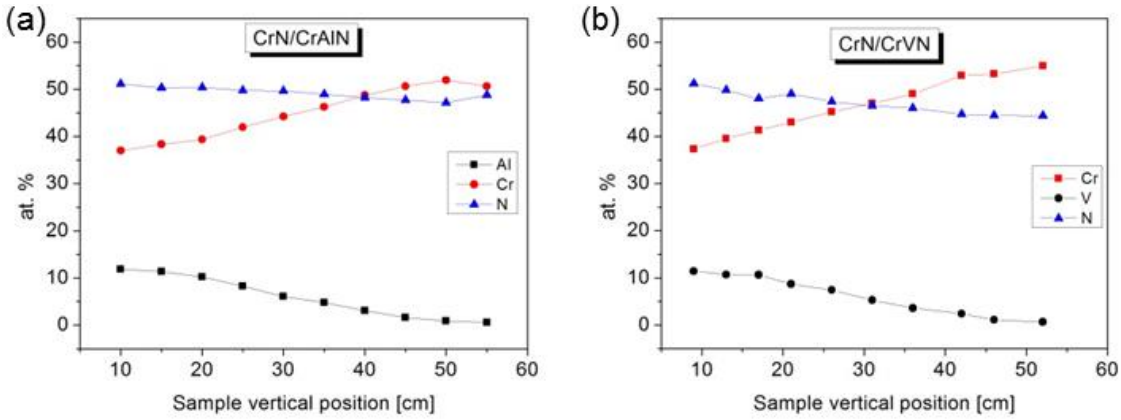


Figure 5.1: Average composition obtained by EDS of (a) CrN/CrAlN and (b) CrN/CrVN hard coatings at different sample vertical positions in the deposition chamber.

The measured XRD patterns of coatings used in our experiments are presented in Figure 5.2. The crystal structure of all the coatings is f.c.c. We noticed the (111) peak shift in the chromium-based coatings due to alloying with aluminum or vanadium. Different deposition rates of chromium versus aluminum or vanadium were detected in vertically positioned samples (as presented in Figure 3.2). Because of this, a small variation of the peak width, caused by the grain size, can be noticed in chromium-based coatings.

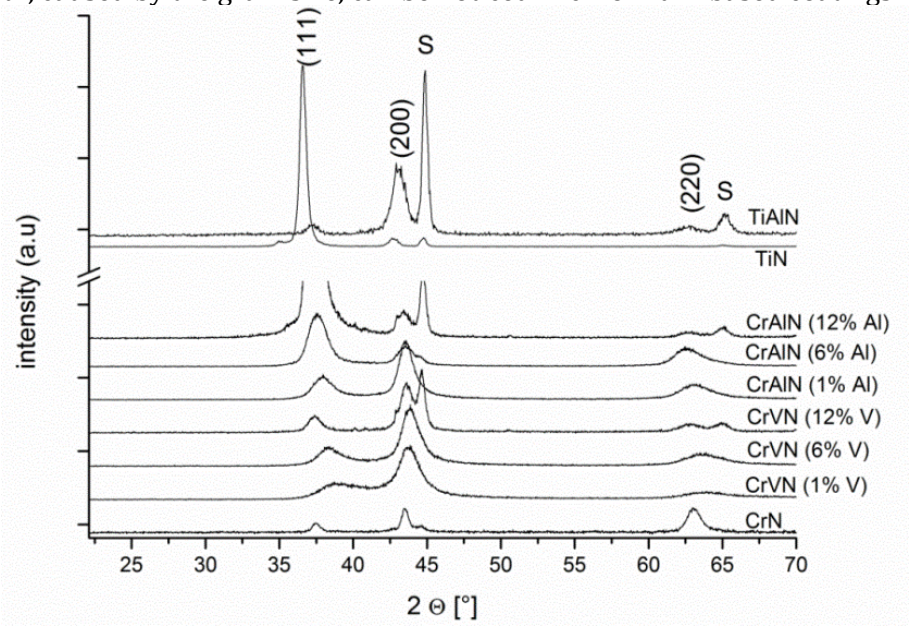


Figure 5.2: The XRD patterns of hard coatings used in tribological experiments. *S* denotes the peak of the substrate; peaks denoted by (111), (200) and (220) belong to hard coating.

5.2 Results

5.2.1 Friction and wear in ambient air atmosphere

The results in Figure 5.3 show COF and wear behavior of different hard coatings sliding against alumina counterbody in ambient air atmosphere.

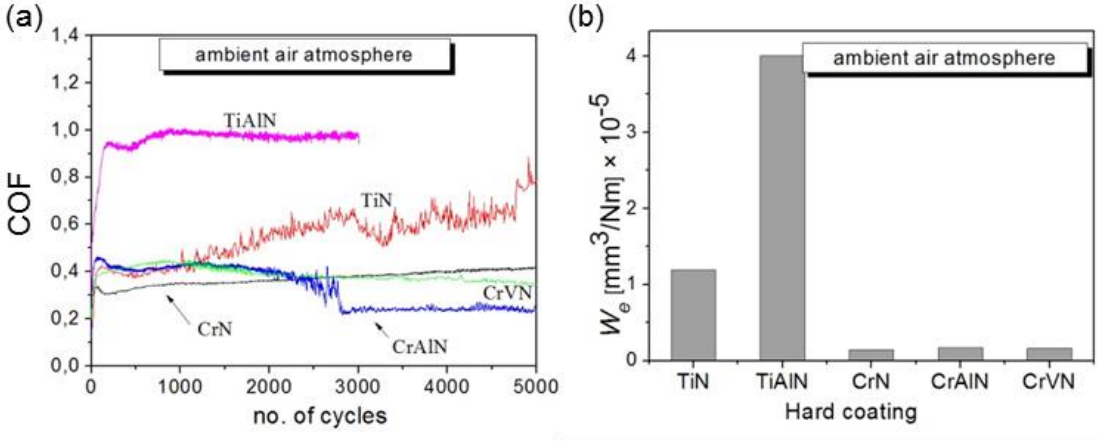


Figure 5.3: Ambient air measurements: (a) COF measurements of different hard coatings in ambient air atmosphere and (b) relative wear rates.

During the running-in, when the nodular defects are leveled with the surface, the COF quickly rises from 0.2 up to 0.9 for TiAlN coating or to approximately 0.4 for all the other hard coatings tested. From Figure 5.3 (a) and (b) it is evident that the TiAlN coating reaches the highest COF values as well as the highest relative wear of the coating. Although the COF values are different, the course of the COF in the first 100 cycles is similar in all the coatings, which shows that the initial processes are the same as described in the previous chapter.

After additional sliding the TiAlN coating COF rose to a stable value of 1.0 after approximately 1000 cycles. CrVN and CrAlN (6 at. % Al or V) coatings both experienced a decrease of the friction coefficient with an exception of the rapid friction coefficient drop for CrAlN coating by 0.1 after 2800 cycles. This could be because of weakly bound debris by water molecules which forms a thin lubricated film [43]. TiN exhibited a continuous increase of the COF through the whole test length showing the highest scattering in COF values. The wear rates of the coatings are well correlated with the friction values. The highest is for TiAlN and TiN hard coatings. CrN coating shows the most stable COF value. All chromium-based coatings exhibit only minor wear rate, approximately one tenth of that for TiN.

5.2.2 Friction and wear in nitrogen atmosphere

The tests on the same samples were repeated in the nitrogen atmosphere. By a continuous flow of the nitrogen we prevented the intake of oxygen at the tribological contact. The inert and moisture-free environment caused a substantially different friction and wear behavior (Figure 5.4).

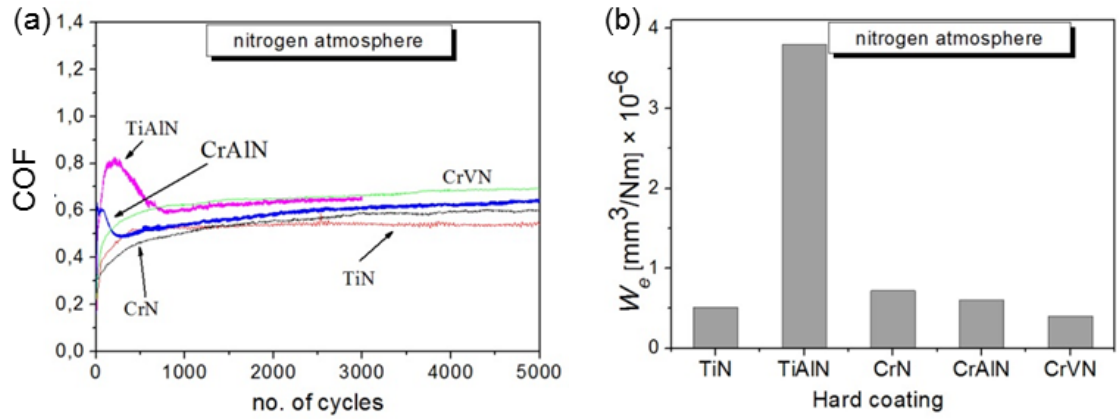


Figure 5.4: Nitrogen atmosphere measurements. (a) COF measurements of different hard coatings in nitrogen atmosphere and (b) relative wear rate.

With an exception of coatings that contain aluminum, similar behavior in the remaining coatings can be observed. The COF running-in period is longer which indicates that the breaking and powdering of the nodular defects runs more slowly than in the ambient air atmosphere. Interestingly, the TiAlN and CrAlN coatings exhibit in the running-in a friction bump that gradually subsides closer to the COF value of the other coatings. Such behavior could be explained by the formation of hydrated oxides that can form during storage of test samples in the ambient air, as already mentioned in the theoretical part of the thesis [101, 102]. This top oxide layer is then worn down after some initial laps in the pure nitrogen environment, while the oxide layer is continuously growing when testing in the pure oxygen or ambient air environment [111]. The wear rate for all the coatings tested in nitrogen decreased in comparison to those obtained in the air conditions. TiN and TiAlN exhibit up to 10 times lower wear rate, while with the chromium based coatings the wear rate change was smaller.

5.2.3 Friction and wear in oxygen atmosphere

In contrast to nitrogen atmosphere the oxygen atmosphere promotes the tribochemical reactions. The influence of oxygen on friction and wear behavior is presented in Figure 5.5.

In the running-in period of the test all coatings have a similar course to that in the ambient air measurements. TiAlN coating COF behaves almost identically to ambient air measurements while its wear is smaller. TiN reaches the highest COF and as in ambient air measurements, while the COF values scatter a lot. The behavior of chromium based coatings is similar. The steady state values are constant at 0.7 and 0.75 for CrAlN and CrVN coatings which are almost double the value of the ambient air measurement. The CrN coating exhibits a bit different behavior; after an initial jump of friction coefficient from 0.2 to 0.5 the friction coefficient decreases to 0.45, and after the following 800 cycles increases again up to 0.63. While in general all the coatings with an exception of TiAlN have higher COF values in oxygen atmosphere, their wear remains similar to the wear in ambient air measurement.

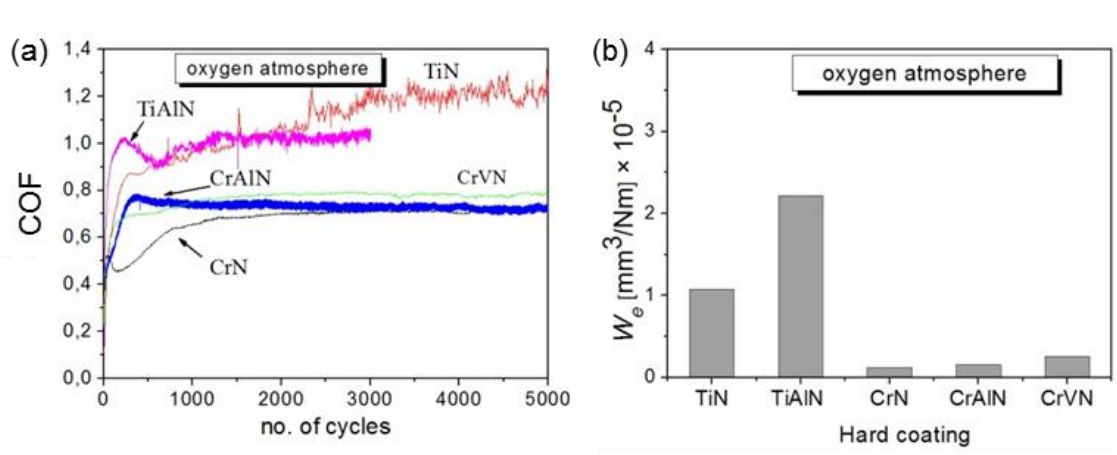


Figure 5.5: Oxygen atmosphere measurements. (a) COF measurements of different hard coatings in pure oxygen atmosphere and (b) relative wear rates.

5.2.4 TiN wear track analysis

Figure 5.6 presents the images of the TiN wear track after 5000 cycles sliding at **ambient air** test conditions. In (a) the secondary electron (SE) image (Figure 5.6a) presents the end of the wear track. At this point a large amount of wear debris accumulates. From (a) and (c) it can be noticed that the wear track is relatively smooth, having only a few grooving marks at the edges. On the backscattered electron (BSE) image the wear debris appear black on this image.

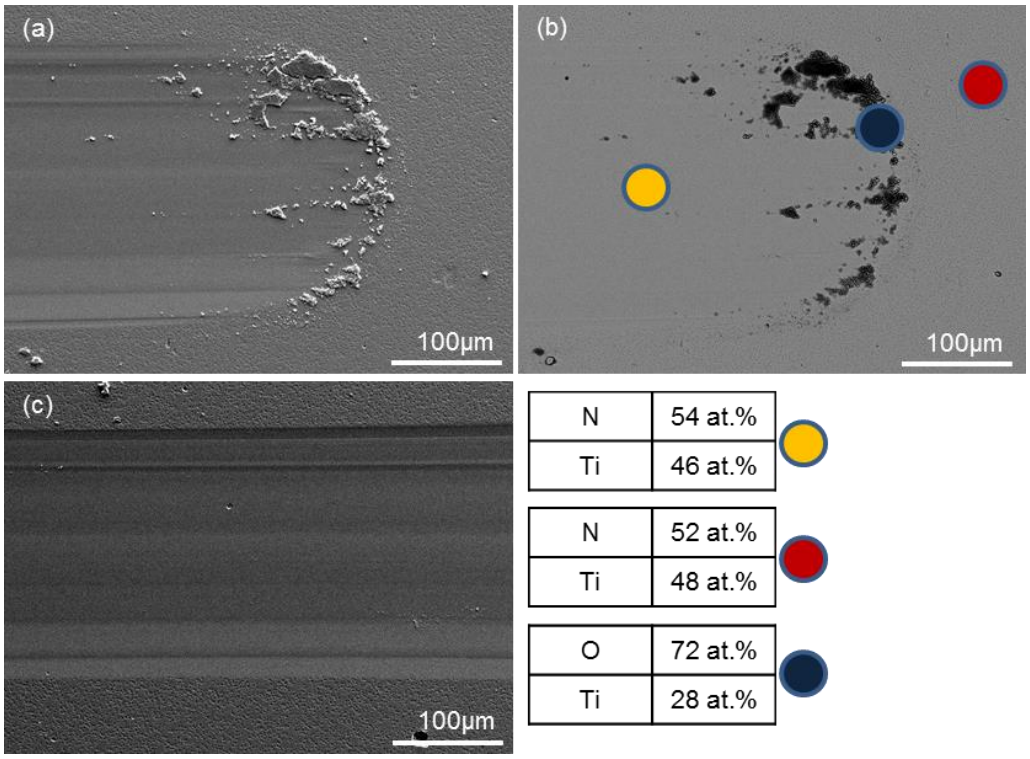


Figure 5.6: SEM analysis of a wear track made in ambient air test. (a) Secondary electron and (b) backscattered image of the wear track end in ambient air. The colored markings mark the positions of EDS analysis, presented below. (c) SEM image of the wear track at the middle.

The EDS analysis confirms that the debris consists of a fully oxidized titanium i.e. TiO_2. We performed the EDS analysis of the wear track and compared it with the composition of the hard coating outside the wear track. Although we did not detect any significant

compositional differences, it is most likely that the wear debris origin is from the thin tribo-oxide layer that forms during sliding.

Due to the absence of oxygen when sliding in pure nitrogen environment, the tribo-oxidation of the surface is severely reduced. This results in low wear rate of the hard coating and hence a small amount of wear debris accumulated at the wear track end. Figure 5.7 presents the wear track after 5000 cycles sliding in **nitrogen atmosphere** and conducted EDS measurements.

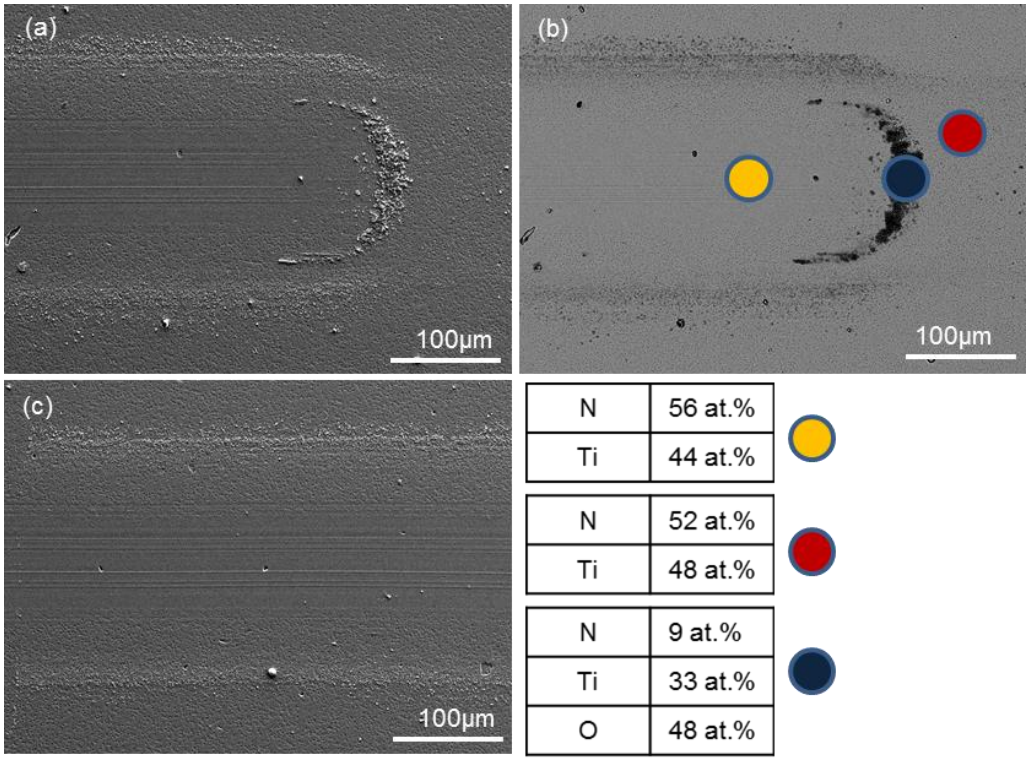


Figure 5.7: SEM analysis of a wear track made in nitrogen atmosphere test. (a) SE and (b) BSE image of a wear track end after 5000 cycles in nitrogen. The colored marks show the positions of EDS measurements, presented below. (c) SE image of wear track at the middle.

The wear rate in nitrogen environment is very small. In (c) the small holes and remains of nodular defects can be noticed. The width of the wear track is smaller compared to the one made in ambient air atmosphere. Shallow horizontal grooving lines are clearly visible. They indicate that the abrasion action of the counterbody is the major wear mechanism removing only the thin oxide layer which formed during the storage of samples in ambient air due to physi-adsorbed oxygen and water. BSE image (b) and EDS analyses showed that only the wear debris was oxidized.

In contrast to the nitrogen environment, the BSE imaging of wear tracks made in pure oxygen reveal a minor contrast between the wear track and the coating surface. Moreover, the larger difference is in the amount of wear debris and their structure. In ambient air the wear debris form patch-like structures probably because of the moisture (RH) that binds them loosely together. In pure oxygen environment the atmosphere is moisture-free, thus the wear debris are in the form of small particles (Figure 5.8 (b)). Apart from a highly oxidizing environment that promotes tribo-oxidation, also the individual tribological products may act in an abrasive manner, thus adding to higher COF and relative wear values compared to ambient air measurements. To support the assumption of the abrasive particles in the wear track the grooving traces in the middle of the wear track length are clearly visible. In all TiN tests the EDS showed the oxidized wear debris.

The TiN coating behavior is severely influenced by the formation of hydrophilic TiO_x [101]. The relative high friction coefficient and its large oscillations in oxygen and the ambient air environment could be related to shearing of the amorphous debris [112]. The

higher friction coefficient in the oxygen environment is influenced by the absence of moisture which can weakly bind the debris. It was reported that the debris could form a thin low-friction tribological layer [43]. The oscillations in COF are not noticeable in the nitrogen environment where the oxidation process is suppressed.

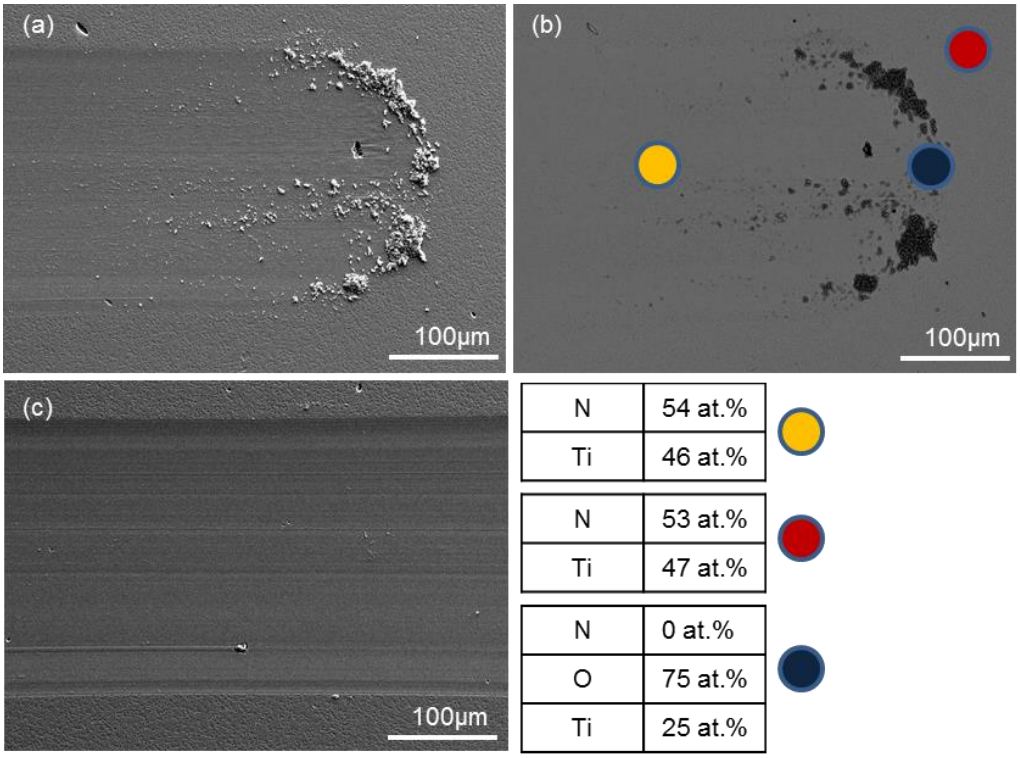


Figure 5.8: SEM analysis of a wear track made in the oxygen atmosphere test. (a) SE and (b) BSE images of a wear track end after 5000 cycles in oxygen. The colored marks show the positions of EDS measurements, presented below. (c) SE image of wear track at the middle of the wear track length.

5.2.5 TiAlN wear track analysis

TiAlN hard coating performed the worst amongst all the hard coatings tested. In **ambient air** tests the TiAlN coating has the highest COF and about four times higher relative wear volume than that of the TiN coating. Figure 5.9 presents the wear track analysis of the ambient air tests. On all the images we notice that the wear debris not only accumulates at the edges of the wear track but is scattered along the entire wear track surface. BSE image reveals that some oxidation of the wear track occurred. The surface within appears darker than the surface outside the wear track. Even though the BSE image shows some contrast, the EDS measurements did not show any significant difference in the coating composition inside or outside the wear track. We believe that this is due to the relatively strong electron beam interaction volume at 15 keV. At this energy, the interaction volume is much larger than 1 µm in depth thus the signal from the few nanometer thick oxide layers is hard to obtain. EDS showed that the wear debris appears to consist of a mixture of pure titanium and aluminum oxides since no nitrogen was detected.

SE and BSE images of the wear tracks made in the **nitrogen environment** (Figure 5.10) appear different than those obtained in ambient air conditions. In the BSE image there is no contrast difference that would indicate any surface oxidation. In COF measurements for this case we observe the friction bump at the beginning of the test (Figure 5.4). As the samples were stored in ambient air conditions oxides could form on the surface or the oxidation process at the beginning of the test could form due to the absorbed moisture on the surface. As the test starts, the junction between the surface oxides and hard counterbody produces a large COF. This layer is then gradually removed by abrasion mechanism which could cause the slow decrease of COF since due to the nitrogen

environment there are no additional oxidation processes possible. Wear debris accumulates at the edges. EDS showed that as in ambient air measurements the wear debris consists of titanium and aluminum oxides.

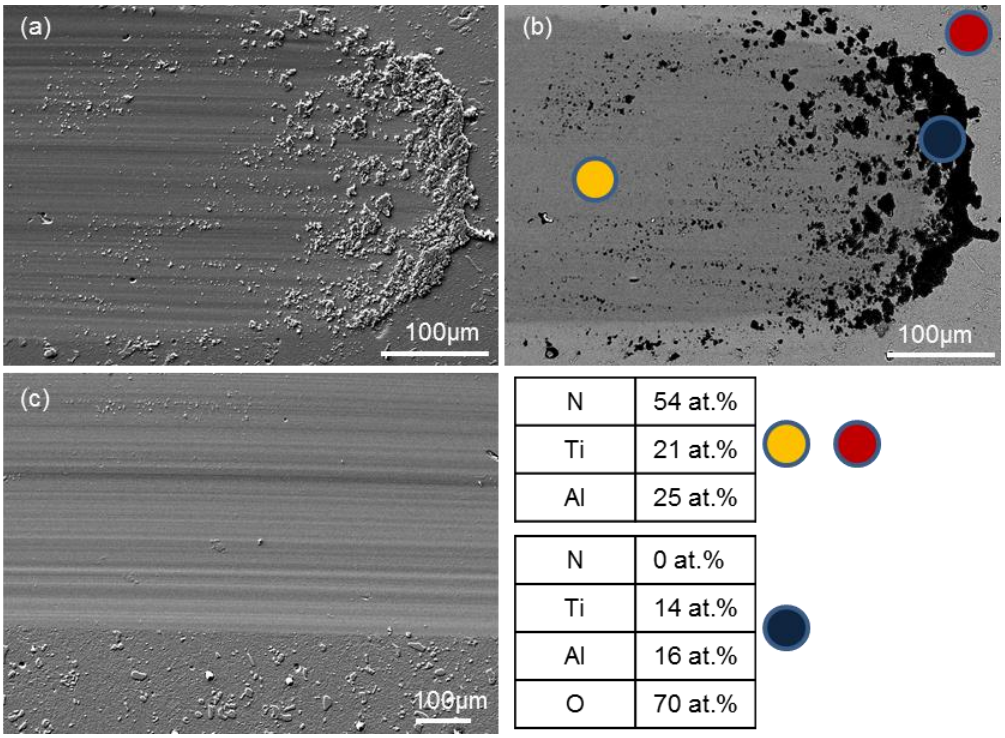


Figure 5.9: SEM analysis of a wear track made in the ambient air test. (a) SE and (b) BSE images of TiAlN wear track after 3000 cycles in the ambient air. The colored marks show the positions of EDS measurements, presented below. (c) SE image of wear track at the middle of the wear track length.

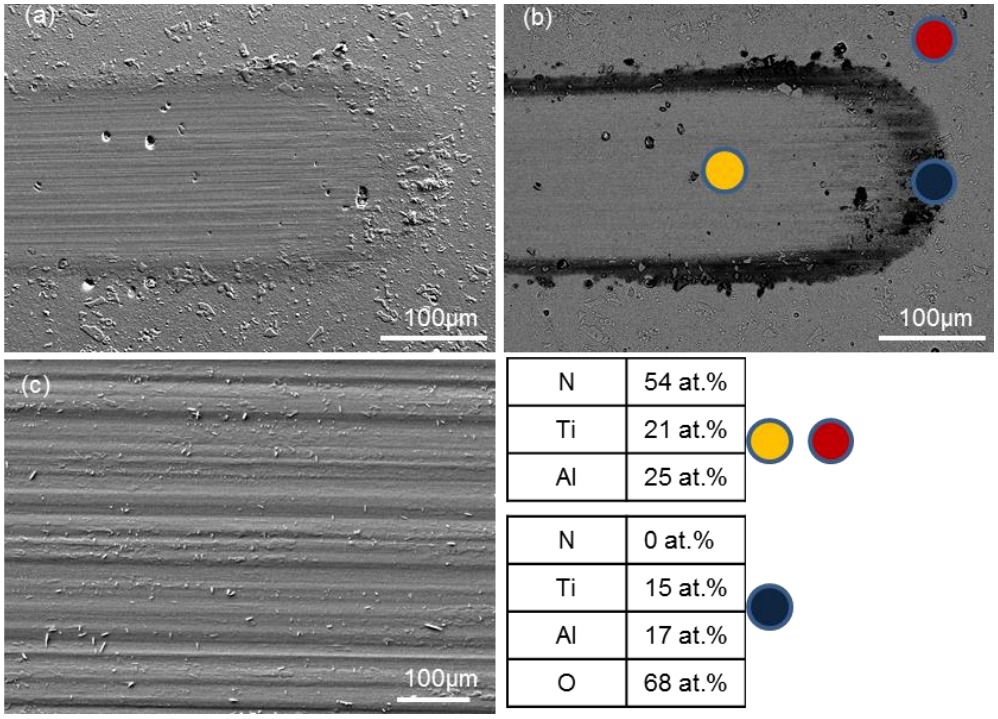


Figure 5.10: SEM analysis of a wear track made in the nitrogen atmosphere test. (a) SE and (b) BSE images of TiAlN wear track end obtained after 3000 cycles in the nitrogen

environment. The colored marks show the positions of EDS measurements, presented below. (c) SE image of wear track at the middle of the wear track length.

Higher magnification of the wear track presented in Figure 5.10 (c) reveals that the roll-like debris is present along the entire wear track surface. This type of debris is common in TiAlN coating in all atmospheres tested. The SEM analysis of the wear track on TiAlN tested in pure **oxygen** appears very similar to those obtained in ambient air (Figure 5.11).

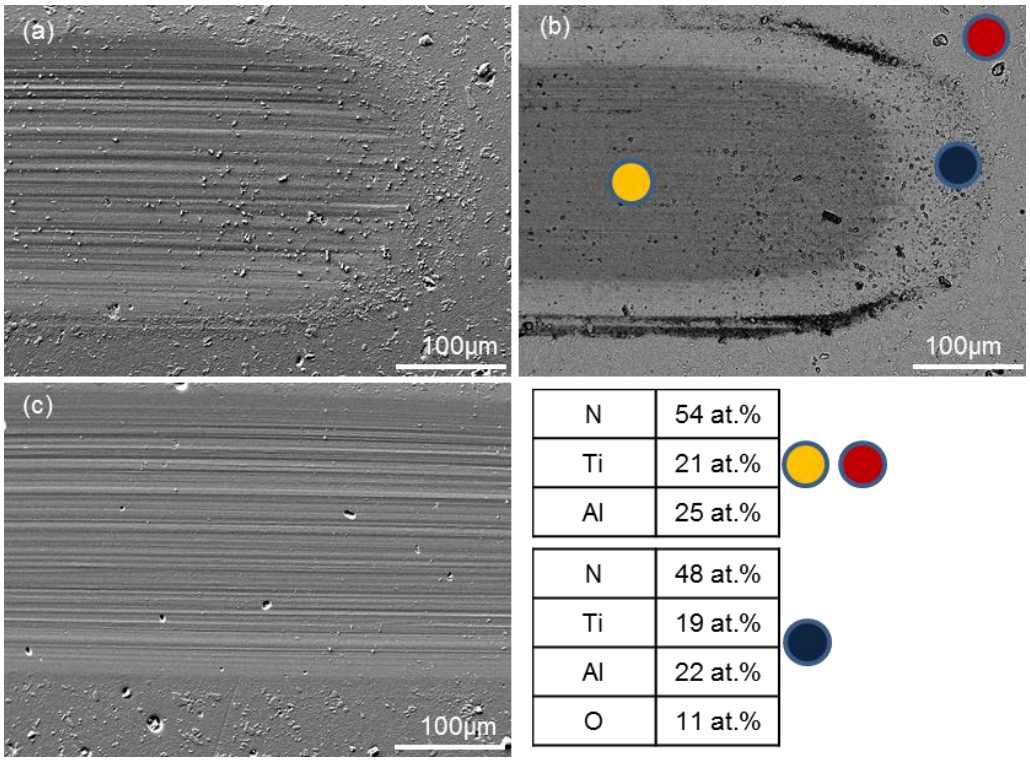


Figure 5.11: SEM analysis of a wear track made in the oxygen atmosphere test. (a) SE and (b) BSE images of TiAlN wear track obtained in the oxygen environment. The colored marks show the positions of EDS measurements, presented below. (c) SE image of wear track at the middle of the wear track length.

On the wear track grooves are visible. Debris density is smaller than that in the nitrogen environment. We also notice that the wear track formed a thin oxide layer which appears dark on the BSE image. A constant supply of oxygen to the sliding contact enabled the constant grow of the oxide layer. According to the hue of wear track in BSE image the layer is thicker compared to the ambient air test. Also comparing the wear rates we notice that the wear is smaller in the pure oxygen environment. The reason could be the formation of aluminum oxide. The attempts to detect this layer with EDS (point or mapping) have not been successful as seen from the presented EDS (Figure 5.11(b)).

5.2.6 CrN wear track analysis

5000 cycles sliding test in the **ambient air** atmosphere results in a mild wear of the CrN hard coating. The wear track is presented in Figure 5.12. It appears smooth with some horizontal grooving marks on the coating surface (c). Nodular defects in the wear track are leveled with the surface and depressions surrounding them are filled with wear debris. EDS does not show any surface oxidation, although small dark areas (which indicate the presence of surface oxides) are visible on the BSE image (b). Wear debris that were analyzed with EDS indicate the presence of chromium oxide.

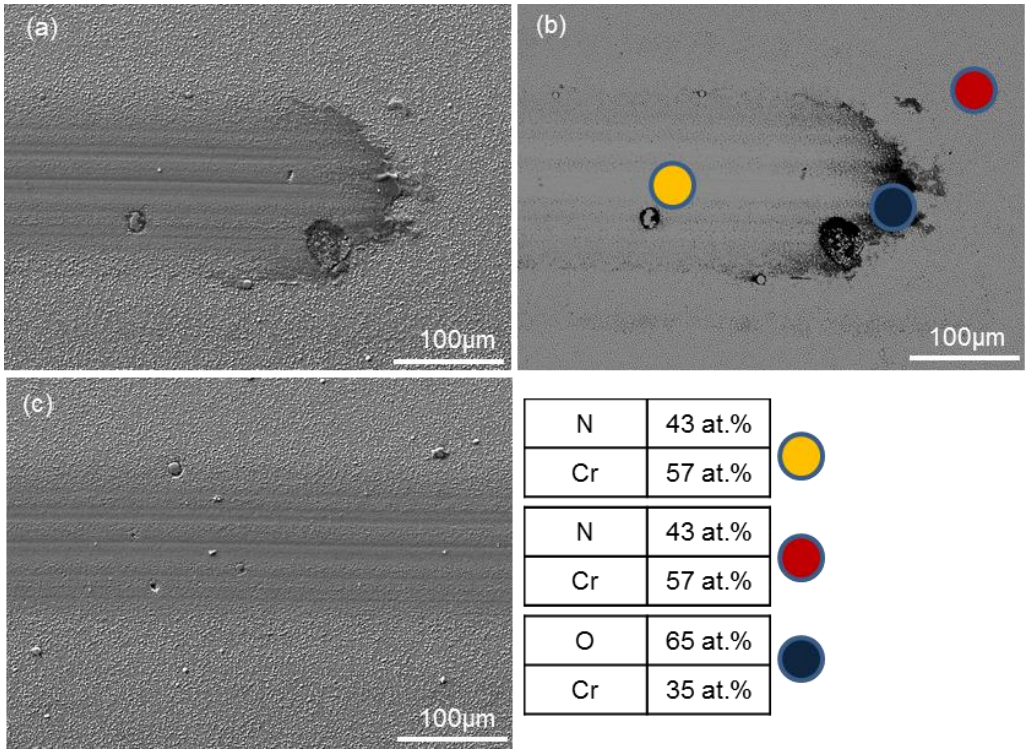


Figure 5.12: SEM analysis of a wear track made in the ambient air test. (a) SE and (b) BSE image of CrN wear track obtained in the ambient air environment. The colored marks show the positions of EDS measurements, presented below. (c) SE image of wear track at the middle of the wear track length.

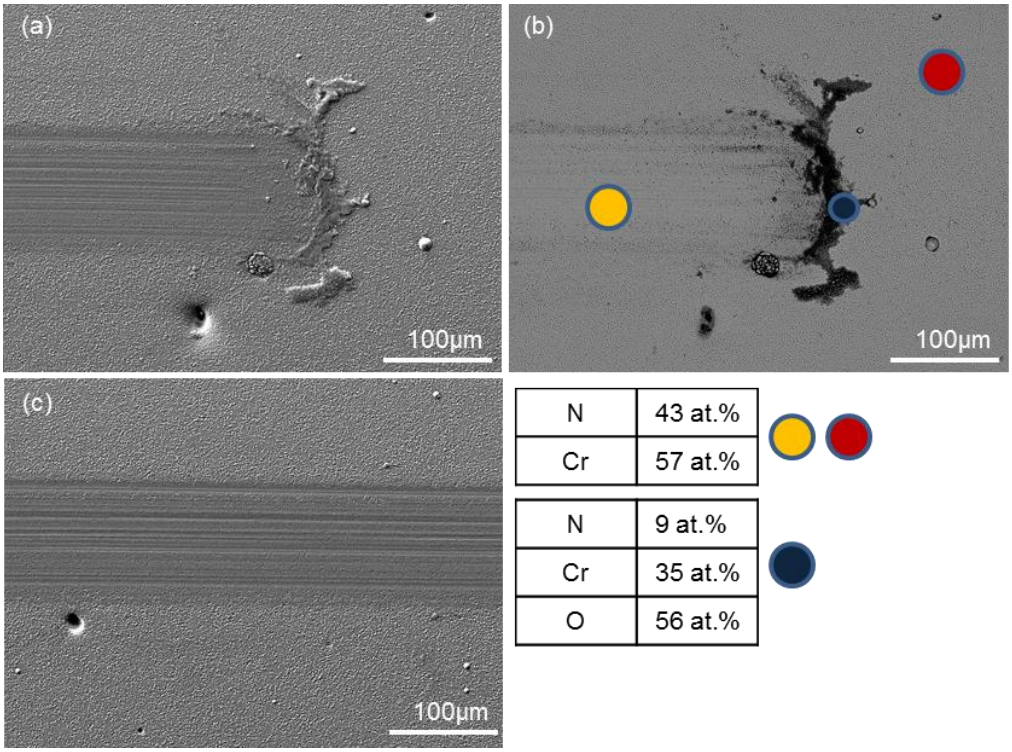


Figure 5.13: SEM analysis of a wear track made in the nitrogen atmosphere test. (a) SE and (b) BSE image of TiAlN wear track obtained in the nitrogen environment. The colored marks show the positions of EDS measurements, presented below. (c) SE image of wear track at the middle of the wear track length.

Even though the **nitrogen** atmosphere suppresses any tribological oxidation beside the one in the beginning due to the adsorbed water, there are hardly any differences in SEM images between the nitrogen and the air-induced wear tracks. These are presented in Figure 5.13. The decrease of relative change of wear is minimal, but in contrast to TiN and TiAlN coatings the average COF in nitrogen increases compared to the ambient air measurements. According to these measurements, the assumption that chromium hydroxides provide a thin low friction tribofilm at the surface may stand. EDS measurements did not show any wear track surface oxidation, but in contrast to other coatings we detected some nitrogen in wear debris at the end of the wear track. This could indicate the presence of CrN coating particles or thin oxide layer.

In the **oxygen** atmosphere COF increases compared to the ambient air measurements, but, interestingly, the relative wear rate is the same. SE and BSE images of wear tracks are presented in Figure 5.14.

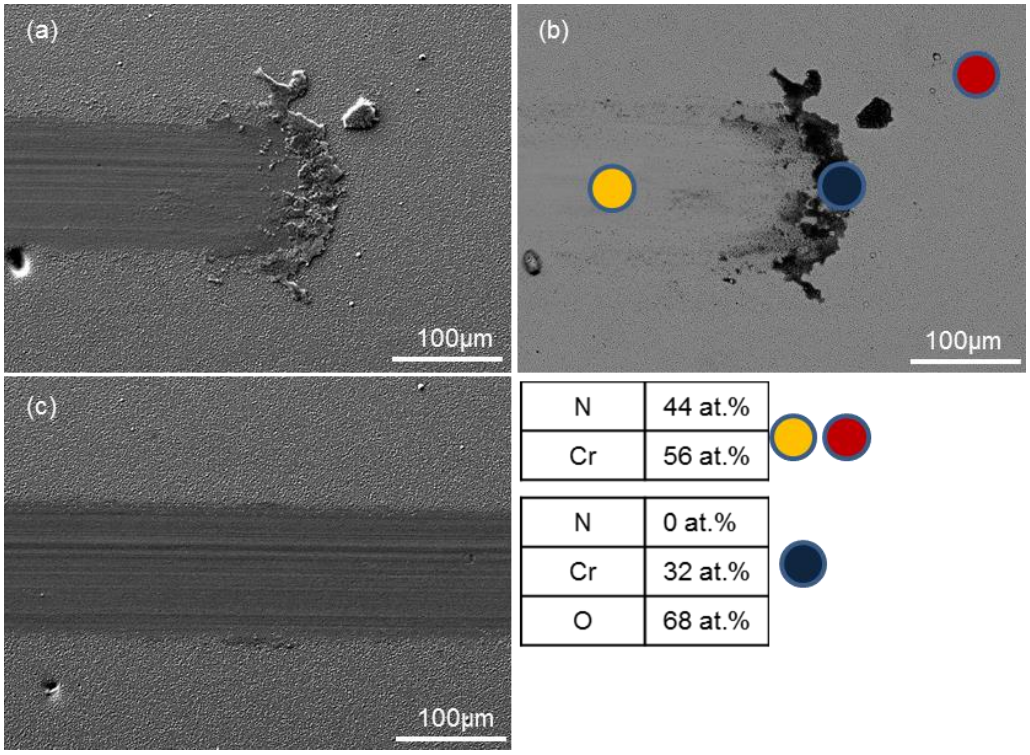


Figure 5.14: SEM analysis of a wear track made in the oxygen atmosphere test. (a) SE and (b) BSE images of CrN wear track obtained in the oxygen environment. The colored marks show the positions of EDS measurements, presented below. (c) SE image of wear track at the middle of the wear track length.

Quick inspection of the wear track does not show any large differences with previous atmospheric test conditions. The higher magnification reveals that the surface oxidation occurred. Larger oxide surface coverage increases COF. In the oxygen atmosphere the COF is the highest among all tested conditions. As shown in Figure 5.15 this causes destructive processes. Higher tangential forces are responsible for the formation of cracks. In Figure 5.15(a) we can see that cracks are more frequent on the oxide regions. The FIB cut through showed that cracks are up to a few microns deep (approximately 2.5 µm).

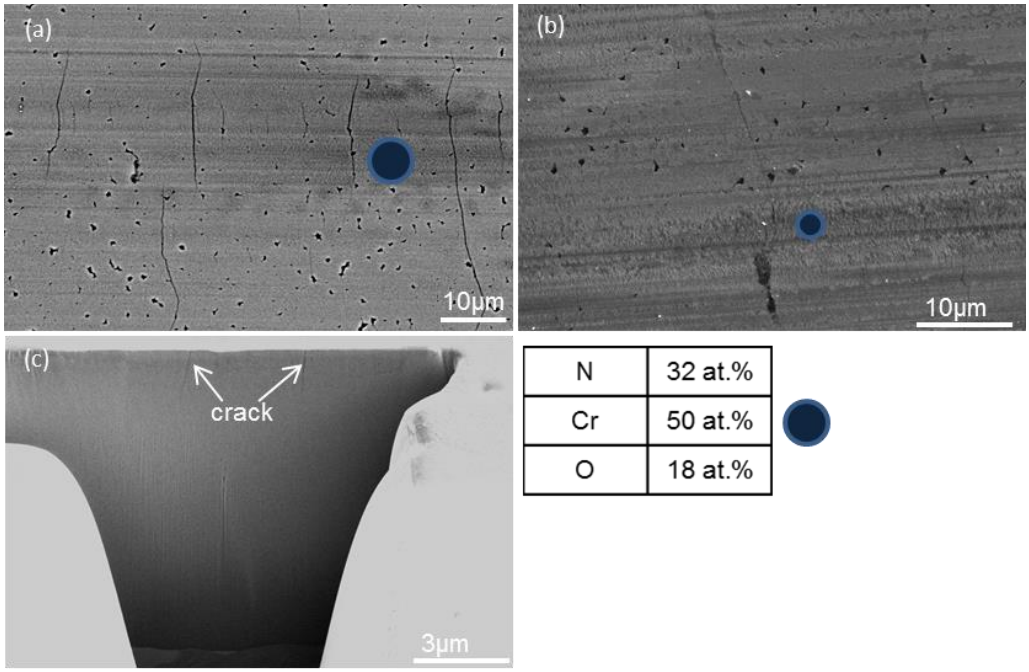


Figure 5.15: FIB analysis of CrN wear track after the oxygen atmosphere test. (a) BSE image of the CrN wear track showing oxide regions. (b) Higher magnification showing oxide film patches with cracks (c).

5.2.7 CrAlN and CrVN wear track analysis

Due to similar behavior in friction and wear of CrAlN and CrVN coatings we describe tribological behavior of both coatings simultaneously. In Figure 5.16 wear track on the CrVN hard coating induced in **ambient air** is presented. Chromium based coatings behave in a similar way. The wear is minimal, with the majority of wear debris collected at the end edge of the wear track. The highly dense horizontal grooving marks are from time to time interrupted with small oxide patches in an otherwise smooth wear track. These patches are encircled on image (c). The EDS showed that only wear debris were oxidized. In **nitrogen** environment the wear is further reduced. Image Figure 5.17(a) shows a 200 µm wide wear track with deep grooving lines in the middle. Closer observation (c) shows that the wear occurred only by grooving the coating surface leaving other parts of the wear track mildly damaged i.e. leveled surface irregularities. BSE image (b) shows the wear debris accumulated at the wear track edges. Some debris is also smeared at the surface protrusions outside the grooves. EDS in both coatings showed that only the wear debris was oxidized. COF for CrAlN and CrVN is different at the beginning of the sliding since aluminum containing coatings exhibit a small hump which disappears in further sliding (Figure 5.4). The mechanism for appearance of the bump is most likely the same as in the TiAlN hard coating. Similar as in CrN coating the COF is higher in nitrogen environment than in ambient air conditions for both coatings.

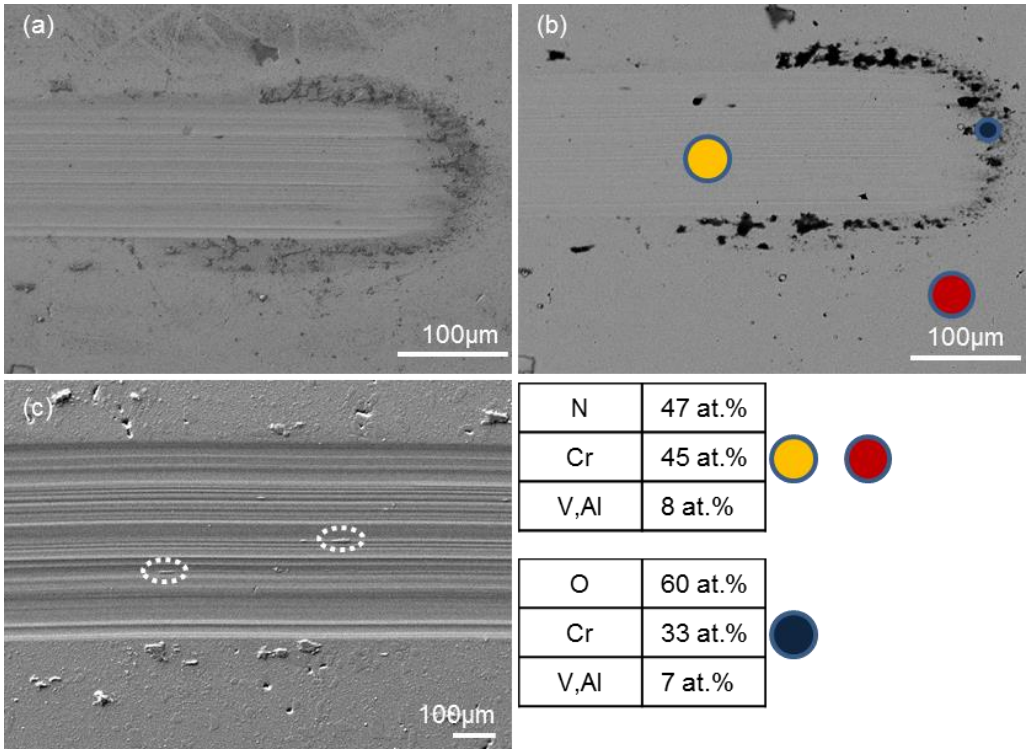


Figure 5.16: SEM analysis of a wear track made in the ambient air test. (a) SE and (b) BSE images of CrVN wear track obtained in the ambient air environment. The colored marks show the positions of EDS measurements, presented below. (c) SE image of wear track at the middle of the wear track length.

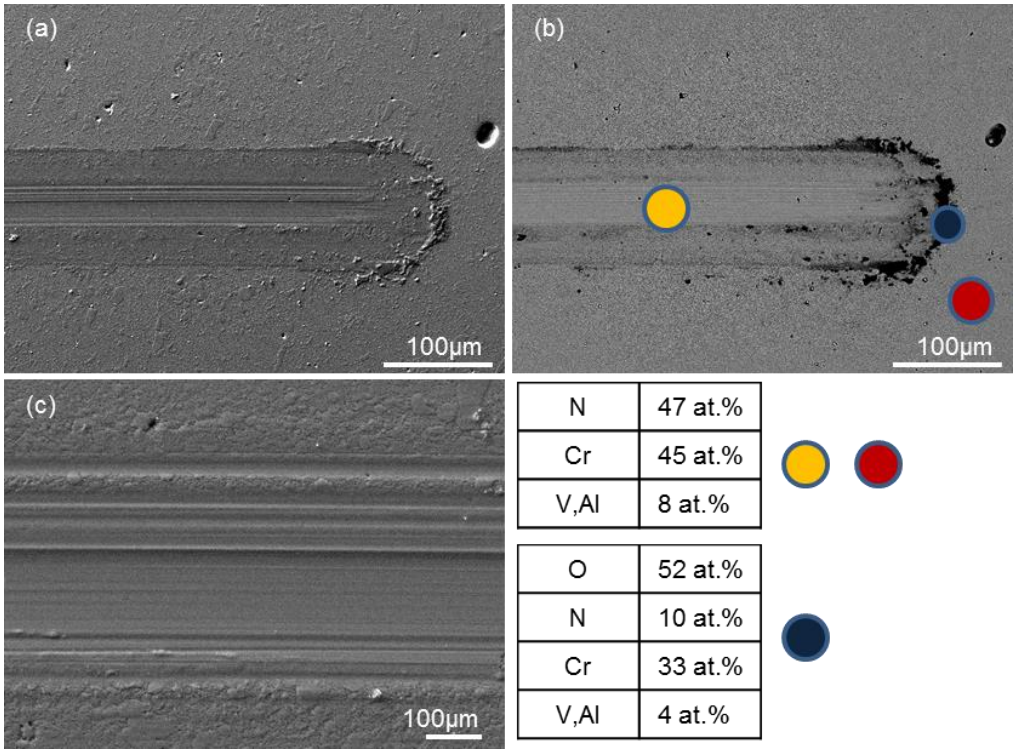


Figure 5.17: SEM analysis of a wear track made in the nitrogen atmosphere test. (a) SE and (b) BSE images of CrVN wear track obtained in the nitrogen environment. The colored marks show the positions of EDS measurements, presented below. (c) SE image of wear track at the middle of the wear track length.

The tribo-oxidation processes are the most noticeable in the oxygen atmosphere (Figure 5.18).

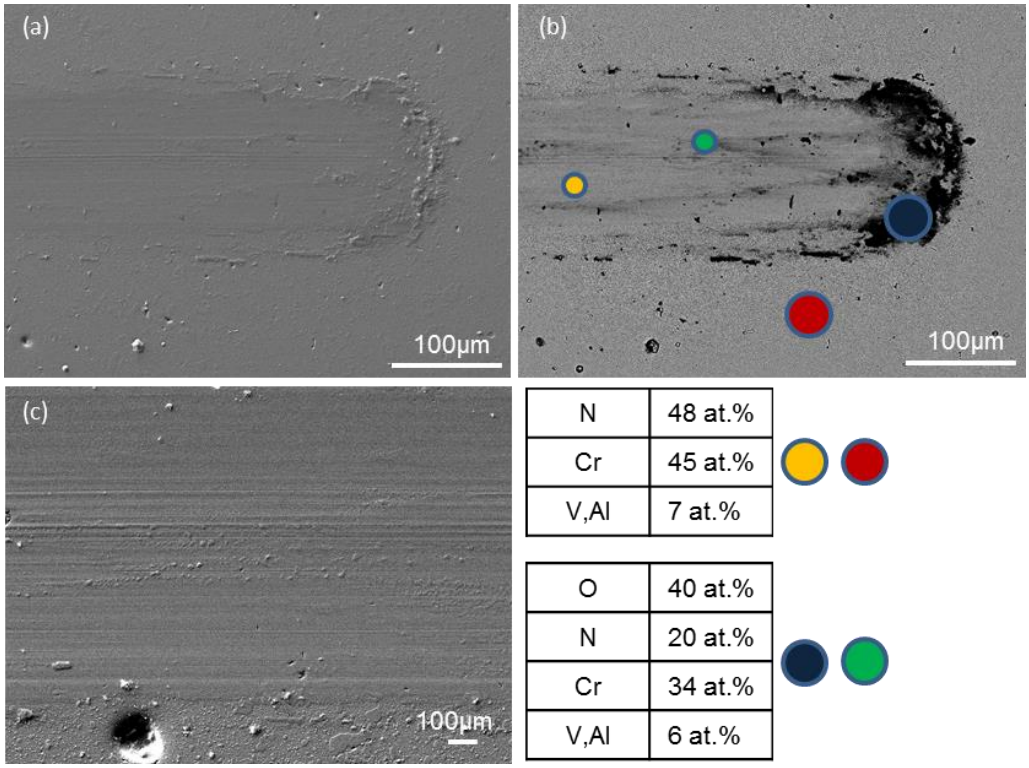


Figure 5.18: SEM analysis of a wear track made in the oxygen atmosphere test. (a) SE and (b) BSE images of CrVN wear track obtained in the oxygen environment. The colored marks show the positions of EDS measurements, presented below. (c) SE image of wear track at the middle of the wear track length.

In all chromium-based coatings (CrN, CrAlN and CrVN) we found tribo film patches in the wear track obtained in the **oxygen** atmosphere. Such patches were not found in the ambient air nor in nitrogen-induced wear tracks. Optical micrographs of the wear track obtained in the oxygen environment show that the color of the coating surface is different in comparison with those obtained in nitrogen. The latter tracks resembled the color of the polished coating itself, but in the oxygen environment the wear track was black (not shown here). EDS analysis of the wear track revealed that both wear debris and film patches in the wear track contained oxygen. This film was not continuous through all the surface of the track, but was more concentrated in the middle of the track. A detailed SEM analysis showed that the pattern was constructed from **fish-scale-like structures** as can be seen in Figure 5.19. Presented EDS mapping shows that only this surface is formed from oxides, while the neighboring flat regions do not contain any oxides.

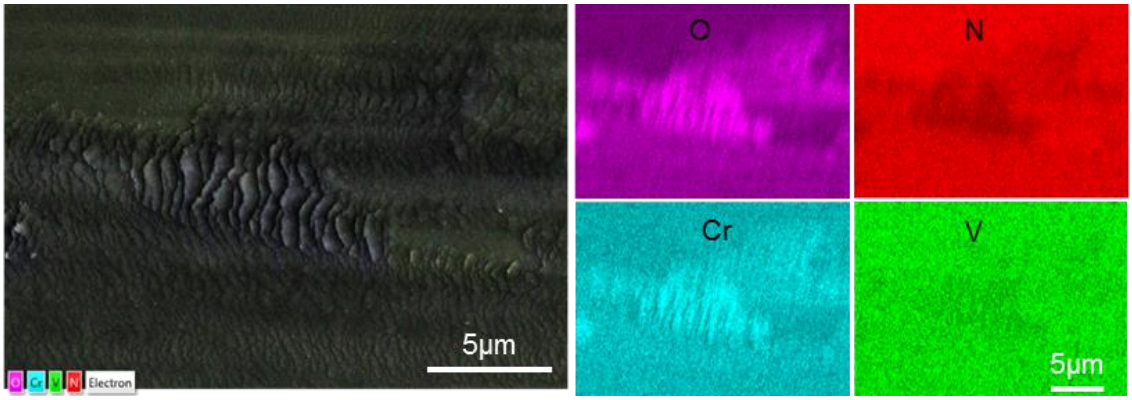


Figure 5.19: EDS mapping of fish-scale-like structures in CrVN wear track.

From the color intensity in EDS mapping we notice that fish-scale-like structures are constructed from chromium oxide since an absence of nitrogen and vanadium is clearly seen. To determine the thickness of this layer we performed a FIB cross section (Figure 5.20).

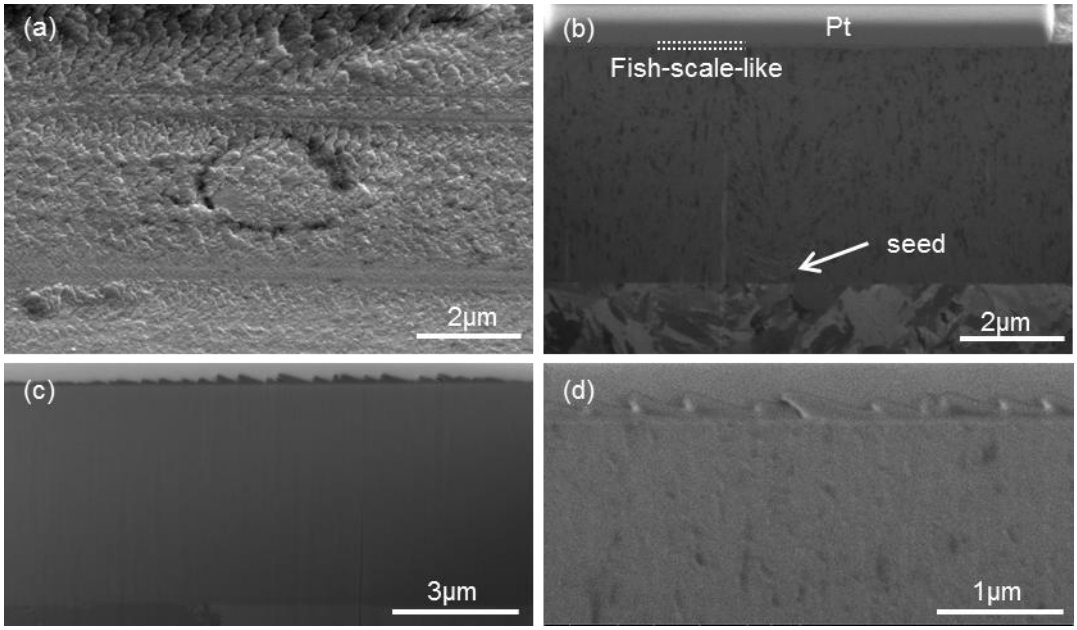


Figure 5.20: FIB analysis of nodular defect after oxygen atmosphere test. (a) Nodular defect covered with oxide layer. (b) Cross section through a defect and the fish-scale-like structure in cross section (c, d) of CrVN coating.

From this FIB image we see how the oxide layer is growing over the nodular defect, covering the depression surrounding it. The FIB cross section revealed the defect seed (iron) which landed on the surface during coating deposition. On image (b) we marked the approximate thickness of the oxide layer. This is then shown in BSE image (c) where it is presented in darker contrast. From ion image (d) the approximate thickness of 200 nm can be determined. Interestingly all the peaks of the oxide layer are tilted in the same direction and a clear boundary at the coating surface is seen, hence the adhesion of this layer is low. As the thickness grows to a certain height, the fish-scale-like structures are removed by the passing counterbody and discarded in the form of wear debris. It is not the first time that such structures were reported. Luo et al. [113, 114] reported on similar behavior observed in the first cycles of the wear. Their origin, formation and role in the tribological process is not yet known.

In order to discover the origin of these patches we performed tribo tests on the samples with different amounts of alloyed material (1 % < Al, V < 12 %). BSE images of the central region of the tracks for different composition of CrAlN and CrVN coatings are

presented in Figure 5.21. These images confirm that the amount of oxides depends on the Al/Cr and V/Cr atomic ratios. As can be seen, the amount of oxide layer grows with the amount of alloyed material. When the fish-scale-like material is removed by tangential forces acting on the surface, it leaves a clean non-oxidized surface behind. This process continues as the main oxidation driven wear mechanism.

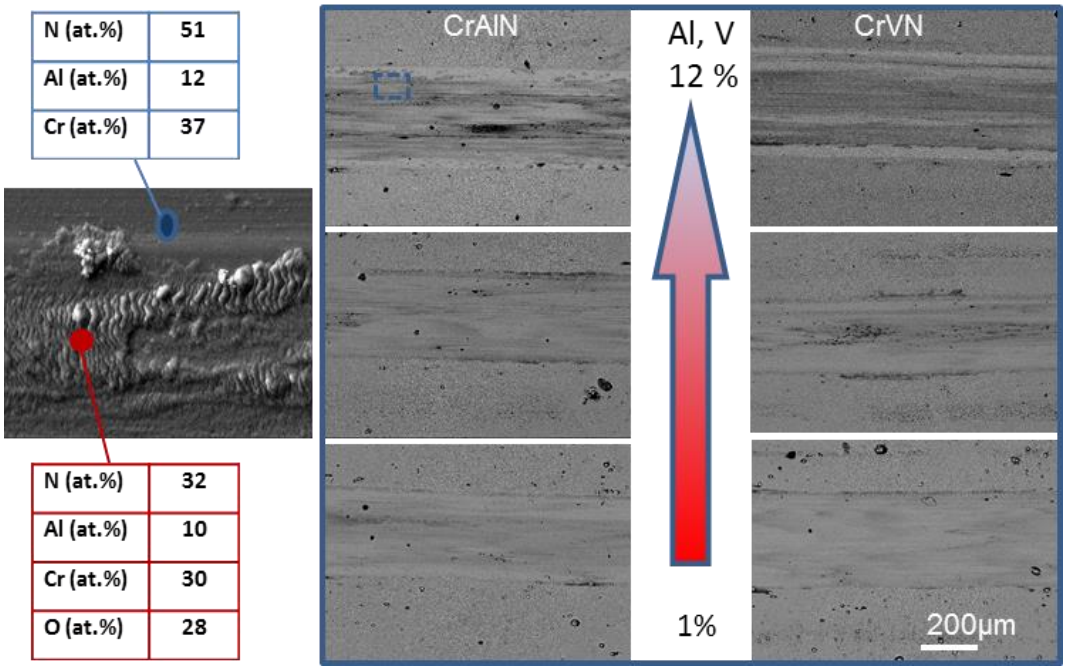


Figure 5.21: SEM images of CrVN and CrAlN wear tracks in an oxygen environment. Darker areas present fish-scale-like oxide patches, presented in more detail on the left image.

Chapter 6

Discussion

The tribological tests of TiAlN hard coating presented in this thesis were performed using of two counterbody materials (alumina and 100Cr6), sliding in two different modes, unidirectional and reciprocal. With the **cycle-to-cycle** approach, it was shown how the nodular defects influence the tribological performance of TiAlN hard coatings.

As the coating and counterbody material surface are put together, the **first junctions** between the surfaces are formed **at the sites of nodular defects**. This happens independently of the counterbody material selection.

When sliding with hard **alumina counterbody,** the nodular defects experience breaking and powdering. The formation of oxide products on the defect sites and debris accumulation can also be noticed as the sliding continues.

In the first cycle only the highest nodular defects form a contact with the counterbody. This is visible from Figure 4.3(a) and Figure 4.10 for reciprocal and unidirectional sliding mode, respectively. The pressure acting on nodular defects causes their breaking. This forms large defect particles. At this very early stage the newly formed wear debris are not removed from the wear track as indicated in Figure 4.4 and Figure 4.10. As the sliding continues, the nodular defects experience additional damage. This can result in:

a) the **complete removal** of the nodular defect top,
b) the defect **crumbling into smaller particles** with wear debris spread all around the wear track and, in some cases,
c) the nodular defect can be crushed with the defect particles being **compressed and smeared** at the nodular defect site.

FIB examination of the latter two cases is presented in Figure 4.4. From these images it can be noticed that in the case where the defect particles are compressed, a large section of the defect is not damaged. This way, the remaining defect can act as an anchorage site for the debris. In contrast, when the defect is fully crushed it cannot act as an anchorage site, subsequently the defect particles can be removed and scattered along the wear track. The latter was noticed in (unidirectional mode) in Figure 4.13 were nodular defects were crushed and their surface was filled with partly oxidized material from the defect itself and the counterbody. The EDS mapping confirmed the presence of alumina counterbody particles as there is no titanium detected in the debris (Figure 4.14). Wear of the alumina ball is minimal. The wear scar on the ball is approximately 180 μm wide.

At the end of the running-in period the nodular defects in the middle of the wear track are worn out. Two newly observed mechanisms come into play. The first one noticed is the oxidation of the hard coating surface and the second one is the formation of grooves in the wear track. These two mechanisms are probably behind the creation of the **roll-like debris** which is initially observed only at sites where the counterbody came into contact with the hard coating. These are poorly adhered oxidized particles (Figure 4.12), which is typical debris for TiAlN sliding against alumina [108-110]. Roll-like debris is spread all across the wear track, but their density is higher in the vicinity of the grooving marks. Grooves and roll-like debris happen simultaneously, neither of them was noticed before the removal of nodular defects. Such features were not noticed when sliding with **100Cr6 counterbody**.

When sliding with softer counterbody some wear processes are common to the sliding with alumina counterbody. The nodular defects also experience the **breaking** under normal load, but this is not as frequent event as when sliding with alumina ball. From Figure 4.7 it can be noticed that in the first eight cycles none of the nodular defects were broken. The galling of the ball material on the coating surface is also visible and only a minor part of the nodular defect presented in (a) broke. Defect particles can also be found

on the steel ball wear surface, see Figure 4.19 (d). This confirms the breaking mechanism of nodular defects in the case of softer counterbody material.

From a comparison of line profiles in Figs 4.2 and 4.6, we notice that the wear tracks are not clearly visible on line profile when sliding with 100Cr6 ball. This is due to adhesion of the counterbody material on site of nodular defects and on the hard coating surface rather than frequent breaking of nodular defects, as observed in sliding against Al_2O_3.

The SEM examination revealed the initial mechanism, when sliding with softer counterbody: **the micro-cutting**. The chip adhered to the nodular defect on Figure 4.16 and Figure 4.19 is a result micro-cutting. This produces a large amount of the counterbody wear debris (Figure 4.18). A part of the debris is pushed to the edges of the wear track where they accumulate, as in sliding with alumina counterbody. The remaining part of the counterbody wear debris is mixed with nodular defect debris. These wear products are collected on the sites of the remaining nodular defects. Elongated defects arranged perpendicular to sliding direction or group of defects present an effective anchorage site for the debris. The debris form poorly adhered **tribofilm patches**, but as sliding continues these tribofilm patches become denser. Dense patches of wear material around the nodular defect protect it to some extend by lowering the pressure acting on the nodular defect. Although the defect was protected by the film patch, the tangential forces caused the formation and propagation of the crack parallel to the hard coating surface (Figure 4.20). Such mechanism release all accumulated wear debris back into the moving contact. This is expressed as short fluctuations in coefficient of friction. The remaining debris is pushed into depressions or craters at the site of nodular defects.

Craters in hard coating are created when nodular defects break into small pieces or as shown in Figure 4.17, when nodular defects are **wrenched out** as a whole. This happen due to poor adhesion to the substrate, large compressive stress in the coating and tangential forces acting on the defect [76].

The wear mechanisms between different counterbody materials express in coefficient of friction behavior. The leveling process of nodular defects, when sliding with alumina ball takes a longer time than the micro-cutting process of the softer 100Cr6 counterbody material.

Thus coefficient of friction reaches a stable value after a few cycles in alumina and 100 cycles with 100Cr6 ball. The softer counterbody also experiences more sever wear.

It must be emphasized that all the described processes on the nodular defects and on the counterbody (**100Cr6 and alumina**) are **continuous** and that at some point they all happen **at the same time**. As the nodular defects are worn out in the middle of the wear track, the initial wear processes happen on the edges of the wear track. This way the wear track is constantly increasing in width, creating new wear debris and pushing them into newly created depressions and towards the edge of the wear track. As all these **processes are happening simultaneously**, the individual events on the nodular defects (breaking, tribo film formation etc.) are not distinctively visible on the COF curve.

Similar processes on nodular defects also happen when the atmosphere in which sliding occurs is changed. The focus of the thesis was on the overall hard coating performance in **different atmospheres**. The influence of nodular defects in different atmospheres was not studied but we can notice that the COF running-in period is longer in nitrogen atmosphere. This indicates that the breaking and powdering of the nodular defects runs more slowly in inert atmosphere then in the ambient air atmosphere.

Ambient air atmosphere tests show that the highest COF is obtained with TiAlN hard coating. The COF reaches a stable value of 1.0. The single layer TiN coating exhibits fluctuations while slowly increasing in COF, reaching 0.8 at the end of the test. For CrN and Cr-based coatings COF does not fluctuate and shows a relatively stable value of coefficient of friction. The only exception is the CrAlN coating whose COF dramatically drops after approximately 2500 cycles. This happens because of weakly bound debris by water molecules which form a thin lubricated film as already described in literature [43]. Such drops are not noticed in nitrogen and oxygen atmosphere since the bottled gas does not contain any moisture.

The change of atmosphere from ambient air to **nitrogen** influences the COF behavior. All final COF values of all the coatings are in the range of 0.55–0.65. In TiAlN and CrAlN coatings the hump in coefficient of friction in the beginning of the sliding is noticed. This can be attributed to the thin aluminum oxide layer which forms due to exposure of samples to air during storage. This top oxide layer is then worn down after some initial laps in the pure nitrogen environment, while the oxide layer is continuously growing when

testing in the pure oxygen or ambient air environment [111]. Since the tribo-oxidation is severely reduced in nitrogen environment, some other wear mechanisms, which are similar in all hard coatings, must prevail. Interestingly, while the chromium based coatings have higher COF in nitrogen compared to air measurements their wear is severely reduced, similar, as in all the other coatings. TiAlN coating still exhibits the largest wear, while other hard coatings wear is minimal. Comparing coating wear rates in ambient air and nitrogen atmosphere we can conclude that the wear processes are mainly oxidation driven. Furthermore, in chromium based coatings the tribo-oxidation layer and ambient air moisture provides conditions for low friction as can be deduced from an increase of COF in nitrogen atmosphere. The EDS and BSE analysis does not show any oxidation of the wear tracks in nitrogen atmosphere, just the wear debris in the edges are oxidized. Since the amount of oxidized debris is small we can assume that the oxidation occurred due to adsorbed water and oxygen on the coating surface.

Using pure **oxygen atmosphere** the surface chemical reactions are promoted. Similar as in nitrogen atmosphere the COF increases for the tested coatings compared to ambient air conditions while the relative wear is similar. The exception is only the TiN hard coating which experiences the reduction of wear. SEM analysis of wear tracks showed that coatings form thin oxide layer, which was undetectable by EDS analysis, but clearly seen in BSE images. This layer protects the hard coating from severe wear even though the COF is higher. Throughout the whole testing in all atmospheres we notice that changes in tribological behavior happen due to surface chemical reactions with oxygen and related interactions with humidity (moisture). The higher humidity can promote different surface reaction products (i.e. rutile formation at high relative humidity, anatase at low humidity)[101]. The titanium based coating behavior is severely influenced by the formation of hydrophilic TiO_x [101]. The relatively high friction coefficient of TiN and its large oscillations in oxygen and the ambient air environment could be related to shearing of the amorphous debris [112]. The higher friction coefficient in the oxygen environment is influenced by the absence of moisture which can weakly bind the debris forming a thin low-friction tribological layer [43]. While the growth of the protective oxide layer on the surface of wear tracks and the effect of humidity can sufficiently explain different COF and wear behavior of hard coatings in different atmospheres, we cannot find the origin of fish-scale-like feature growth on CrAlN and CrVN coatings in oxygen atmosphere. Detailed SEM/EDS analysis showed that they compose manly of chromium oxide, but further chemical surface analysis and mechanical properties at nano-scale are needed to explain their influence on tribological behavior and their relation to Al/Cr and V/Cr ratio.

Chapter 7

Conclusions

In the thesis the tribological properties of magnetron sputtered hard coatings were investigated. There are several stages of friction mechanisms in the sliding contact. Two major stages are emphasized in my thesis. The **first stage**, which is called the **running-in period**, is governed by contacting asperities – coating nodular defects. Their role and friction/wear behavior in the contact with other materials is difficult to observe and study. Our cycle-to-cycle study offers a **novel approach** which enables the inside view in the tribological contact even when realistic counterbody materials are used.

The second stage in focus is the **steady state period**. This stage of friction is governed mainly by the chemical reactions between sliding surfaces and environment. To test this thesis pin-on-disc experiments were performed on different conventional and advanced coatings and under different atmospheres (ambient air, nitrogen and oxygen atmosphere).

To summarize the aims of the thesis I will answer some basic questions that motivated our research as posed in the Introduction.

1. **What influences the running-in period?**

The running-in period is influenced mainly by the coating surface topography. Our research was focused on unavoidable topographical features of the magnetron sputtering; the **nodular defects** and their role in the tribological contact. Tests were performed in two modes, linear and cyclic, and with two different materials as a counterbody, producing distinct differences in tribological behavior.

In a **reciprocal mode** when using the **alumina counterbody** the running-in period lasted for about 80 cycles. The initial values of COF were about 0.2 and reached 0.7 after 80 cycles. The SEM analysis revealed that the majority of nodular defects were leveled with the surface at the end of the running-in period. Even though each test was performed on the fresh surface, similar COF behavior can be seen. Small differences in COF naturally occurred due to changes in local growth defect density.

The use of a softer, but more realistic counterbody material **100Cr6,** caused different COF behavior. A friction jump happens immediately and COF reaches the value above 0.6 during the first few cycles. Then the COF value slowly decreases reaching 0.6 in approximately 1000 cycles. The SEM analysis confirmed the formation of tribological film patches around the nodular defects. Many of the nodular defects break apart but the hard coating did not suffer any significant damages.

Unidirectional mode testing generally shows longer running-in periods due to fewer passes of the counterbody over the nodular defects. For **alumina** counterbody the duration of running-in period lasts for 100 cycles, while in the case of **100Cr6** material the initial friction jump occurs in the first 10 cycles, then additional 50 cycles were done to reach a steady state value of COF at about 0.7.

2. **What is the most important origin of the wear particles between the sliding surfaces?**

The cycle-to-cycle experiments have clearly demonstrated that in the initial sliding the nodular defects are the major sources of wear particles. Regardless the counterbody material the majority of defects broke into smaller particles that contributed to friction and wear behavior. Since defect particles have similar hardness as the hard coating, they contribute to abrasion of the coating and the counterbody material. The latter is clearly seen in the case of the softer counterbody material.

3. How do nodular defects act when sliding with 100Cr6 or Al_2O_3 counterbody?

The intrinsic hardness of the counterbody material invokes different behavior of nodular defects in the tribological coatings. This is evident regardless of whether the tribological testing is performed in cyclic or linear mode. The novel **cycle-to-cycle** observation method provided us with chronological observation of the same defects in the contact.

When using the **100Cr6 counterbody,** the first mechanism evident after just one cycle sliding is the **micro-cutting** of the counterbody material by hard and sharp tips of the nodular defects. This can be observed on the defects in the form of adhered chips and also as scratches on the scar surface of the counterbody. As long as this mechanism is active, the COF remains low (<10 cycles).

The micro-cutting produces a large amount of wear debris. It is gathered at the edges of the wear track and at the sites of nodular defects. Craters fill up with debris while nodular defects act as anchorage sides where the debris accumulates. This process produces **tribological film patches**. As the sliding continues, the patches become larger and denser. This increases the surface area of nodular defect which consequently decreases the pressure acting on the defect. Simultaneously to the patch formation at some defect sites, other defects are **broken** into small particles or they are **pulled out** of the hard coating in one piece. In both cases the result is a crater, forming at the site of the nodular defect. The described process continues at different regions of the wear track for the whole testing period, while the damage of the hard coating was not observed.

The hardness of the **alumina counterbody** is comparable to the hard coating. Therefore the observed processes are different than those observed when sliding with the softer 100Cr6 counterbody. During the first few cycles the **plastic deformation** of the nodular defects was observed. This process created large particles. As the sliding continues, the **powdering** of nodular defects starts. This creates finer debris material that fills up craters in the wear track. Eventually the nodular defects are completely worn away and the **surface is leveled**. This marks the end of the running-in period.

Wear and deformation of the counterbody surface produces asperities which cause the **abrasion** of the hard coating. SEM images reveal that **tribological oxidation** of the hard coating and the **formation of roll-like debris** occurs when nodular defects are leveled with the coating surface.

4. Is there any difference between sliding modes observed in the running-in period?

Small differences in COF and wear behavior between the two modes were observed. Namely the first one is a **higher friction** when using the cyclic mode. In the case of linear mode, two passes in opposite directions occur in one cycle. This creates the tangential forces acting on the nodular defect on two sides enabling the defect to plastically deform in fewer cycles.

When a softer counterbody material is used, the formation of tribological film patches starts on both sides of the nodular defect. This should create a denser and more stable tribological film patch providing better protection of the nodular defect and the coating surface.

5. How do different hard coatings behave in terms of friction and wear in the ambient atmosphere?

Testing of hard coatings in ambient atmosphere provided us with similar results as those of other authors. Both TiN and TiAlN coatings have the highest COF and wear rate. This result indicates that titanium oxides forming in the wear track possess a more intense friction behavior than the chromium nitride tribological products. TiAlN also forms aluminum oxide which increases the COF to approximately 1.0. All chromium based coatings have a lower COF than the titanium based ones. The CrAlN coating exhibited a drop in COF behavior after approximately 3000 cycles. Such behavior is not an intrinsic coating property, but it is a result of water molecules that weakly bind the debris in the form of a thin tribological film.

The wear rate was high for TiAlN and TiN coating while chromium-based coatings exhibited much lower wear rates.

6. **How do hard coatings behave in terms of friction and wear in inert or highly oxidative atmosphere? What is the role of tribological oxidation?**

Inert **nitrogen atmosphere** suppresses the tribological oxidation. This can be seen in a lower wear rate, for one order of magnitude, for all hard coatings tested. COF behavior of coatings is different compared to the ambient air measurements. TiAlN exhibits a friction bump in the running-in period. This is associated with the slow wear of the surface native oxides. As the native oxides are worn out, the COF decreases. This phenomenon was observed in coatings containing aluminum (TiAlN and CrAlN). The steady state of COF of all the coatings is similar, ranging from 0.5 to 0.6 which indicates that abrasion mechanism and polishing of the wear track are the main mechanisms in inert atmosphere for all hard coatings.

In contrary to the inert atmosphere, a pure **oxygen atmosphere** invokes the formation of oxides. This can be observed as higher friction and wear. In contrast to the ambient air test atmosphere, the friction is the highest for TiN coating while the COF and relative wear behavior of TiAlN coating is similar to the ambient conditions. For chromium-based coatings the average COF values are between 0.6 and 0.7, and the wear rate is similar to the wear track obtained in ambient atmosphere tests.

From the difference in behavior in inert and oxidizing atmosphere the role of tribological oxidation can be derived. The results show that titanium-based coatings possess lower oxidation resistance than the chromium ones. This is in agreement with other researches that showed high oxidation resistance (stability) of chromium-based hard coatings. Therefore the similar COF behavior at room temperature of chromium-based coatings in inert and oxidizing atmosphere is expected. The difference in COF between the ambient air tests and nitrogen or oxygen could be the level of relative humidity.

Though only small changes in COF were observed in chromium-based coatings in the oxygen atmosphere compared to other atmospheres, **fish-scale-like products** were found only in wear track made in oxygen atmosphere. A wear track comparison between CrAlN and CrVN coatings with a different amount of vanadium and aluminum showed that the density of fish-scale-like products increases with the content of the alloying element.

7. **Are there any differences in tribological behavior between conventional and advanced coatings?**

All advanced nanolayered coatings show superior friction and wear behavior compared to the conventional TiN, TiAlN and CrN hard coatings Low friction and wear rate was observed in all advanced coatings in all atmospheres tested. Although the thickness of advanced coatings was relatively large, the coatings did not crack as the CrN coating did.

It must be emphasized that the advanced CrAlN and CrVN coatings are preferably used for high temperature applications. CrAlN coating should show high thermal stability up to 900 °C, while CrVN coatings are used as solid lubrication coatings at temperatures above 600 °C. The tribological behavior at higher temperatures is a topic for further research.

References

1. Holmberg, K., H. Ronkainen, and A. Matthews, *Wear Mechanisms of Coated Sliding Surfaces*, in *Tribology Series*, C.M.T.T.H.C.C.M.G. D. Dowson and G. Dalmaz, Editors. 1993, Elsevier. p. 399-407.
2. Ali, M., E. Hamzah, and M.R. Toff, *Friction coefficient and surface roughness of TiN-coated HSS deposited using cathodic arc evaporation PVD technique.* Industrial Lubrication and Tribology, 2008. **60**(3): p. 121-130.
3. Harlin, P., et al., *Influence of surface roughness of PVD coatings on tribological performance in sliding contacts.* Surface and Coatings Technology, 2006. **201**(7): p. 4253-4259.
4. Jeng, Y.-R., Z.-W. Lin, and S.-H. Shyu, *Changes of Surface Topography During Running-In Process.* Journal of Tribology, 2004. **126**(3): p. 620-625.
5. Klünsner, T., et al., *Influence of surface topography on early stages on steel galling of coated WC-Co hard metals.* International Journal of Refractory Metals and Hard Materials, 2016. **57**: p. 24-30.
6. Olofsson, J., et al., *On the influence from micro topography of PVD coatings on friction behaviour, material transfer and tribofilm formation.* Wear, 2011. **271**(9–10): p. 2046-2057.
7. Podgornik, B. and J. Jerina, *Surface topography effect on galling resistance of coated and uncoated tool steel.* Surface and Coatings Technology, 2012. **206**(11–12): p. 2792-2800.
8. Podgursky, V., et al., *Dependence of the friction coefficient on roughness parameters during early stage fretting of (Al,Ti)N coated surfaces.* Wear, 2011. **271**(5–6): p. 853-858.
9. Podgursky, V., et al., *Comparative study of surface roughness and tribological behavior during running-in period of hard coatings deposited by lateral rotating cathode arc.* Wear, 2010. **268**(5–6): p. 751-755.
10. Dossett, J. and G. Totten, *Introduction to Surface Hardening of Steels.* 2013.
11. Hogmark, S., S. Jacobson, and M. Larsson, *Design and evaluation of tribological coatings.* Wear, 2000. **246**(1–2): p. 20-33.
12. PalDey, S. and S. Deevi, *Single layer and multilayer wear resistant coatings of (Ti, Al) N: a review.* Materials Science and Engineering: A, 2003. **342**(1): p. 58-79.
13. Quinto, D.T., *Twenty-five years of PVD coatings at the cutting edge.* SVC Bulletin, Fall, 2007. **17**: p. 22.
14. Zhang, S. and W. Zhu, *TiN coating of tool steels: a review.* Journal of Materials Processing Technology, 1993. **39**(1): p. 165-177.
15. Ohring, M., *Materials science of thin films*. 2001: Academic press.
16. Anders, A., *A structure zone diagram including plasma-based deposition and ion etching.* Thin Solid Films, 2010. **518**(15): p. 4087-4090.
17. Thornton, J.A., *Influence of apparatus geometry and deposition conditions on the structure and topography of thick sputtered coatings.* Journal of Vacuum Science & Technology, 1974. **11**(4): p. 666-670.

18. Panjan, M., *Physical and chemical properties of nanolayered metalnitride coatings prepared by sputtering*, in *Department of material science and metalurgy*. 2010, University of Ljubljana.
19. Panjan, P., et al., *Zaščita orodij s trdimi PVD-prevlekami*. 2005: Institut" Jozef Stefan".
20. Sundgren, J.-E., *Structure and properties of TiN coatings.* Thin solid films, 1985. **128**(1): p. 21-44.
21. Polcar, T., N.M.G. Parreira, and R. Novák, *Friction and wear behaviour of CrN coating at temperatures up to 500 °C.* Surface and Coatings Technology, 2007. **201**(9-11): p. 5228-5235.
22. Navinšek, B., P. Panjan, and I. Milošev, *Industrial applications of CrN (PVD) coatings, deposited at high and low temperatures.* Surface and Coatings Technology, 1997. **97**(1): p. 182-191.
23. Polcar, T., et al., *Comparison of tribological behaviour of TiN, TiCN and CrN at elevated temperatures.* Surface and Coatings Technology, 2005. **193**(1-3): p. 192-199.
24. Ballhause, P., et al., *Containing papers presented at the 12th International Vacuum Congress CrNx — a hard coating for corrosion and wear resistance.* Materials Science and Engineering: A, 1993. **163**(2): p. 193-196.
25. Knotek, O., M. Böhmer, and T. Leyendecker, *On structure and properties of sputtered Ti and Al based hard compound films.* Journal of Vacuum Science & Technology A, 1986. **4**(6): p. 2695-2700.
26. Tönshoff, K., et al., *Wear mechanisms of (Ti1 − x,Alx)N coatings in dry drilling.* Surface and Coatings Technology, 1997. **94**: p. 603-609.
27. Yoon, S.-Y., J.-K. Kim, and K.H. Kim, *A comparative study on tribological behavior of TiN and TiAlN coatings prepared by arc ion plating technique.* Surface and Coatings Technology, 2002. **161**(2): p. 237-242.
28. Aihua, L., et al., *Friction and wear properties of TiN, TiAlN, AlTiN and CrAlN PVD nitride coatings.* International Journal of Refractory Metals and Hard Materials, 2012. **31**: p. 82-88.
29. Santecchia, E., et al., *Wear resistance investigation of titanium nitride-based coatings.* Ceramics International, 2015. **41**(9, Part A): p. 10349-10379.
30. Reiter, A.E., et al., *Investigation of the properties of Al1−xCrxN coatings prepared by cathodic arc evaporation.* Surface and Coatings Technology, 2005. **200**(7): p. 2114-2122.
31. Brizuela, M., et al., *Magnetron sputtering of Cr(Al)N coatings: Mechanical and tribological study.* Surface and Coatings Technology, 2005. **200**(1-4): p. 192-197.
32. Shah, H.N. and R. Jayaganthan, *Influence of Al Contents on the Microstructure, Mechanical, and Wear properties of Magnetron Sputtered CrAlN Coatings.* Journal of Materials Engineering and Performance, 2012. **21**(9): p. 2002-2009.
33. Sanchéz, J.E., et al., *Mechanical, tribological, and electrochemical behavior of Cr1−xAlxN coatings deposited by r.f. reactive magnetron co-sputtering method.* Applied Surface Science, 2010. **256**(8): p. 2380-2387.
34. Li, T., et al., *High temperature corrosion behavior of a multilayer CrAlN coating prepared by magnetron sputtering method on a K38G alloy.* Surface and Coatings Technology, 2008. **202**(10): p. 1985-1993.
35. Le Bourhis, E., et al., *Mechanical properties of hard AlCrN-based coated substrates.* Surface and Coatings Technology, 2009. **203**(19): p. 2961-2968.
36. Qiu, Y., et al., *Improvement of tribological performance of CrN coating via multilayering with VN.* Surface and Coatings Technology, 2013. **231**: p. 357-363.
37. Wriedt, H.A., *The O-V (Oxygen-Vanadium) system.* Bulletin of Alloy Phase Diagrams, 1989. **10**(3): p. 271-277.

38. Franz, R. and C. Mitterer, *Vanadium containing self-adaptive low-friction hard coatings for high-temperature applications: A review.* Surface and Coatings Technology, 2013. **228**: p. 1-13.
39. Panjan, P., et al., *Oxidation resistance of CrN/(Cr,V)N hard coatings deposited by DC magnetron sputtering.* Thin Solid Films, 2015. **591, Part B**: p. 323-329.
40. Holmberg, K. and A. Matthews, *Coating Tribology: Properties, Techniques, and Applications in Surface Engineering*. 1994: Elsevier.
41. Holmberg, K., A. Matthews, and H. Ronkainen, *Coatings tribology—contact mechanisms and surface design.* Tribology International, 1998. **31**(1): p. 107-120.
42. Holmberg, K., H. Ronkainen, and A. Matthews, *Tribology of thin coatings.* Ceramics International, 2000. **26**(7): p. 787-795.
43. Kato, K., *Wear in relation to friction—a review.* Wear, 2000. **241**(2): p. 151-157.
44. Bhushan, B., *Modern tribology handbook, two volume set*. 2000: CRC press.
45. Hokkirigawa, K. and K. Kato, *An experimental and theoretical investigation of ploughing, cutting and wedge formation during abrasive wear.* Tribology International, 1988. **21**(1): p. 51-57.
46. Ashby, M.F., J. Abulawi, and H.S. Kong, *Temperature Maps for Frictional Heating in Dry Sliding*. Tribology Transactions, 1991. **34**(4): p. 577-587.
47. Wilson, S. and A.T. Alpas, *Wear mechanism maps for TiN-coated high speed steel.* Surface & Coatings Technology, 1999. **120**: p. 519-527.
48. Guha, D. and S.K. Roy Chowdhuri, *The effect of surface roughness on the temperature at the contact between sliding bodies.* Wear, 1996. **197**(1–2): p. 63-73.
49. Suh, N.P. and H.C. Sin, *The genesis of friction.* Wear, 1981. **69**(1): p. 91-114.
50. Bowden, F. and D. Tabor, *Friction and Lubrication of Solids, vol. I. Clarendon*. 1950, Oxford.
51. Blau, P.J., *On the nature of running-in.* Tribology International, 2005. **38**(11–12): p. 1007-1012.
52. Singer, I.L., et al., *Role of third bodies in friction and wear of protective coatings.* Journal of Vacuum Science & Technology A, 2003. **21**(5): p. S232-S240.
53. Dienwiebel, M. and K. Pöhlmann, *Nanoscale evolution of sliding metal surfaces during running-in.* Tribology Letters, 2007. **27**(3): p. 255-260.
54. Blau, P.J., *Friction science and technology: from concepts to applications*. 2008: CRC press.
55. Luo, Q., *Origin of Friction in Running-in Sliding Wear of Nitride Coatings.* Tribology Letters, 2010. **37**(3): p. 529-539.
56. Nogueira, I., et al., *An experimental model for mixed friction during running-in.* Wear, 2002. **253**(5–6): p. 541-549.
57. Chromik, R.R., et al., *Run-in behavior of nanocrystalline diamond coatings studied by in situ tribometry.* Wear, 2008. **265**(3–4): p. 477-489.
58. Akbarzadeh, S. and M. Khonsari, *Experimental and theoretical investigation of running-in.* Tribology International, 2011. **44**(2): p. 92-100.
59. Stempflé, P. and R.K. Njiwa, *In situ running-in wear assessment in multi-asperity nanotribology.* Wear, 2015. **328–329**: p. 77-88.
60. Garbar, I., *Microstructural changes in surface layers of metal during running-in friction processes.* Meccanica, 2001. **36**(6): p. 631-639.
61. Biswas, S.K., *Some mechanisms of tribofilm formation in metal/metal and ceramic/metal sliding interactions.* Wear, 2000. **245**(1–2): p. 178-189.
62. Chen, M., K. Kato, and K. Adachi, *The difference in running-in period and friction coefficient between self-mated Si3N4 and SiC under water lubrication.* Tribology Letters, 2001. **11**(1): p. 23-28.

63. Kumar, R., B. Prakash, and A. Sethuramiah, *A systematic methodology to characterise the running-in and steady-state wear processes.* Wear, 2002. **252**(5): p. 445-453.
64. Wilson, S. and A. Alpas, *TiN coating wear mechanisms in dry sliding contact against high speed steel.* Surface and coatings technology, 1998. **108**: p. 369-376.
65. Uchida, M., et al., *Friction and wear properties of CrAlN and CrVN films deposited by cathodic arc ion plating method.* Surface and Coatings Technology, 2004. **177**: p. 627-630.
66. Mao, K., Y. Sun, and T. Bell, *CONTACT MECHANICS OF ENGINEERING SURFACES: STATE OF THE ART.* Surface Engineering, 1994. **10**(4): p. 297-306.
67. Harlin, P., U. Bexell, and M. Olsson, *Influence of surface topography of arc-deposited TiN and sputter-deposited WC/C coatings on the initial material transfer tendency and friction characteristics under dry sliding contact conditions.* Surface and Coatings Technology, 2009. **203**(13): p. 1748-1755.
68. Drnovšek, A., et al., *The influence of growth defects in sputter-deposited TiAlN hard coatings on their tribological behavior.* Surface and Coatings Technology, 2016. **288**: p. 171-178.
69. Panjan, P., et al., *Growth defects in PVD hard coatings.* Vacuum, 2009. **84**(1): p. 209-214.
70. Panjan, P., et al., *Surface density of growth defects in different PVD hard coatings prepared by sputtering.* Vacuum, 2012. **86**(6): p. 794-798.
71. Panjan, P., et al., *SEM study of defects in PVD hard coatings using focused ion beam milling.* Surface and Coatings Technology, 2008. **202**(11): p. 2302-2305.
72. Vetter, J., M. Stüber, and S. Ulrich, *Growth effects in carbon coatings deposited by magnetron sputtering.* Surface and Coatings Technology, 2003. **168**(2–3): p. 169-178.
73. Spalvins, T., *International Conference on Metallurgical Coatings, San Diego, 1979-Part IIICharacterization of defect growth structrures in ion-plated films by scanning electron microscopy.* Thin Solid Films, 1979. **64**(1): p. 143-148.
74. Panjan, P., et al., *Growth defect density in PVD hard coatings prepared by different deposition techniques.* Surface and Coatings Technology, 2013. **237**: p. 349-356.
75. Čekada, M., et al., *SEM study of defects in PVD hard coatings.* Vacuum, 2007. **82**(2): p. 252-256.
76. Münz, W.D., et al., *Defects in TiN and TiAlN coatings grown by combined cathodic arc/unbalanced magnetron technology.* Vacuum, 1995. **46**(4): p. 323-330.
77. Powell, R.A. and S.M. Rossnagel, *PVD for microelectronics: sputter deposition applied to semiconductor manufacturing*. Vol. 8. 1999: Elsevier.
78. Selwyn, G.S., et al., *Particle contamination formation in magnetron sputtering processes.* Journal of Vacuum Science & Technology A, 1997. **15**(4): p. 2023-2028.
79. Podgornik, B., S. Hogmark, and O. Sandberg, *Influence of surface roughness and coating type on the galling properties of coated forming tool steel.* Surface and Coatings Technology, 2004. **184**(2–3): p. 338-348.
80. Archard, J.F., *Surface topography and tribology.* Tribology, 1974. **7**(5): p. 213-220.
81. Stout, K.J., T.G. King, and D.J. Whitehouse, *Analytical techniques in surface topography and their application to a running-in experiment.* Wear, 1977. **43**(1): p. 99-115.
82. Sedlaček, M., et al., *Surface Topography Modelling for Reduced Friction.* 2011, 2011. **57**(9).
83. Jacobson, S. and S. Hogmark, *Surface modifications in tribological contacts.* Wear, 2009. **266**(3–4): p. 370-378.
84. Chromik, R., H. Strauss, and T. Scharf, *Materials phenomena revealed by in situ tribometry.* Jom, 2012. **64**(1): p. 35-43.

85. Rebelo de Figueiredo, M., et al., *In Situ Studies of TiC1−x N x Hard Coating Tribology.* Tribology Letters, 2010. **40**(3): p. 365-373.
86. Carlsson, P. and M. Olsson, *PVD coatings for sheet metal forming processes—a tribological evaluation.* Surface and Coatings Technology, 2006. **200**(14–15): p. 4654-4663.
87. Podgornik, B., J. Vižintin, and S. Hogmark, *Improvement in galling performance through surface engineering.* Surface Engineering, 2006. **22**(4): p. 235-238.
88. Tkadletz, M., et al., *The effect of droplets in arc evaporated TiAlTaN hard coatings on the wear behavior.* Surface and Coatings Technology, 2014. **257**(0): p. 95-101.
89. Wang, H.W., et al., *Wear associated with growth defects in combined cathodic arc/unbalanced magnetron sputtered CrN/NbN superlattice coatings during erosion in alkaline slurry.* Surface and Coatings Technology, 2000. **135**(1): p. 82-90.
90. Tench, R.J., R. Chow, and M.R. Kozlowski, *Characterization of defect geometries in multilayer optical coatings.* Journal of Vacuum Science & Technology A, 1994. **12**(5): p. 2808-2813.
91. Guenther, K.H., *Nodular defects in dielectric multilayers and thick single layers.* Applied Optics, 1981. **20**(6): p. 1034-1038.
92. Reicher, D., P. Black, and K. Jungling, *Defect formation in hafnium dioxide thin films.* Applied Optics, 2000. **39**(10): p. 1589-1599.
93. Fenker, M., M. Balzer, and H. Kappl, *Corrosion protection with hard coatings on steel: Past approaches and current research efforts.* Surface and Coatings Technology, 2014. **257**(0): p. 182-205.
94. Petrogalli, C., et al., *Tribological and corrosion behavior of CrN coatings: Roles of substrate and deposition defects.* Surface and Coatings Technology, 2014. **258**: p. 878-885.
95. Rossnagel, S.M., R. Powell, and A. Ulman, *PVD for Microelectronics: Sputter Desposition to Semiconductor Manufacturing*. 1998: Academic Press.
96. Lewis, D.B., et al., *The role of the growth defects on the corrosion resistance of CrN/NbN superlattice coatings deposited at low temperatures.* Thin Solid Films, 2006. **503**(1–2): p. 143-148.
97. Sasaki, S., *The effects of the surrounding atmosphere on the friction and wear of alumina, zirconia, silicon carbide and silicon nitride.* Wear, 1989. **134**(1): p. 185-200.
98. Ray, S. and S.K. Roy Chowdhury, *Prediction of contact temperature rise between rough sliding bodies: An artificial neural network approach.* Wear, 2009. **266**(9–10): p. 1029-1038.
99. Vick, B. and M.J. Furey, *A basic theoretical study of the temperature rise in sliding contact with multiple contacts.* Tribology International, 2001. **34**(12): p. 823-829.
100. zu Köcker, G.M., T. Gross, and E. Santner, *Influence of the testing parameters on the tribological behaviour of self-mated PVD-coatings.* Wear, 1994. **179**(1): p. 5-10.
101. Gant, A.J., M.G. Gee, and L.P. Orkney, *The wear and friction behaviour of engineering coatings in ambient air and dry nitrogen.* Wear, 2011. **271**(9-10): p. 2164-2175.
102. Mo, J.L., et al., *Comparison of tribological behaviours of AlCrN and TiAlN coatings—Deposited by physical vapor deposition.* Wear, 2007. **263**(7–12): p. 1423-1429.
103. Wilson, S. and A.T. Alpas, *Tribo-layer formation during sliding Wear of TiN coatings.* Wear, 2000. **245**(1-2): p. 223-229.
104. Wu, P.Q., et al., *Comparison of wear and corrosion wear of TiN coatings under uni- and bidirectional sliding.* Surface and Coatings Technology, 1999. **113**(3): p. 251-258.
105. de Wit, E., M.A.M. Walet, and J.P. Celis, *Ultramicrotomy on fretting wear debris.* Microscopy Research and Technique, 1998. **40**(6): p. 492-494.

106. Oliver, W.C. and G.M. Pharr, *An improved technique for determining hardness and elastic modulus using load and displacement sensing indentation experiments.* Journal of materials research, 1992. **7**(06): p. 1564-1583.
107. Čekada, M. *Orientacija vzorcev in identifikacija motivov pri mikroskopiji*. Vakuumist 2012 [cited 2016 28.11.].
108. Drnovšek, A., et al., *The influence of surrounding atmosphere on tribological properties of hard protective coatings.* Surface and Coatings Technology, 2015. **267**: p. 15-20.
109. Zhou, Z., et al. *Investigating worn surfaces of nanoscale TiAlN/VN multilayer coating using FIB and TEM*. in *Journal of Physics: Conference Series*. 2006. IOP Publishing.
110. Zhou, Z., et al., *Wear and friction of TiAlN/VN coatings against Al2O3 in air at room and elevated temperatures.* Acta Materialia, 2010. **58**(8): p. 2912-2925.
111. Wang, X., et al., *Friction coefficient and sliding wear of AlTiN coating under various lubrication conditions.* Wear, 2013. **304**(1-2): p. 67-76.
112. Hofmann, D., et al., *New multilayer PVD-coating technique for cutting tools.* Surface and Coatings Technology, 1993. **61**(1–3): p. 326-330.
113. Luo, Q., *Temperature dependent friction and wear of magnetron sputtered coating TiAlN/VN.* Wear, 2011. **271**(9): p. 2058-2066.
114. Luo, Q., et al., *TEM-EELS study of low-friction superlattice TiAlN/VN coating: the wear mechanisms.* Tribology Letters, 2006. **24**(2): p. 171-178.

Bibliography

Publications Related to the Thesis

Drnovšek, A., Panjan, P., Panjan, M., & Čekada, M. (2016). The influence of growth defects in sputter-deposited TiAlN hard coatings on their tribological behavior. *Surface and Coatings Technology, 288*, 171-178. doi: http://dx.doi.org/10.1016/j.surfcoat.2016.01.021

Drnovšek, A., Panjan, P., Panjan, M., Paskvale, S., Buh, J., & Čekada, M. (2015). The influence of surrounding atmosphere on tribological properties of hard protective coatings. *Surface and Coatings Technology, 267*, 15-20. doi: http://dx.doi.org/10.1016/j.surfcoat.2014.11.068

Panjan, P., Drnovšek, A., Kovač, J., Gselman, P., Bončina, T., Paskvale, S., . . . Panjan, M. (2015). Oxidation resistance of CrN/(Cr,V)N hard coatings deposited by DC magnetron sputtering. *Thin Solid Films, 591, Part B*, 323-329. doi: http://dx.doi.org/10.1016/j.tsf.2015.05.010

Journal Articles

Čekada, M., Radić, N., Jerčinović, M., Panjan, M., Panjan, P., Drnovšek, A., & Car, T. Growth defects in magnetron sputtered PVD films deposited in UHV environment. *Vacuum*. doi: http://dx.doi.org/10.1016/j.vacuum.2016.12.012

Drnovšek, A., Panjan, P., Panjan, M., & Čekada, M. (2016). The influence of growth defects in sputter-deposited TiAlN hard coatings on their tribological behavior. *Surface and Coatings Technology, 288*, 171-178. doi: http://dx.doi.org/10.1016/j.surfcoat.2016.01.021

Drnovšek, A., Panjan, P., Panjan, M., Paskvale, S., Buh, J., & Čekada, M. (2015). The influence of surrounding atmosphere on tribological properties of hard protective coatings. *Surface and Coatings Technology, 267*, 15-20. doi: http://dx.doi.org/10.1016/j.surfcoat.2014.11.068

Matavz, A., Frunza, R. C., Drnovsek, A., Bobnar, V., & Malic, B. (2016). Inkjet printing of uniform dielectric oxide structures from sol-gel inks by adjusting the solvent composition. *Journal of Materials Chemistry C*. doi: 10.1039/C6TC01090C

Panjan, P., Drnovšek, A., Kovač, J., Čekada, M., & Panjan, M. Oxidation processes in vanadium-based single-layer and nanolayer hard coatings. *Vacuum*. doi: http://dx.doi.org/10.1016/j.vacuum.2016.12.025

Panjan, P., Drnovšek, A., Kovač, J., Gselman, P., Bončina, T., Paskvale, S., . . . Panjan, M. (2015). Oxidation resistance of CrN/(Cr,V)N hard coatings deposited by DC magnetron sputtering. *Thin Solid Films, 591, Part B*, 323-329. doi: http://dx.doi.org/10.1016/j.tsf.2015.05.010

Conference Paper

Matavž, A., Frunză, R. C., Drnovsek, A., Bobnar, V., & Malič, B. (2016). *Inkjet printing of thin metal-oxide structures from sol-gel precursor inks.* Paper presented at the Applications of Ferroelectrics, European Conference on Application of Polar Dielectrics, and Piezoelectric Force Microscopy Workshop (ISAF/ECAPD/PFM), 2016 Joint IEEE International Symposium.

Other Publications

Drnovšek, A., & Mihailovic, D. D. (2012). An array smell sensor based on the measurement of the junction impedance of nanowires with different metals: **Patent SI 23582 (A)** / Aljaž Drnovšek, Dragan D. Mihailović

Biography

The author of this thesis was born in 1985 in Trbovlje, Slovenia. He studied Techniques of Measurement in Physics at the Faculty of Mathematics and Physics, University of Ljubljana and graduated in 2010 with diploma titled $MoSI_x$ - zaznava plina in transformacija v MoO_2 ($MoSI_x$ – gas detection and transformation into MoO_2) under supervision of Prof. Dr. Dragan D. Mihailović. He then attended a master study programme, Nanoscience and Nanotechnologies, at the Jožef Stefan International Postgraduate School and in 2012 successfully defended his Master Thesis titled Optimizacija $MoSI_x$ selektivnega plinskega nanosenzorja (Optimization of $MoSI_x$ selective gas sensor) under supervision of Prof. Dr. Dragan D. Mihailović. The same year he entered the Ph.D. program at the Jožef Stefan International Postgraduate School and started working in the Thin Films and Surfaces department at Jožef Stefan Institute under supervision of Asst. Prof. Dr. Miha Čekada.